Technische Universität München

TUM School of Computation, Information and Technology

High-Precision 3D Printed Scaffolds Mimicking Native Alveolar Tissue in Geometrical, Mechanical and Biochemical Cues

Amelie S. Erben

Vollständiger Abdruck der von der TUM School of Computation, Information and Technology der Technischen Universität München zur Erlangung des akademischen Grades einer

Doktorin der Ingenieurwissenschaften (Dr. Ing.)

genehmigten Dissertation

Vorsitz: Prof. Dr. Bernhard Wolfrum

Prüfer der Dissertation:

1. Prof. Dr. Oliver Hayden
2. Prof. Dr. Hauke Clausen-Schaumann

Die Dissertation wurde am 04.10.2022 bei der Technischen Universität München eingereicht und durch die TUM School of Computation, Information and Technology am 18.07.2023 angenommen.

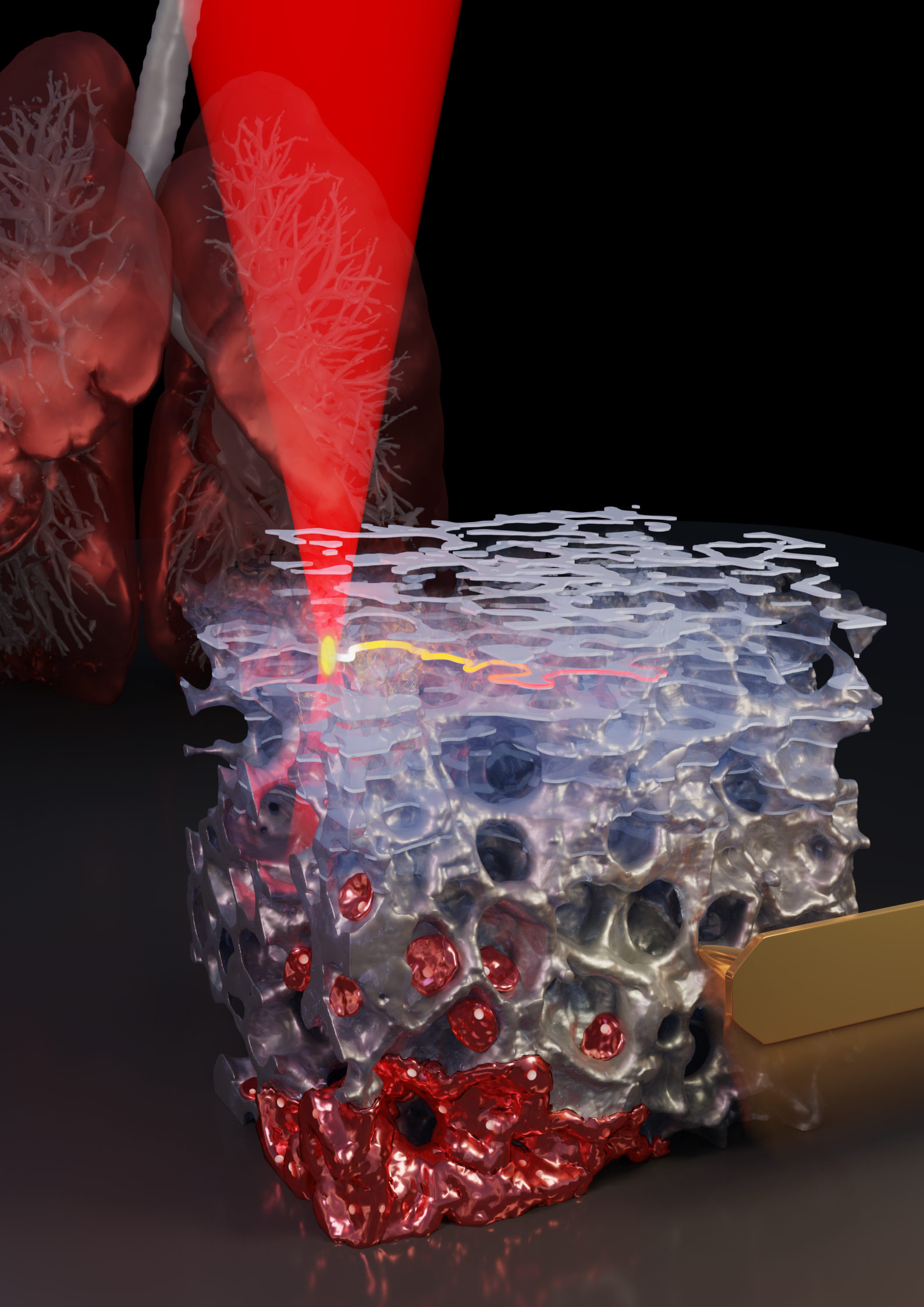

Abstract

Cellular dynamics are governed by the geometrical, mechanical and biochemical properties of the extracellular matrix (ECM) and vice versa[1]–[4]. This reciprocity proves essential for tissue and organ viability and many forms of interactions have extensively been investigated in 2D environments over the last decades. However, with the addition of the third dimension, cellular dynamics become increasingly complex and cellular behavior in 3D environments can differ significantly from 2D. Therefore, 3D *in vitro* models are being developed mimicking both healthy and pathological cell niches with the highest biological conformity including high resolution of biochemical and mechanical cues to achieve further insights in cell-ECM interactions including proliferation, differentiation and migration[1],[5]–[7]. Furthermore, by integrating an interveined micro vascular system, the nutrient supply as well as the distinct distribution of additional biochemical factors throughout ever larger tissues models can be enabled[1],[8]–[10].

The aim of this doctoral thesis was to improve precision 3D printed cell scaffolds mimicking native tissues in geometry, composition and mechanics. In particular, the fabrication of (i) up to mm-sized scaffolds with micrometer resolution printed from gelatin derived photo-resins which are suitable to culture and analyze a variety of cell lines as well as primary cells, (ii) with defined biomechanical properties, (iii) using biomimetic 3D print templates mimicking alveolar tissue and (iv) with integrated channels for selective perfusion was investigated.

Two-photon stereolithography (TPS) was adapted to fabricate up to mm-sized high-precision cell scaffolds at sub-cellular resolution from protein based photo-resins including gelatin methacrylate and bovine serum albumin and demonstrated compatibility with a variety of cells types including primary human lung fibroblasts. By tailoring the manufacturing settings such as objective specifications or laser power as well as by applying two-pass printing and post-print crosslinking, the Young's moduli of 3D printed high-precision cell scaffolds to range was quantified to be between 7 – 300 kPa. The effects of different scaffold geometries on cellular dynamics was observed using mouse myoblast cells.[1] Biomimetic 3D print templates mimicking the alveoli within the lung were either created by imaging of native alveolar tissue or by using generative design[1],[10]. In particular, generative design was used to create parametrized print templates with fully intact alveoli and capillary structures and tailorable properties such as wall thickness, degree of vascularization or number of alveoli. Finally, an ultra-compact perfusion chip

allowing for contacting, perfusion and cellularization of individual channels within protein printed scaffolds was explored, paving the way to fully vascularized high-resolution *in vitro* tissue models[10].

In summary, precision printed cell scaffolds mimicking native tissue in composition, mechanics and geometry were improved. The work in this doctoral thesis will allow for a systematic analysis of single cell and tissue dynamics in response to defined geometrical, mechanical and biomolecular environments and will eventually be scalable to full organs[1],[10].

Zusammenfassung

Die Zelldynamik wird von den geometrischen, mechanischen und biochemischen Eigenschaften der extrazellulären Matrix (ECM) bestimmt, wobei diese wiederum von der Zelldynamik beeinflusst werden[1]–[4]. Diese Wechselwirkung ist für die Vitalität von Geweben und Organen von entscheidender Bedeutung. Viele Formen der Zell-ECM Interaktionen wurden in den letzten Jahrzehnten eingehend in 2D Umgebungen untersucht. Durch die Einführung der dritten Dimension wird die Zelldynamik jedoch zunehmend komplexer, und das Zellverhalten in 3D Umgebungen kann sich erheblich von dem in 2D unterscheiden. Daher werden derzeit 3D-in-vitro-Modelle entwickelt, die sowohl gesunde als auch pathologische Zellnischen mit höchster biologischer Konformität nachahmen. Diese beinhalten eine hohe räumliche Auflösung biochemischer und mechanischer Signale, um weitere Einblicke in die Zell-ECM Interaktionen, einschließlich Proliferation, Differenzierung und Migration, zu gewinnen[1],[5]–[7]. Darüber hinaus kann durch die Integration eines vernetzten mikrovaskulären Systems die Nährstoffversorgung sowie die selektive Verteilung zusätzlicher biochemischer Faktoren in immer größeren Gewebemodellen ermöglicht werden[1],[8]–[10].

Das Ziel dieser Doktorarbeit war die Verbesserung von präzisen 3D-gedruckten Zellgerüsten, in Hinblick auf die Nachahmung von nativem Gewebe in Geometrie, biochemische Zusammensetzung und Mechanik. Insbesondere wurde zur Herstellung von (i) bis zu mm-großen Gerüsten bei gleichzeitiger Auflösung im einstelligen Mikrometerbereich beigetragen. Diese Zellgerüststrukturen wurden aus Gelatine-Phototinte gedruckt und eignen sich für die Kultivierung und Analyse einer Vielzahl von Zelllinien, darunter auch Primärzellen. Mit (ii) definierten biomechanischen Eigenschaften, (iii) unter Verwendung biomimetischer 3D-Druckvorlagen und (iv) mit integrierten Kanälen für die selektive Perfusion können diese Zellgerüste Alveolargewebe in diesen Aspekten imitieren.

Die Zwei-Photonen-Stereolithographie wurde adaptiert, um hochpräzise, mm-große Zellgerüste mit subzellulärer Auflösung aus proteinbasierten Photoharzen wie Gelatine-Methacrylat und Rinderserumalbumin herzustellen, und haben die Kompatibilität mit einer Vielzahl von Zelltypen einschließlich primärer menschlicher Lungenfibroblasten nachgewiesen. Durch Anpassung der Druckparameter, wie die Vergrößerung des Objektivs oder die Laserleistung, sowie durch mehrfache oder nachträgliche Vernetzung, konnten die Elastizitätsmodule von 3D-gedruckten, hochpräzisen Zellgerüsten in einem Bereich zwischen 7 und 300 kPa variiert werden. Die Auswirkungen verschiedener Gerüstgeometrien auf die Zelldynamik wurden mit Myoblastenzellen der Maus

beobachtet[1]. Biomimetische 3D-Druckvorlagen, die die Alveolen in der Lunge nachahmen, wurden entweder durch Bildgebung von nativem Alveolargewebe oder durch algorithmische Designmethoden erstellt[1],[10]. Insbesondere wurde algorithmisches Design verwendet, um parametrisierte Druckvorlagen mit vollständig intakten Alveolen und Kapillaren, sowie maßgeschneiderte Eigenschaften wie Wandstärke, Grad der Vaskularisierung oder Anzahl der Alveolen zu erstellen. Schließlich wurde ein ultrakompakter Perfusionschip entwickelt, der es ermöglicht, einzelne Kanäle innerhalb von proteingedruckten Scaffolds zu kontaktieren und perfundieren, um den Weg zu vollständig vaskularisierten, hochauflösenden *in vitro* Gewebemodellen zu ebnen[10].

Zusammenfassend lässt sich sagen, dass gedruckte, hochpräzise Zellgerüste in ihrer Nachahmung von nativem Gewebe in den Aspekten Zusammensetzung, Mechanik und Geometrie verbessert wurden. Die Ergebnisse dieser Doktorarbeit werden eine systematische Analyse der Dynamik einzelner Zellen und Gewebe als Reaktion auf definierte geometrische, mechanische und biomolekulare Umgebungen ermöglichen und wird schließlich auf ganze Organe skalierbar sein[1],[10].

Table of Contents

Abbreviations

ALI	*air liquid interface*
C2C12	*mouse myoblast cells*
CAD	*computer aided design*
DAPI	*4',6-diamidino-2-phenylindole*
DMEM	*Dulbecco's Modified Eagle Medium*
ECM	*extra cellular matrix*
EDTA	*ethylene diaminetetraacetic acid*
GelMa	*gelatin methacryloyl*
GM10	*modified gelatin methacryloyl*
hMSCs	*human mesenchymal stem cells*
HUVECs	*human umbilical vein endothelial cells*
IT-AFM	*indention type atomic force microscopy*
LAP	*lithium phenyl-2,4,6-trimethylbenzoylphosphinate*
mTSPC	*mouse tendon stem/progenitor cells*
NA	*numerical aperture*
NIH3T3 WT	*murine NIH3T3 fibroblast wildtype*
PBS	*phosphate buffered saline*
PFA	*perfluoroalkoxy alkane*
PGMEA	*propylene glycol monomethyl ether acetate*
phLFs	*primary human lung fibroblasts*
RT	*room temperature*
SEM	*scanning electron microscopy*
TPEFM	*two photon excited fluorescence microscopy*
TPS	t*wo-photon stereolithography*
YM	*Young's modulus*

List of Symbols

σ	*uniaxial stress*
ε	*strain*
λ	*wavelength*
τ	pulse length
f	repetition rate
θ_0	reference angle
θ_n	local orientation angle

1 Introduction

"Although nature commences with reason and ends in experience it is necessary for us to do the opposite, that is to commence with experience and from this to proceed to investigate the reason."
- ***Leonardo da Vinci*** (1452 - 1519)[11]

1.1 Motivation

The aspiration to understand the human body might go all the way back to the cradle of human kind. In the 19th century pioneers have started to decode the structure and composition of the human body and countless scientists have contributed to unveil the mechanisms behind the functionality of the human body ever since[12]. Thanks to ever more advancing cutting edge technologies, the scale on which we comprehend the individual components and their interactions has miniaturized[13]–[17]. Nowadays, we can not only observe these biological phenomena *in-* or *ex-vivo*, but we are also able to rebuild biological entities to some extent *in vitro*[15],[18]–[21]. This allows us to adjust and study the effects of isolated parameters such as matrix stiffness or composition on cell behavior and fate[22]–[24].

From 2D to 3D cell culture

While fundamental cellular processes have predominately been studied in 2D over the last decades, an interdisciplinary community, ranging from biophysics[25],[26], over imaging[27],[28], transcriptomics[29],[30], proteomics[31],[32], computer science[33]–[36] to digital fabrication methods[37]–[39] is increasingly devoting research to the unravelling of 3D tissue formation[1]. In contrast to standard 2D cell cultures based on cellular monolayers adherent to rigid glass or plastic substrates, these sophisticated *in vitro* 3D tissue models have been established as invaluable platforms to investigate the complexity of the extra cellular matrix (ECM)[1],[6],[24],[40],[41]. In this course, the 3D ECM has been identified to be in a dynamic

reciprocal interaction with adjacent cells rather than just a passive scaffold[1],[24]. While the 3D architecture of the ECM offers pivotal cues instructing cellular behavior and fate *in vivo*, the ECM itself is deposited, remodeled and resorbed by the cells[1],[24],[42]. Apart from biochemical and mechanical factors, the micro-scale 3D ECM geometry has been identified to guide cellular actions inducing tissue development, remodeling and homeostasis[6],[43]–[45]. Hence, controlling the 3D micro-environment *in vitro* with (sub-) cellular precision is indispensable to create instructive cell niches, which can evoke and control organotypical tissue development[1],[46].

By developing 3D models such as organoids, organs-on-a-chips or bio-printed scaffolds, we are now able to discover still unknown ECM correlations e.g. in the context of angiogenesis or early stage organ development[47]–[52]. Considering the high effort which has already been made in this field and how far we actually are from fabricating anything similar to a fully functioning human organ in the lab, it becomes clear to which extent nature has perfected the assembly and interplay of building blocks across all scales.

Towards the goal of engineering fully functioning organs, it is necessary to consider the smallest hierarchical level. One apparent example is the lung where gas exchange is governed by approx. 300 - 480 million alveoli, small air filled sacs with a diameter of aprox. 250 µm[53],[54].

In future, these simplified *in vitro* models of human tissues will function as personalized test platforms to access optimal patient specific therapy approaches[49],[55],[56] and eventually they can be scaled to fully functional human organs[39],[57].

1.2 Pulmonary Physiology

While every organ has a fine tuned architecture on the micro realm, specific organs highlight the urge for highly resolved features within the human body. These include the retina containing photoreceptor cells[58], the basal membrane separating fetal from maternal blood in the placenta[59], as well as the alveoli, which provide for the gas exchange between blood and air at the distal end of the lungs[1],[24].

Oxygen Supply

The supply of our organism with oxygen is essential to provide our basic cellular processes with energy. Oxygen rich air is breathed in through the nose and mouth into the lung (Figure 1, A) where it passes the branched conducting airway, including trachea, the bronchi, bronchioles and the alveoli branches (Figure 1, B) before arriving at the approx. 300 - 480 million air filled alveoli within the human lung[53],[60],[61]. Here, at the terminal respiratory

unit, a basal membrane consisting of collagen and elastin fibrils supports monolayers of pneumocytes forming the alveoli and is closely associated with the pulmonary capillary network including vascular endothelial cells. Through pores within this thin membrane, oxygen diffuses from the incoming air into the blood stream where it is further transported by red blood cells in exchange for waste carbon dioxide, which is constantly transported into the pulmonary capillary network from other tissues[53],[62] (Figure 1, C).

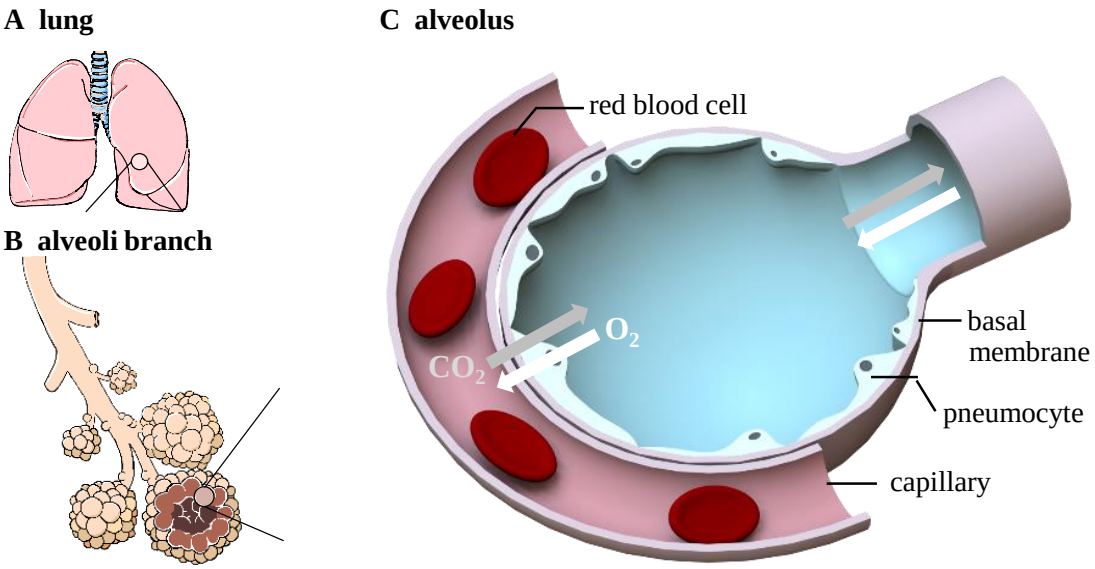

Figure 1: Schematic image of the alveoli. (A) The lung is the main organ of the respiratory system in humans. **(B)** At smallest end of the hierarchical structure are the alveoli branches including the alveoli, little air-filled sacs. **(C)** This is where the gas exchange takes place: Air is breathed in and O_2 is transported over the basal membrane lined with pneumocytes into the capillaries guiding red blood cells in exchange for CO_2, which is in turn is exhaled. (Images A, B adopted from Erben et al. 2020, image C adopted from Erben et al. 2022)

Alveolar Characteristics

Human alveolar functionality is characterized by several features (Figure 2). With a blood flow rate of approx. 2 - 5 nL/min in pulmonary capillaries[63],[64] and resulting mean velocities of approx. 1 mm/s, a shear stress at the capillary walls of approx. τ = 1.5 Pa is induced in healthy adult humans[65],[66]. To maintain sufficient baseline energy levels in large multicellular organisms, an enormous surface area of the pulmonary basal membrane is required, which, in the adult human, is estimated to be >100 m^2[53],[67],[68]. Alongside the very thin basal membrane, the ECM including 94 proteins provides the alveoli with their geometrical, mechanical and biochemical characteristics, with a stiffness measured as Young's modulus (*YM*) estimated to range from 1 – 2 kPa[69]–[71]. In diseased alveolar tissue such as idiopathic pulmonary fibrosis, the Young's modulus of the basement membrane can reach up to 35 kPa[69],[70]. The basal membrane provides an interface between air and

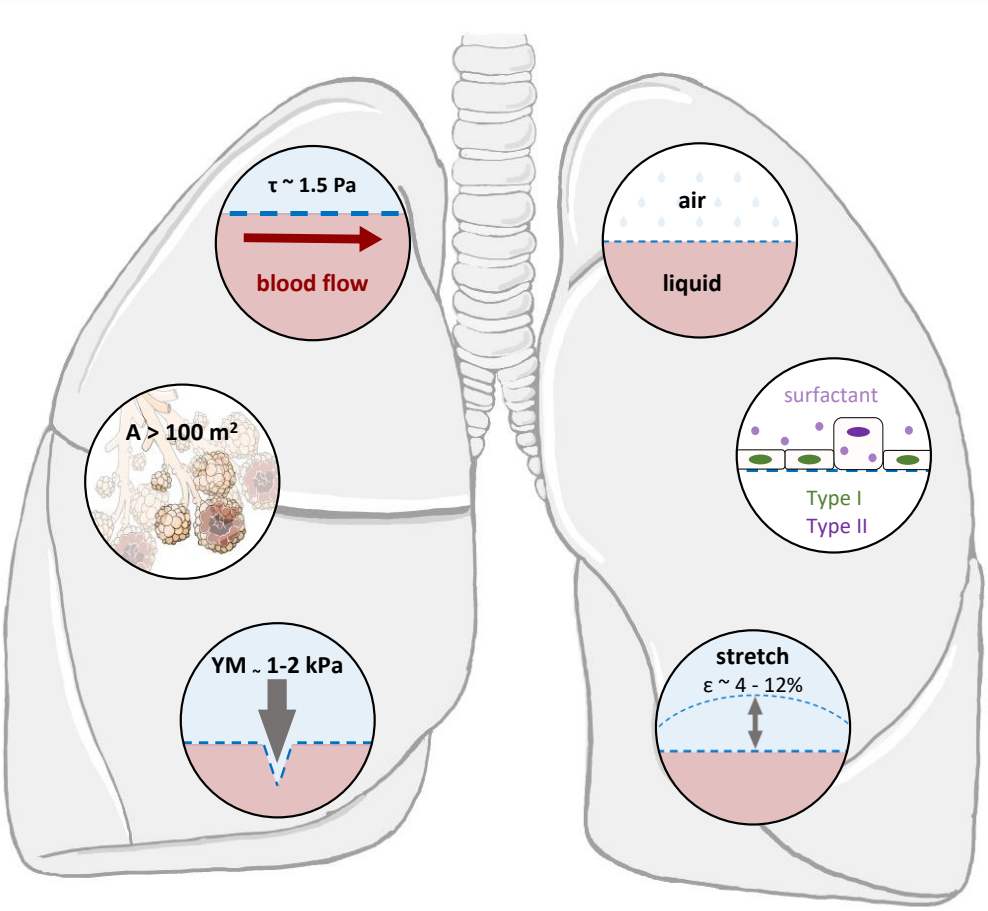

Figure 2: Features of the respiratory system. The respiratory system including the alveoli circumscribed by an interveined vasculatory system enables sufficient supply of oxygen throughout the human body. On the scale of the alveoli, this vital function is enabled by several characteristics: (1) blood flow in the capillaries results in a shear stress of approx. τ = 1.5 Pa; (2) a surface area of the basal membrane of > 100 m^2; (3) a stiffness measured as Young's modulus (YM) of 1 – 2 kPa in healthy tissue; (4) an air liquid interface separated by a thin basal membrane (5) lined with two types of pneumocytes on the alveolar side: Flat shaped type I cells (green) and cuboid shaped type II cells (purple) which secrete surfactant to reduce surface tension; (6) a ventilation induced by breathing which leads to a stretch of the basal membrane of approx. 4 – 12%;

liquid and is layered with two types of pneumocytes: flat Type I and cuboidal type II alveolar epithelial cells. Type I cells are prevalent with 90% coverage of the alveolar surface and are mainly involved in gas exchange and immune response, while type II cells secrete surfactants to decrease the alveolar surface tension.[53] The unique characteristic of the respiratory system is the continuous but dynamic mechanical forces generated by every in- and exhaling of air[69]. This ventilation results in a stretch of the basal membrane inducing a linear strain of 4 – 12% (at rest / heavy exercise) stimulating pulmonary epithelial and endothelial cells at approx. 0.2 – 0.55 Hz[65],[69],[72].

1.3 *in vitro* Alveoli Models

Sars-CoV-2 has fiercely underlined the importance of deeply understanding the respiratory system[73],[74]. However, already before the world wide pandemic in 2020, chronic respiratory diseases were one of the leading causes of death with a highest prevalence also in high-income regions[69],[75],[76]. In light of the urgent need to rigorously investigate these diseases and to speed up drug efficacy and delivery testing, a wide range of *in vivo* and *in vitro* lung test models have emerged[42]. In fact, ***in vivo* animal models** can represent complex inner-body coherences as they offer both native ECM components, such as proteins, cells and spatially defined growth factors as well as dynamic factors including physiological shear stress and mechanical stretch. Nevertheless, fundamental differences in lung physiology and anatomy between humans and animals exist. These include, among others, airway architecture and size, rates of alveolar epithelial fluid transport and biomarkers[53],[77]. Thus, it is not surprising, that despite sophisticated efforts, most drugs that prove to be successful in preclinical rodent studies fail to effectively treat human diseases in clinical trials[69],[78],[79]. Additionally, the role of biomechanical forces on lung development is rather difficult to study *in vivo*, but has been recognized to not only play a decisive role in lung development and regeneration, but has also shown to be crucial for disease onset, mitigation and chronicity. Cyclic mechanical stretch has been identified to alter cell proliferation, differentiation, secretion and migration by regulating downstream signaling pathways evoking modifications in gene expression and protein synthesis[69],[80],[81]. While mouse studies have shown dynamic ECM deposition and remodeling of collagen and elastin fibers by mesenchymal cells in cooperation with alveolar epithelial cells upon cyclic stretch during alveoli maturation, little is known about these factors influencing homeostasis and efficient gas exchange as well as regeneration and response to inhaled environmental and infectious agents in humans[65],[82]–[84]. In light of the necessity to accurately predict disease mechanisms and patient specific therapy success, ***in vitro* 3D alveoli models** have been developed and should mimic native alveoli tissue in at least one of the following physiologically relevant properties[69],[77]:

- ECM components including glycoproteins such as elastin, collagen, laminin, fibronectin, etc.[43],[77]
- Air liquid interface (ALI) incl. endo-/epithelial cells at the blood/air interface[68],[77]
- Large surface area of basal membrane at <1 µm thickness[67],[68],[85],[86]
- Young's modulus of 1 - 2 kPa (healthy) or up to 35 kPa (diseased)[69]–[71]
- Blood flow rate of approx. 2 - 5 nL/min[63],[64]
- Stretch induced strain of 4 - 12 % at 0.2 – 0.55 Hz[72],[77]

Current *in vitro* alveoli models only show a small fraction of the complex, dynamic and interacting processes which occur in the native alveolar tissue. However, they allow for

tightly controlled cellular environments, which can be scaled, reproduced and analyzed in real time, providing substantial advantages over both animal models and clinical studies. Depending on the desired level of complexity, these *in vitro* models can range from very simplistic to highly sophisticated models including:

- 3D hydrogels[87]
- Air liquid interface (ALI) cultures[88]–[93]
- organs / tissue / cells-on-chips[53],[94],[95]
- spheroids / organoids[96]–[98]
- biological / ex-vivo scaffolds[24],[43]
- bio-printed scaffolds[99]–[101]

all of which have their very own (dis-) advantages[53],[77].

By culturing cells in **3D (photo-) hydrogel matrices**, cells are exposed to micro environments mimicking the native ECM. Further, cell guidance can be achieved in such systems by means of stiffness gradients[87],[102],[103]. However, sufficient oxygen and nutrient supply is critical for cell survival in thick hydrogel matrices[104],[105]. While 2D protein-coated **glass or plastic substrates** allow for the investigation of the effects of a great variety of ECM molecules on cellular monolayers, the stiffness of such substrates (cell culture plastics: 2 - 4 GPa) vary significantly from both native healthy alveolar tissue (~1 - 2 kPa) as well as fibrotic tissue (< 35 kPa)[43],[61],[70],[106]. More realistic monolayer models embed an **air-liquid interface** by culturing vascular endothelial cells in liquid medium on one side of a membrane, while alveolar epithelial cells are cultured in a humid environment on the opposite side of the membrane. These co-culture systems have considerably contributed to an advanced understanding of mucus secretion and have revealed the effects of external toxins such as cigarette smoke on lung tissue[93],[107]. ALI models have further been extended by microfluidics, which provide for a controlled regulation of spatiotemporal oxygen, nutrition and chemical gradients, as well as physiological shear stress and stretch[77],[89]–[91],[108],[109]. These **cells/organ-on-a-chip** systems are easy in handling and allow the investigation of biological and biochemical processes at the micro scale. Further, they are highly parallelizable and standardizable and thus beneficial to obtain reproducible and quantitative results[77],[90]. However, ALI culture systems are unable to simulate the complex 3D geometry of alveolar tissue and membranes are most often not entirely fabricated from ECM derived proteins. **Spheroids and organoids** rely on the self-organization of specific cells, which can be programmed to form simplified, microscopic 3D versions of organs. They have emerged to a coming of age technology to recapitulate vital and diseased tissue and have proven to reliably reflect therapeutic responses[6],[53],[110]. The limitations of spatial patterning, as well as tight control over the distribution of biochemical and mechanical cues across these 3D spheroids and organoids are increasingly being considered a major constraint in developing sophisticated

organ[53],[111]. The intricate ECM structure plays a key role in shaping the cellular microenvironment by offering structural cues, regulating growth factor supply and controlling cell adhesion and migration[62],[112],[113]. Efforts towards more biomimetic *in vitro* alveoli models have spawned **biological/ex-vivo scaffolds**, from which we have now gained most of our understanding about the human respiratory system, apart from rodent studies. These tissue samples obtained from mammalian lungs, which are decellularized and subsequently reseeded with human pulmonary cells, allow for a realistic model in respect to native ECM composition, cell types and geometry. However, these tissue samples are rather difficult to obtain from healthy humans. Furthermore, lifestyle, genetic, protein/carbohydrate composition and remaining growth factor variability between individuals must be taken into account for all acquired findings aggravating reproducibility and generally valid conclusions. Additionally, necessary chemical treatments can impair ECM properties such as Young's modulus or biochemical composition[53]. Consequently, **bioprinting** approaches have emerged as a powerful tool to spatially define and position cells and micro environments with precisely defined properties, stimulating cells to mimic native tissue. By tailoring both bioprinting parameters or hydrogel resin composition physical and chemical ECM properties such as stiffness and cell binding sites can be adjusted[62]. Besides applications in liver[114],[115], heart[57],[116],[117], kidney[118], skin[119]–[121], lung[122],[123] and various cancer models[124]–[126], bioprinting has been used to fabricate lab-grown model systems mimicking alveolar function[53],[99],[101],[127]. These include layered (barrier) models recapitulating the native blood-air barrier printed using inkjet or contact dispensing[100],[127]. While droplet-based bioprinting methods succeed in directly printing cells and ECM derived hydrogels into high-resolution patters, these approaches are limited to a small variety of low viscosity inks, the reproducibility is low and cells experience extreme shear stresses within the nozzle[9]. Using extrusion-based 3D biopronting, cell-laden bioinks have been integrated into a PDMS chamber to assemble an airway-on-a-chip promoting early vasculogenisis. This platform was used to explore cytokines in asthma and has closely mimicked *in vivo* pathophysiological mechanisms[53],[128]. One limitation of extrusion printed models is the overall rigid flat shape, despite its 3D layering, thus not recapitulating the native geometry of alveolar tissue[100]. Furthermore, this is a layer-by-layer process with a defined layer resolution, which may result in stair-stepping effects which in return may result in occlusion or turbulence of the flow[9]. Strikingly, Grigoryan et al. have developed a computer derived alveoli model from space filling mathematical topographies, printed using one-photon stereolithography, to study oxygenation and flow of human red blood cells during tidal ventilation and stretch. These results beautifully demonstrate the feasibility of the new generation of hydrogel derived organ-on-a-chips, mimicking native tissue also in 3D geometrical cues. However, Grigoryan et al. use synthetic hydrogels which are lacking both native biochemical and mechanical cues with a resolution of 2 - 10x larger compared to native alveoli[99] and this platform is currently lacking *in vitro* cell colonization of printed structures.

1.4 Challenges in Bioprinting of Alveolar High Resolution 3D *in vitro* Models

Despite various approaches to fabricate *in vitro* alveolar models, their success in establishing functional, physiologically relevant as well as mechanically and structurally stable constructs across all scales varies significantly[9]. As a result, most alveolar *in vitro* 3D tissue models show only limited functionality based on the lack of providing the full set of native properties. These limitations include a relatively low number of simultaneously co-cultured cells, the lack of multi-dimensioned, branched micro vascular networks as well as non-sufficient integration of the ECM architecture both in terms of fabrication and design[105]. The situation is aggravated by the fact that common standards ensuring reproducibility and comparability have only been established for 2D culturing techniques. By extending tissue models to 3D, additional variables are introduced, essentially complicating the redefinition and establishment of these standards[6]. In particular, current *in vitro* alveolar 3D models have at least one of the following limitations:

Cell Culturing

Up to now, mostly only low numbers of cell types have been included in 3D bioprinted scaffolds[129]. In comparison, the native ECM of the lungs is populated by about 60 different cell types[69]. However, to achieve a sufficient number of regeneration-competent cells that do not induce an immune response upon transplantation is a strongly addressed challenge. One method to obtain patient-derived cells for biofabrication is the expansion of harvested autologous primary cells *in vitro.* Unfortunately, not all primary cells are easy to isolate, expand and handle and tumorigenicity remains as one of the most significant risks. However, a multitude of strategies and protocols to handle cell sourcing limitations are constantly being developed towards safe and efficient phenotypic tissue models[129]. Additionally, technologies such as laser induced forward transfer must be advanced to sophisticate the precise distribution of various cell types throughout highly hierarchical scaffolds[9],[130].

Imaging

Larger and more complex structures also require advanced imaging techniques allowing for time-resolved, high-resolution and non-destructive analysis and quality control. While the visualization of 3D constructs with one-photon fluorescence is not sufficient to fully resolve all three spatial dimension[131], advances in fluorescence labelling and detection including confocal[132], two-photon[133] and light sheet microscopy[134],[135] have emerged to image greater volumes at high resolution over extended periods of time[26]. Additionally,

non-fluorescent microscopy technologies such as opto-acoustical, Brillouin[16] or high energy x-ray imaging[136] are becoming increasingly powerful as accurate analysis tools in optical *in vitro* 3D tissue model analysis. With the development of improved imaging methods with high resolution of ever larger imaging sections, both the quality of native print templates as well as the non-destructive real time analysis of *in vitro* tissue models are constantly being improved. These advances come with the acquisition of large 3D data sets which must be analyzed, interpreted and also stored requiring powerful computers, customized software, AI algorithms and large data storage capacities[137].

Biomimetic Print Templates

In nature, growth usually follows patterns such as branching phenomena, which can be mathematically described by bioinspired algorithms such as Mandelbrot's fractal model[138], the reaction-diffusion model based on Turing instability[138] or digital morphogenesis[139]. Using additive manufacturing to recapitulate native ECM structure requires information rich print templates mimicking native tissue in geometry, mechanical and biomechanical properties. Up to date such templates solely carry the geometric design information and are typically generated using a computer aided design software (CAD) or native tissue scans[10],[140]. Using datasets derived from native tissue certainly allows for accurate mimicry of native ECM architecture[1],[141],[142]. However, these models lack parametrization and therefore it is difficult to systematically adjust individual design features such as wall thickness[10],[143]. While CAD software can be used to design parametrized models, it was originally designed to support traditional subtractive fabrication techniques rather than additive manufacturing. Hence, it is not surprising that current CAD derived templates typically lack organic design and thus significantly differ from their native counterpart[10],[141],[144]–[146].

3D ECM Micro Architecture

With the introduction of additive manufacturing to the field of tissue engineering, the design complexity of lab grown 3D tissue models has enhanced. Volumetric bioprinting[147] and one-photon stereolithography[99] enable the rapid fabrication of clinically relevant scaffolds by polymerizing photo-activatable, protein based resins at two-digit µm resolution[99],[147]. However, to orchestrate the ECM ultrastructure, fabrication methods with the ability to fabricate arbitrary 3D structures at sub cellular resolution are in demand[1]. While droplet-based printing methods such as inkjet printing[148],[149] or laser induced forward transfer[130] allow for the precise deposition of droplets containing cells and/or ECM-derived hydrogels, these techniques are rather time consuming and cells suffer from extreme shear stresses during deposition[9]. Electrospinning is a versatile technique to structure finely controlled nanostructures at a resolution well below cell size. However,

electrospinning does not allow for the fabrication of arbitrary, complex 3D structures [150],[151].

1.5 Two-Photon Stereolithography

With TPS spatial polymerization of proteinaceous resins can be precisely controlled to achieve arbitrary 3D cell scaffolds from photo-activatable protein-based resin achieving single-digit µm resolution[1],[130],[151],[152]. As a laser-based 3D printing technique, it also allows for the precise tuning of scaffold stiffness which is correlated with cross-linking density, simply by adjusting the introduced laser energy[1],[37].

In brief, two photons within the focal spot of a pulsed laser are required in spatial and temporal proximity to simultaneously induce a chemical reaction in TPS. This reaction, underlying a nonlinear absorption process, is triggered by a photo initiator which is designed to be transparent at the laser wavelength. Consequently, a local polymerization of monomers present in the solution is only induced where the spatiotemporal density of photons is sufficient to induce simultaneous absorption of two photons. This high temporal density of photons at twice the wave length (half the energy) is obtained by using an ultra-short pulsed laser. This leads to a spatially constrained solidification of the resin only within the polymerizing voxel. It follows, that wherever the laser focus has passed within the photo reactive resin with sufficient energy, a solid structure emerges, which can subsequently be freed from the excess resin by means of a development and washing process[37],[153] (Figure 3, A). Therefore, TPS is suitable to fabricate complex, highly

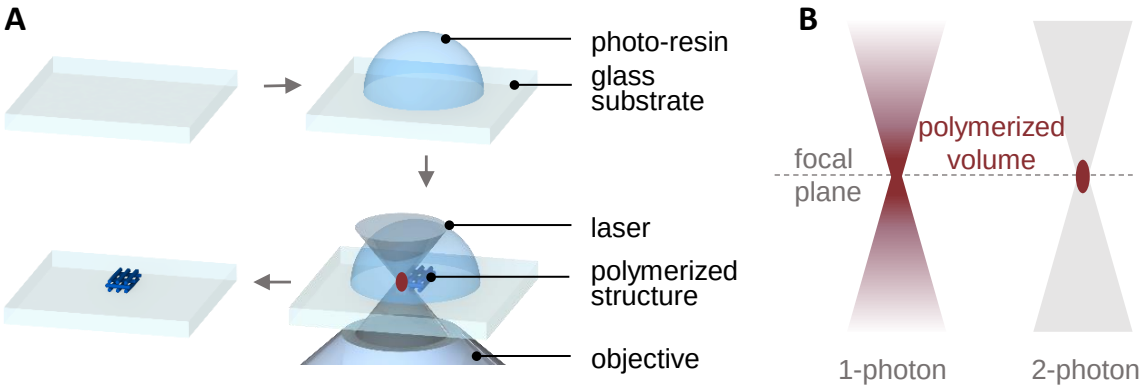

Figure 3: Two-photon stereolithography (TPS). (A) The workflow of TPS entails casting of a photo-resin on a glass substrate, followed by selective laser exposure. The laser is focused by an objective and polymerization only occurs within a focused voxel (red). The resulting polymerized 3D structure is subsequently developed by means of a washing process. **(B)** While in one-photon stereolithography (left) the laser beam is absorbed along the focalization cone, the polymerized volume is restricted to a defined ellipsoidal volume (voxel) in TPS (right). This enables the fabrication of complex, high-resolution 3D structures with TPS.

resolved 3D structures in contrast to one-photon stereolithography where the excitation is not limited to a confined voxel (Figure 3, B).

Two Photon Stereolithography in Life Sciences

By functionalizing with respective cell-mediating bio-molecules, TPS scaffolds fabricated with standard acrylic-based photo-resins have recently been utilized to guide cell adhesion[154], cardiomyocyte differentiation[155] and neuronal networks[156],[157]. However, acrylic-based photo-resin properties, including Young's Modulus (YM) as well as specific cell binding domains, significantly differ from native ECM. Hence, the introduction of ECM derived proteins such as gelatin[58],[158]–[160], silk fibroin[161],[162] or bovine serum albumin[152],[163],[164] paired with biocompatible photo initiators including rose bengal[165]–[167], methylene blue[58],[161],[168] and lithium phenyl-2,4,6-trimethylbenzoylphosphinate (*LAP*)[59] to TPS offers exciting prospects for the design of information-rich micro cell niches[1],[169]. By adapting resin composition or fabrication parameters, such as the laser power and scan speed, the mechanical properties of these cell niches can be tuned to mimic native tissue, as *YM* values have been reported ranging from 2 – 220,000 kPa[1],[162],[170]. Therefore, TPS poses a high potential for the recreation of highly resolved tissue segments such as the retina[58],[171], the placenta[59] or the alveoli[1], potentially allowing for quantitative *in vitro* studies regarding biological processes, interaction and guidance within high-resolved tissues.

However, in TPS print time is inversely linked to achievable print resolution[147] limiting typical print volumes of proteinaceous scaffolds with single digit µm resolution to < 0.03 mm^3[58],[164],[165],[172]–[174]. Furthermore, post-crosslinking and processing parameters have not been taken into account when quantifying the stiffness of TPS printed cell scaffolds. While channels with 10 µm resolution have been demonstrated, these channels are encased in rigid microfluidics and can not be individually contacted for perfusion, thus limiting selective perfusion of high precision scaffolds.

1.6 Hypothesis

As depicted in section 1, 3D *in vitro* tissue models mimicking the vital or pathological microenvironment of cells in various traits are required to fundamentally understand cellular behavior and fate in their natural environments. As the ECM's geometry, as well as mechanical and biochemical properties have been ascertained to play a crucial role for tissue functionality, there is an urge for high-resolution printing techniques, allowing for the fabrication of proteinaceous 3D cell microscaffolds mimicking the ECM. To my knowledge, TPS is the only bioprinting technology, which can structure proteinacous resins

at a single-digit resolution in a highly controlled manner. Within the scope of this doctoral thesis, the TPS workflow was improved for life science applications. Further, the extent to which TPS is suitable to recapitulate the microstructure of native tissues in respect to geometry, composition and mechanics was investigated. In particular, the following research questions were addressed, by merging 3D fabrication, life science and imaging expertise based on the example of alveolar tissue:

(1) *Can clinically relevant high-precision scaffolds be fabricated using protein formulations while maintaining sub-cellular resolution?*

(2) *Are these high-precision cell scaffolds compatible with various cell types and are they suitable for standard 2D and novel 3D cell assays (e.g. actin filament orientation)?*

(3) *Do the fabricated high-precision cell scaffolds resemble native (alveoli) templates in topographical and mechanical properties?*

(4) *Can high precision cell scaffolds be individually connected to standard microfluidic systems to allow for cell seeding and active perfusion?*

(5) *What is the achievable resolution of protein-based micro channels fabricated with modified gelatin methacryloyl (GM10) resin using TPS?*

(6) *How can parametrized print templates with an organotypical alveoli design be derived, including an interveined capillary system which additionally supports microfluidic contacting of both alveoli and capillaries?*

1.7 Overview of this thesis

This doctoral thesis consists of the following main chapters: **Chapter 1** is an introductory chapter on high-resolution 3D *in vitro* tissue models. Particular attention is paid to pulmonary tissue and the state of the art of *in vitro* alveoli models as well as remaining

factors required for enhanced imitation of the functional tissue followed by the research questions to address these needs. In **Chapter 2**, fabrication, cell culture, analysis and statistical methods applied or developed throughout this research are described. **Chapter 3** gives a summary of the peer reviewed first-author papers published within the scope of this doctoral thesis. Finally, in **Chapter 4**, the strengths and weaknesses of the introduced approach and possible future perspectives are discussed.

2 Materials & Methods

In this chapter, the experimental methods and used materials as well as all data analysis approaches are briefly described. Most passages and images describing the methods are adapted from previously published publications (Erben et al. 2020[1], Erben et al. 2022[10]).

2.1 Scaffold fabrication

Microscaffolds were either designed using CAD software SolidWorks (Dassault Systèmes, 2017), Hyperganic Core 2.0 (Hyperganic Group GmbH, 2021) or by datasets obtained by using confocal microscopy. Respective files were converted to STL files which were further processed to print job instructions using the Describe software (Nanoscribe GmbH, 2019) (Figure 4). Slicing (z) and hatching (x/y) distances of individual layers of 0.3 µm and 0.2 µm for 63x objectives (numerical aperture (NA) = 1.4) and 1.0 µm and 0.5 µm for 25x objectives (NA = 0.8) were selected. Selective exposure was carried out with the Nanoscribe GT Photonics Professional equipped with an erbium-doped femtosecond laser source with a center wavelength of 780 nm and a maximum power of about 150 mW (all Nanoscribe GmbH). Standard operating mode was the dip-in configuration using protein-based resins (composition described in the following) to achieve in theory arbitrary print heights (Figure 5, A). This operating mode is in contrast to the bottom-up configuration, where print heights are limited to the working distance of the objective. 3D printed microscaffolds, which were further colonized with cells, were commonly printed in 35 mm petri dishes (MatTek, No. 1.5), each equipped with a centered, 160 - 190 µm thick glass slide. Petri dishes were fixed onto the sample holder using double sided adhesive tape with openings facing towards the objective in a way that the petri dish was circumferentially

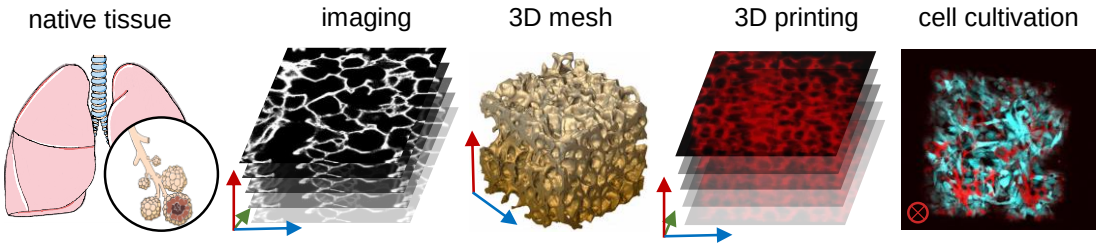

Figure 4: Workflow for biological 3D precision printed scaffolds. Here, alveolar tissue within the respiratory system was used as an example for sub-cellular ECM topographies. Native tissue was imaged using high resolution techniques such as confocal microscopy. After imaging, the data set was converted to a 3D mesh which was further translated into a 3D printer instruction code by a slicing software. Finally, the 3D template derived from native tissue was printed with highest precision in a layer-by-layer fashion using two-photon stereolithography and the scaffold (red) was subsequently colonized with cells (blue). (Figure adapted from Erben et al. 2020)

aligned with the circular notch in the substrate holder (Figure 5, B). For additional securing, petri dishes were fixed to the sample holder using multiple strips of one-sided adhesive tape (Nanoscirbe GmbH). The objective seal was designed with the CAD software SolidWorks (Dassault Systèmes, 2017) allowing it to fit tightly on the 25x objective. The reservoir filled with double distilled water during the printing process, was designed to fit the rim of the petri dish. The objective seal was printed with a Form2 3D printer using Flexible Resin V2 (both Formlabs GmbH). All AFM samples were printed on 170 µm thick square glass cover slips with 22 mm edge lengths. After completing the printing job, 3D prints were developed by removing all residual resin with phosphate-buffered saline (PBS) and stored in PBS containing 1% penicillin-streptomycin at room temperature (Figure 5, C). To enhance cell adhesion, most microscaffolds were coated with 50 µL of

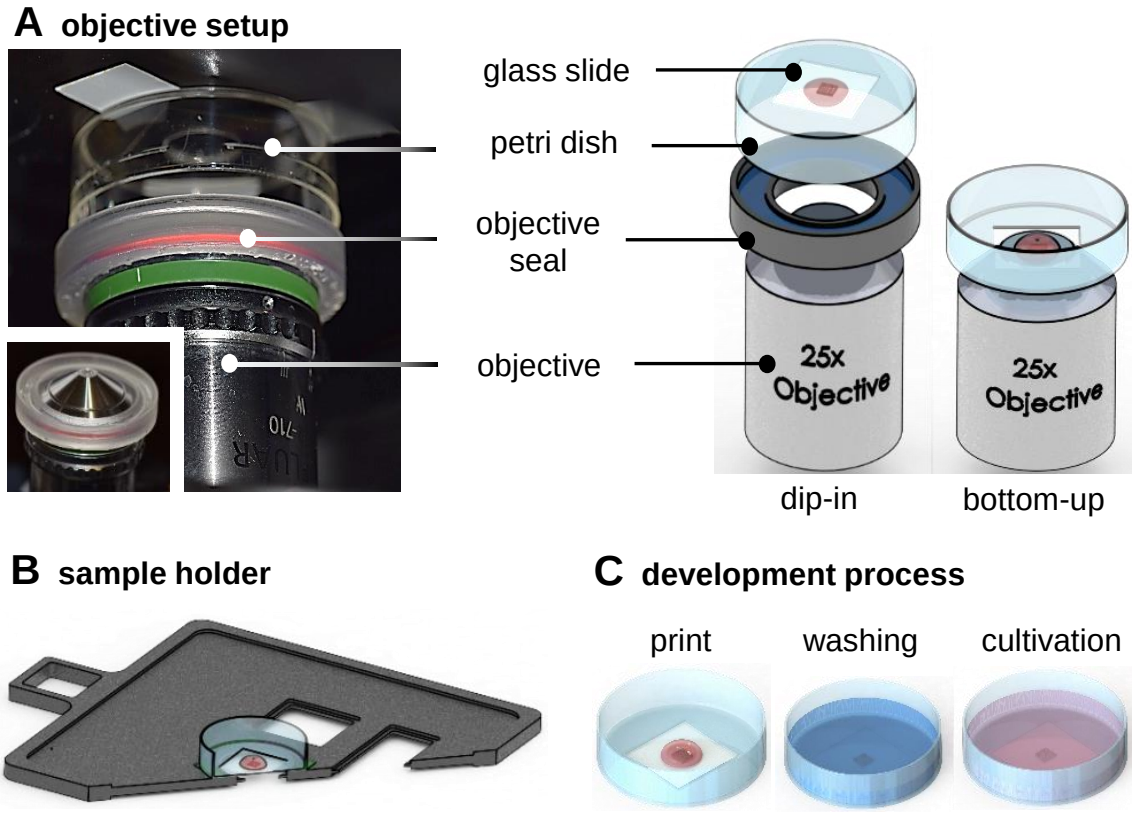

Figure 5: Dip-in vs. bottom up TPS printing mode. (A) The objective setup, optimized for the fabrication of cell scaffolds with sub-cellular precision: By dipping the objective into the drop of resin (dip-in setup), the working distance can be subsequently adjusted allowing for the fabrication of prints exceeding 230 µm. In contrast, the laser is focused through the substrate for the standard bottom-up setup established for protein-based resins. As the evaporation of water-based protein resins limits consistent print quality, a custom designed objective seal containing water was designed and installed, significantly increasing print time and thus print volume. **(B)** All scaffolds used for cell culture, were printed directly into glass-bottom petri dishes to implement biological standards and facilitate downstream handling. Therefore, petri dishes (light blue) containing 0.17 mm thick glass slides were aligned with the sample holders (grey), fixated using adhesive tape and photo-resin (red) was subsequently pipetted onto the center of the petri dish (Nanoscribe GmbH). **(C)** After printing, residual resin (red) was washed from the microscaffold with PBS (blue). Finally, cells were cultivated on microscaffolds in respective cell culture medium (pink) (Figure A from Erben et. al. 2020)

a solution containing 100 µL mL^{-1} of the ECM glycoprotein fibronectin (AppliChem GmbH) for 30 min at room temperature (RT). After rinsing excess fibronectin from samples with PBS, petri dishes were filled with 2 mL of cell specific medium composition (described in the following) and drop-seeded with 50 - 100 µL of cell suspension with a cell density of approx. 5 x 10^6 cells mL^{-1} [1],[10].

2.2 Cell Handling & Staining

Cells were handled with the following protocol, unless specified otherwise: Cells were cultured in Dulbecco's Modified Eagle Medium (DMEM; BS.FG 0445, Bio&SELL GmbH) supplemented with 1% Penicillin/Streptomycin (BS.A 2213, Bio&SELL GmbH), 10% fetal calf serum (F7524-500mL, Sigma-Aldrich Chemie) and 1% GlutaMAX (35 050 038, Life Technologies GmbH) under humidified conditions at 37 °C and 5% CO_2. Cell culture medium was exchanged every 2 - 4 days. Upon cell confluency of 80 – 90%, cells were passaged using 0.5% trypsin-disodium ethylenediaminetetraacetic acid (EDTA) solution (BS.L 2163, Bio&SELL GmbH), centrifuged at 500 rpm for 5 min at room temperature and finally seeded in a ratio of 1:5 or 1:6 in T175 cell culture flasks (83.3912.002, Sartstedt AG und Co.). For microscaffolds containing cells which were not fluorescently labeled, colonized scaffolds were fixed with 3.7% - 4% paraformaldehyde (PFA) for 15 min (37% paraformaldehyde, CP10.1 Carl Roth GmbH + Co. KG), rinsed with PBS, permeabilized with 0.1% Triton-X-100/PBS (Sigma Aldrich, Lot. SLBM1396V/Lot. SLBM1396V) for 2 - 10 min, again rinsed with PBS. Subsequently, actin cytoskeletons were stained with 10% ATTO 594 phalloidin/PBS (ATTO-TEC, Lot. SA02T25F8) for 15 min or Alexa 594 phalloidin for 1h. Cell nuclei were stained with 10% 4′,6-diamidino-2-phenylindole (DAPI, AppliChem, Lot. 7QD13667) for 15 min. Scaffolds were rinsed with PBS between each work step and rinsed three times after staining. To increase stability, fixed microscaffolds were coated with a drop of Abberior Mount Solid Antifade (Abberior, Lot. MM-2013-2 × 15 mL). All procedures were performed at RT. For staining of C2C12 cells, cell-loaded scaffolds were quenched with 1 M Glycine in PBS for 5 min after fixation with PFA and blocked with 5% fetal calf serum in PBS for 30 min after permeabilization. Cell nuclei of C2C12 cells were stained with DAPI (5 mg mL^{-1} stock; final concentration 300 nM) during the last washing step and incubated for 5–10 min at RT [1],[10].

phLFs

Primary human lung fibroblasts were isolated by outgrowth from human lung tissue obtained from lung explants or tumor-free areas of lung resections. phLFs were cultured in DMEM F-12 containing 20% (v/v) special processed fetal bovine serum (PAN Biotech),

100 International Units mL^{-1} Penicillin and 100 µg mL^{-1} Streptomycin. Cells were used for experiments to a maximum of 7 passages[1]. Human biomaterial and clinical data was kindly made available by the CPC-M bioArchive and its partners at the Asklepios Biobank Gauting, the Ludwig-Maximilians-University Munich (LMU) and the LMU hospital. A written broad consent to participate in this study was obtained from all participants, in line with consent by the local ethics committee of the LMU, Germany (Project 333-10, 454-12)[1].

NIH3T3 WT

Murine NIH3T3 fibroblast wildtype cells expressing Lifeact-RFP (rLV-Ubi-LifeAct Lentiviral Vectors, ibidi GmbH) were kindly provided by Prof. Christof Hauck and Timo Baade (University of Konstanz). Cells were cultured at 37 °C and 10% CO_2 in DMEM growth medium (Biochrom) complemented by 10% fetal calf serum (Biochrom), 1% GlutaMax (Gibco) and 1% Penicillin/Streptomycin (Biochrom)[1].

mTSPC

Mouse tendon stem/progenitor cells originally isolated from WT and Tnmd KO mouse tail tendons at 6, 9, 12, and 18 months of age[175],[176] were kindly made available by Prof. Dr. Denitsa Docheva and Manuel Delgado Cáceres (University of Regensburg). Respective culture medium DMEM/HAMs F-12 (Biochrom F4815) was supplemented with 1% GlutaMAX (Thermo Fisher Scientific), 10% fetal bovine serum (Biochrom), 1% non-essential amino acids (REF 11140-035, gibco), 1% Penicillin/Streptomycin (Biochrom) and ascorbic acid 2-phosphate (5.8 mL of 36 mg mL^{-1})[1].

HUVECs

Human umbilical vein endothelial cells (pooled donors, cryopreserved, C-12203) were cultured in endothelial cell growth medium (ECGM 2, Promo- Cell GmbH)[1].

C2C12

Mouse myoblast cells (<20 passages, Sigma-Aldrich) were cultured in DMEM (D6046, Sigma-Aldrich) supplemented with 10 wt% fetal bovine serum (F4135, Sigma-Aldrich) and 1% Penicillin/Streptomycin (P0781, Sigma-Aldrich)[177],[178].

2.3 Imaging

Bright-field and epifluorescence microscopy

Bright-field and fluorescence images of scaffolds colonized with hMSCs, HUVECs, mTSCPs and NIH2T3 WT cells were obtained by the ZEN blue software (Zeiss, 2009) using the AxioObserver.Z1 (Zeiss). Time lapses were acquired by using EC Plan-Neofluar DIC 10×objective (NA 0.3, Carl Zeiss) while cells were cultured in respective cell culture medium compositions in humidified conditions at 37°C and 5% CO_2 in a PM S1 incubator chamber (Zeiss) or Incubator PS compact with heating incubation insert (Pecon GmbH)[1].

Confocal Microscopy

Confocal z-stacks of microscaffolds colonized with various cell types were recorded with an inverted confocal Spinning Disk Microscope (Zeiss AxioObserver SD) equipped with Yokogawa CSU-X1 Spinning Disk UnitFastScan Confocal Fluorescence Microscope, using 20x (ZEISS Plan-APOCHROMAT 20x, NA0.8) and 40× objectives (ZEISS Plan-APOCHROMAT 40×, NA 1.4 Oil Dic (UV) VIS–IR) and an EMCCD camera (Photometrix Evolve 512). DAPI was excited with a 405 nm diode laser combined with a 450/50 nm emission filter. Alexa594 was excited with a 561 nm diode laser combined with a 600/50 nm emission filter. For large constructs, image tiles of up to 4 × 4 with a 10% overlap were captured and reconstructed using ZEN (Vers. 2.3). For tiled images the ImageJ BaSiC shading correction plugin was applied[1],[179].

Stereomicroscopy

Stereomicroscopy was used for the assembly and analysis of the bio-hybrid perfusion chip. All stereomicroscopic images were performed with a Wild epi-microscope M450 (Leica Microsystems GmbH)[10].

Two-Photon Microscopy

High resolution images of TPS printed scaffolds using proteinaceous resins were performed using a custom made two photon excited fluorescence microscope (TPEFM). The optical setup was configured using a Nikon Eclipse Ti2 body and an ultrashort pulsed laser (FemtoFiber Dichro Design, TOPTICA Photonics AG) with wavelengths of $\lambda_1 = 1034$ nm and $\lambda_2 = 780$ nm, a maximal laser power of $P = 100$ mW, a pulse length of $\tau = 95$ fs and a repetition rate of $f = 80$ MHz . The two beams were combined by a dichroic mirror (F38-825, AHF Analysetechnik) previous to coupling into a resonant-galvo scanner system (Multiphoton Essential Kit, Thorlabs). Laser scanning was achieved by a water immersion objective lens (CFI Apo MRD77200, Nikon) with a magnification of 20x and a numerical aperture of 0,95. The fluorescence signal emitted by the sample was collected by the objective lens in epi direction, before it was deflected from the illumination

beam path by a dichroic mirror (FF825-sDi01, Laser2000). The detection was carried out in a non-descanned configuration, using two InGaAsP photomultiplier tubes (Multiphoton Essential Kit, Thorlabs). An additional dichroic mirror (HC 735 LP, AHF Analysentechnik) in the detection path split the fluorescence signal in blue and red spectral ranges. Filters in the blue (F76-594, AHF Analysetechnik) and red (AT 600 LP, AHF Analysetechnik) channels were used as clean up filters for the emission signal. Two multiphoton filters (F39-745, AHF-Analysetechnik) blocked the excitation wavelengths to ensure low background signal and noise contribution[10].

Scanning Electron Microscopy

TPS fabrication success of adapters printed with acrylate-based IP-S resin was optically analysed using scanning electron microscopy (SEM). After sputtering samples with platinum for 45 s, images were recorded using a LYRA3 (Tescan Orsay Holding) with a voltage of 4.0 kV in high vacuum[10].

2.4 Atomic Force Microscopy

The stiffness of a material can be expressed by the Young's Modulus (*YM*), which is defined by the ratio of the applied uniaxial stress (σ) and the resulting strain (ε). This material value can be quantified using indention type AFM (IT-AFM). By indenting a substrate with a ~20 nm tip fixed to the end of a cantilever spring, the deflection of the cantilever and thus of a laser beam, which is reflected from the backside of the bent cantilever, can be detected by a segmented photodiode (Figure 6). Using both the indentation depth and the resulting cantilever deflection, the respective applied force can be calculated and displayed as force-indentation curve. By applying a fit model to these force-indentation curves, the *YM* can be estimated[1]. Here, the Sneddon-Hertz model was applied[180]. IT-AFM measurements were conducted using a MFP-3D Bio AFM (Asylum Research, Oxford Instruments, Goleta, CA, USA) on TPS printed microscaffolds measuring 90 µm x 90 µm x 11 µm and fabricated from various resin compositions. Glass cover slips containing these microscaffolds were mounted on microscope slides with thermostable wax in order to fit the IT-AFM sample holder. AFM indentation experiments were performed in PBS at RT using MLCT cantilevers (Bruker Corporation, Billerica, MA, USA; Cantilever D) containing a four sided pyramid tip and a nominal spring constant of 0.03 N m^{-1}, as specified by the manufacturer. The actual cantilever force constant was determined before experiments for every utilized cantilever using the thermal noise method[181]. All measurements of microscaffolds printed with GM10-LAP resin composition entailed 20 x 20 force-distance curves recorded in a 20 x 20 µm scan area at a

z-piezo velocity of 8 µm s^{-1}. A sampling rate of 25 kHz, a 2 V trigger point and a full z-piezo travel distance of 6 µm were selected. For measurements of microscaffolds printed with BSA-RB, 16 x 16 individual points were measured in a 40 x 40 µm region, the z-piezo velocity was reduced to 5 µm s^{-1} at a sampling rate of 3.5 kHz and the full z-piezo travel distance was set to 5 µm. The Young's modulus was derived by fitting the indentation section of the resulting force-indentation curves[182],[183]. Data acquisition was conducted with the Igor Pro software (version: 6.3.7.2) and data analysis with custom-programmed MATLAB scripts (Mathworks)[184]. All histograms were plotted using python 3.7 in Spyder (version 4). Mean *YM* values (µ) and standard deviations (σ) of all data points were calculated. For visualization, Gaussian curves defined by µ and σ were plotted. For additional cross-linking, scaffolds were incubated in 10 mM Genipin (>98 % HPLC powder, Sigma, G4796) dissolved in PBS[1].

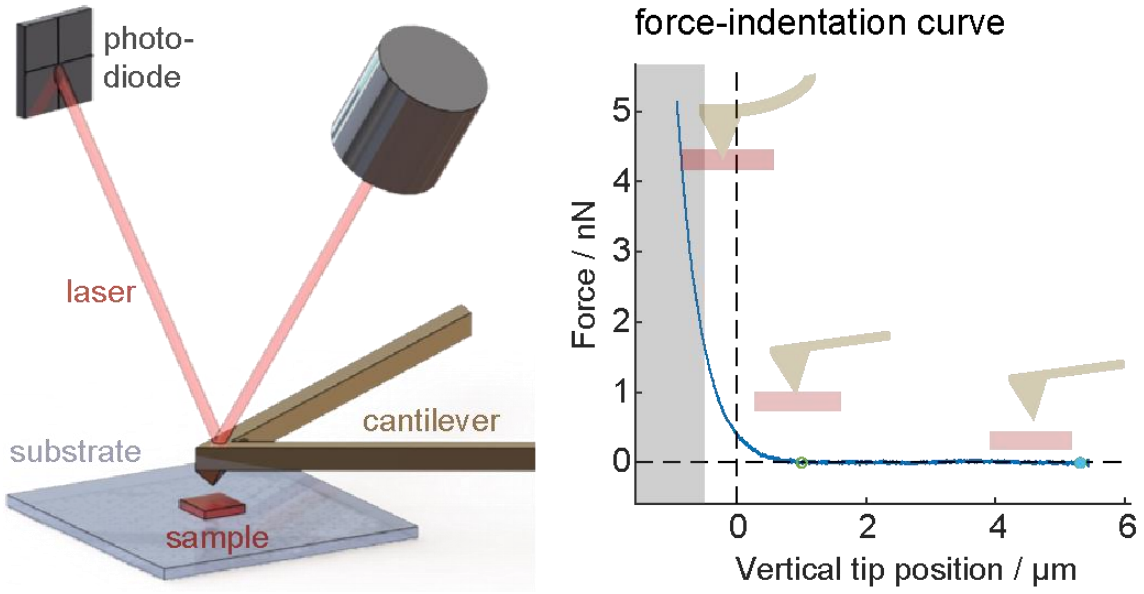

Figure 6: Atomic Force Microscopy (AFM) workflow. AFM (left image) was used to quantify respective Young's moduli of high-precision printed cell scaffolds. Therefore, a tip at the end of a cantilever (brown) was indented into a sample (red) adherent to a glass substrate (grey). By detecting the deflected laser beam (red) with a photodiode (grey), the Young's modulus can be derived with the help of the spring constant of the cantilever resulting in a force indentation curve (right image): While the cantilever is approaching the sample (blue curve, here: vertical tip position >1 µm), no force is applied. Upon first contact between sample and cantilever (here: vertical tip position ~1 µm) a force is applied and increases exponentially with vertical tip position (here: vertical tip position <1 µm). This curve is subsequently fitted to determine the Young's modulus. (Adapted from Erben et al. 2020)

2.5 Microfluidics

Assembled adapters containing TPS printed protein microscaffolds were coupled via MicroTight adapters to a pressure-based flow control and pressure source (FlowEZ and FLGP+, both Fluigent). 1/32-inch tubing (IDEX Health & Science LLC) was used to connect the adapters to 360 µm OD HPLC capillary tubing (PolyMicro). The pressure was set to 345 mbar for microfluidic experiments.

2.6 Algorithmic Design

All computationally derived vascularized alveoli print templates were derived by using Hyperganic Core 2.0 (2021, Hyperganic Group GmbH). All demonstrated designs are available as STL files from the University of Stuttgart DaRUS data repository (https://doi.org/10.18419/darus-2612).

2.7 Actin Filament Orientation Maps

Confocal images of microscaffolds colonized with C2C12 cells and stained for the actin filaments were used to calculate actin filament orientation maps using a custom MATLAB script (Mathworks) established in previous studies on single cells[177],[185],[186]. Recorded images were convoluted with elongated Laplace of Gaussian (eLoG) kernels, which were obtained by convolving a Laplacian filter [0,−1,0; −1,+4,−1; 0,−1,0] and n = 15 differently rotated anisotropic Gaussians (σ_x = 3, σ_y = 1). The maximum response images were determined for each pixel, as

$$I_{max}(n,x,y) = \max[eLOG\ (n) x\ I(x,y)]$$

Subsequently, the Otsu's thresholding method was applied, processing I_{max} by the binarized original images[187]. All fibers of the same rotational direction with less than 7 pixels were removed. A color scheme that corresponds to the local actin orientation angles θ_n was applied to the processed images. From each actin filament orientation map the nematic order parameter was derived, as

$$< S > = < \cos 2\ (\theta_n - \theta_0\ ) >$$

with θ_0 as the reference angle, which was chosen to be 90 degrees[1].

2.8 Statistical Analysis

TPS printed scaffolds derived from native alveolar tissue scans were printed in dip-in mode and seeded with phLFs (n = 25). For AFM measurements, 98 to 1002 independent measurements were obtained from one to two samples per parameter set with an indentation depth in the range of 2 µm. Only measurements with a coefficient of determination (R^2) above 0.9 were included. Actin Filament Orientation Maps were analyzed on one sample per design. Proteinaceous channels were printed on custom adapters and perfused using PBS (n = 3) or cell suspension (n = 2). Scaffolds to determine channel resolution were printed using TPS (n = 3) and imaged using two-photon microscopy. Computational alveoli templates were designed using Hyperganic Core 2.0 and were printed using acrylate-based IP-S resin (n = 3) or proteinaceous GM10-based resin (n = 5)[1].

3 Results and Discussion

In this chapter, the experimental results as well as data analysis are presented. Passages and images are adapted from previously published publications (Erben et al. 2020[1], Erben et al. 2022[10]).

3.1 Dip-In TPS for Large Scale Precision 3D-Bioprinted Scaffolds

To produce microscaffolds mimicking native tissue in geometry, confocal microscopy data was used to create a 3D printing model. As a proof-of-principle, a 300 x 300 x 300 µm^3 confocal image stack of the decellularized alveolar tissue of the mouse lung parenchyma was used[1],[24]. The digitized 3D confocal microscopy data, available in VRML2 file format, was converted and exported to the standard printing format .STL using open-source MeshLab processing software[188].

In conventional bottom-up TPS configuration, the laser is focused through an inert immersion oil initiating the photo-polymerization at the distal substrate interface. The highest achievable structure height using protein-based resin was on the order of 14 µm (Figure 7, A). This was less than the working distance of the utilized objective lens (approximately 200 µm from the surface of the glass substrate), suggesting major scattering losses throughout the respective interfaces as well as throughout the already polymerized resin layers. In order to increase the achievable print height, the print set-up was modified to the dip-in set-up (Figure 7, B). In the dip-in mode, the photo-resin simultaneously acts as an immersion medium[189], as the laser is focused through the resin onto the adjacent substrate interface. However, using this setup, the resin cannot be easily encased. This results in continuous solvent evaporation of water-based hydrogel resin, thus limiting feasible printing times to under 10 minutes. In order to guarantee optimal printing conditions and scaffold integrity, it is essential to inhibit evaporation losses during printing, since already a slight difference in resin composition can significantly modify the polymerization dynamics. While evaporation can be easily avoided by using a PDMS cap or a microfluidic device in the bottom-up printing mode, the top-down mode requires an alternative approach[152]: A flexible water seal encasing a 35 mm petri dish with embedded glass substrate was developed. The design allows the objective to adjust the working distance while retaining humidified air around the resin droplet during printing. As a result,

large prints without quality impairment were successfully achieved (Figure 7, B). Using this setup, a 222 x 222 x 104 μm^3 scaffold was fabricated within 37 minutes of printing time. Therefore, 15 µl of protein-based resin was directly applied to a 40x objective (NA = 1.2). This developed dip-in configuration has been used in all subsequent experiments. To cut printing time further, the 40x objective lens was exchanged with a 25x water-immersion objective (NA = 0.8). This allowed for a reduction of the slicing distance from 0.3 µm to 1 µm and the x/y spacing between voxels from 0.2 µm to 0.5 µm. This in return resulted in the reduction of printing time for the 222 x 222 x 104 μm^3 alveolar slice to 6 minutes (Table 1). Using this configuration, a 1110 x 1110 x 104 μm^3 patch was successfully printed, by printing an array of 222 x 222 x 104 μm^3 alveolar slices (Figure 7, B). Achievable print speed and quality heavily depend on resin composition, objective, scan speed and laser power. Table 1 reveals calculated print speeds for a 63x objective and 25x objective for print volumes of 0.00513 mm^3 and 1.0 mm^3. All print times were calculated by Nanoscribe's slicer Describe. In solid mode, the polymerization reaction is initiated by the laser within the entire volume. Using a 63x objective, print speeds range from 1:47:00 h for the 0.00513 mm^3 volume at 70 mms^{-1} to 4:35:30 h for a 1.0 mm^3 volume in solid slicing mode, indicating longer print times for larger volumes. For the 25x

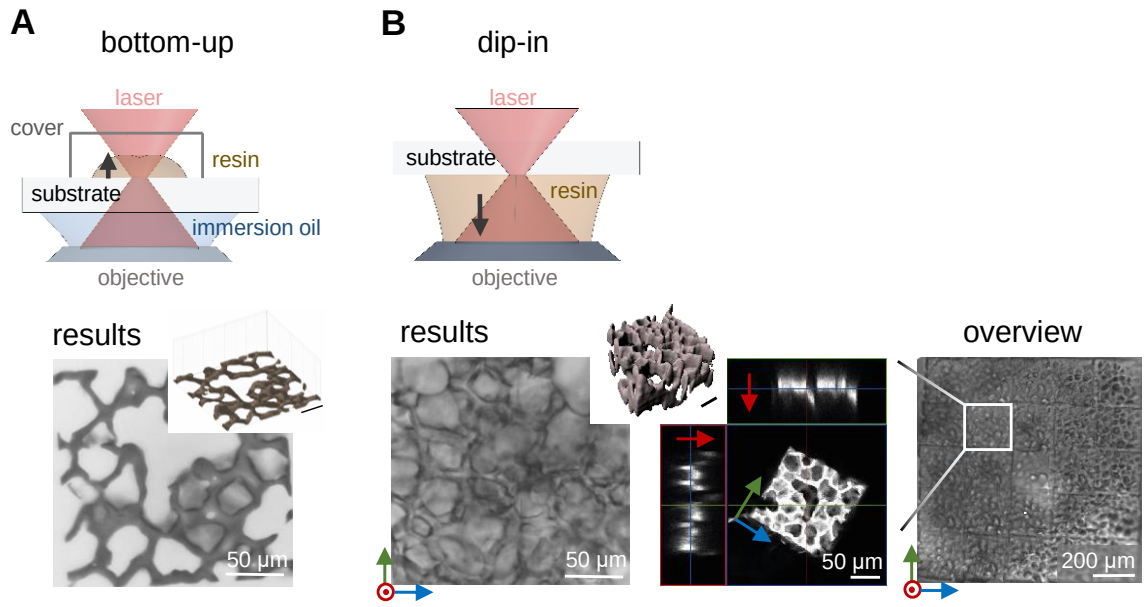

Figure 7: Two-photon stereolithography (TPS) bottom-up and dip-in setup for proteinaceous resins. (**A**) The printing of proteinaceous resins with TPS is predominantly done in bottom up mode to facilitate encapsulation of water-based resin to prevent impaired print quality due to solvent evaporation. In bottom-up mode, the laser is focused through a drop of immersion oil onto the far surface of the glass substrate where the polymerization of voxels is then initiated in a layer-by-layer fashion. However, this working distance of the objective limits the height of the printed structures in this setup. (**B**) In dip-in mode, the resin simultaneously acts as immersion fluid. The laser is focused onto the substrate surface facing the objective enabling a constant adjustment of the working distance. To reduce the solvent evaporation rate, a dedicated objective seal was developed to allow for long-term dip-in mode printing. Printed scaffolds in the range of mm were achieved within 35 mm glass bottom petri dishes. (Image adjusted from Erben et al. 2020)

objective, calculated print times are reduced significantly: 0:06:01 h for a 0.00513 mm^3 volume and 19:33:00 h for a 1 mm^3 volume at 70 mm/s print speed. By reducing print speeds from 70 mm/s to 35 mm/s, print times are increased respectively. In shell mode, lattices are printed within the interior of the structure, while the wall thickness of the surrounding can be adjusted. Here, the wall thickness was selected large enough to avoid internal lattices. The difference in print time from solid to shell result from differing laser paths.

The combination of the dip-in method and the humidified objective seal allowed for 3D printed scaffolds larger than a millimeter in size while maintaining single micron resolution. This printing mode was adjusted in a way to be in consistency to standard life science workflows enabling the direct printing within 35 mm glass bottom petri dishes[1].

volume [mm^3]	scan speed [mm s^{-1}]	63x - solid	25x - solid	25x - shell
0.00513	35	2:14:00 h	0:06:31 h	0:06:02 h
0.00513	70	1:47:00 h	0:06:01 h	0:05:14 h
1.0	35	347:45:00 h	21:11:00 h	19:36:00 h
1.0	70	435:30:00 h	19:33:00 h	17:00:00 h

Table 1: Calculated printing times of alveolar print templates for volumes of 0.00513 mm^3 and 1 mm^3 with laser scan speeds of 35 mm s^{-1} and 70 mm s^{-1}. Calculations by Describe slicer software (Nanoscribe GmbH) with 0.3 µm z-slicing and 0.2 µm x/y-hatching parameters for a 63x objective or 1 µm z-slicing and 0.5 µm x/y-hatching for a 25x objective. Using the solid setting, the entire inner volume of the structure is scanned by the laser, resulting in a solid part. In the shell setting, the interior of the structure is filled with a lattice, while the wall is fully printed. For these calculations, the wall thickness in the shell mode were set to entail the entire volume of the alveolar structure – therefore no interior latticing. (Table from Erben et al. 2020)

3.2 Optimized Biopolymer Resin for Non-Fluorescent, Biocompatible 3D Scaffolds

The optimal resin composition for TPS applications resembles the native ECM in chemical and mechanical factors as closely as possible while minimizing undesirable auto-fluorescence from the residual photo-initiator. Here, the usability of both bovine serum albumin – rose bengal (BSA-RB) and substituted gelatin methacryloyl - lithium-phenyl-2,4,6-trimethylbenzoylphosphinat (GM10-LAP) resins were tested in respect to cell adherence and auto-fluorescence. A scaffold containing of a mesh structure with 5 µm holes, spanned across posts was designed using CAD software Solid Works (Figure 8, A). TPS printed scaffolds fabricated with BSA-RB resin and a 25x objective (Figure 8, B, C, D, green) were subsequently colonized with human mesenchymal stem cells (hMSCs).

BSA-RB is an easy-to-use resin for TPS applications generating biocompatible scaffolds with high resolution[190]. However, BSA is not native to the ECM. To promote cellular colonization of BSA-RB scaffolds, these were previously coated with the ECM glycoprotein fibronectin, which offers molecular attachment sites for cells most likely provided by integrin receptors[191]. Following an incubation time of 2.5 days, hMSCs were fixed and stained for their actin cytoskeleton using phalloidin (red). Confocal images in top, bottom and side view revealed hMSCs on both top and bottom of the scaffold's mesh structure, as well as on the glass substrate. Cells located on the bottom of the mesh suggest active cell migration through the 5 µm holes, consistent with previous reports using e.g. foreskin fibroblasts[192].

To further assimilate the biochemical resemblance of the scaffold composition to the native ECM, commercially available gelatin methacryloyl (GelMa) has previously been used for TPS. GelMa benefits from adhesion promoting properties including arginine-glycine-

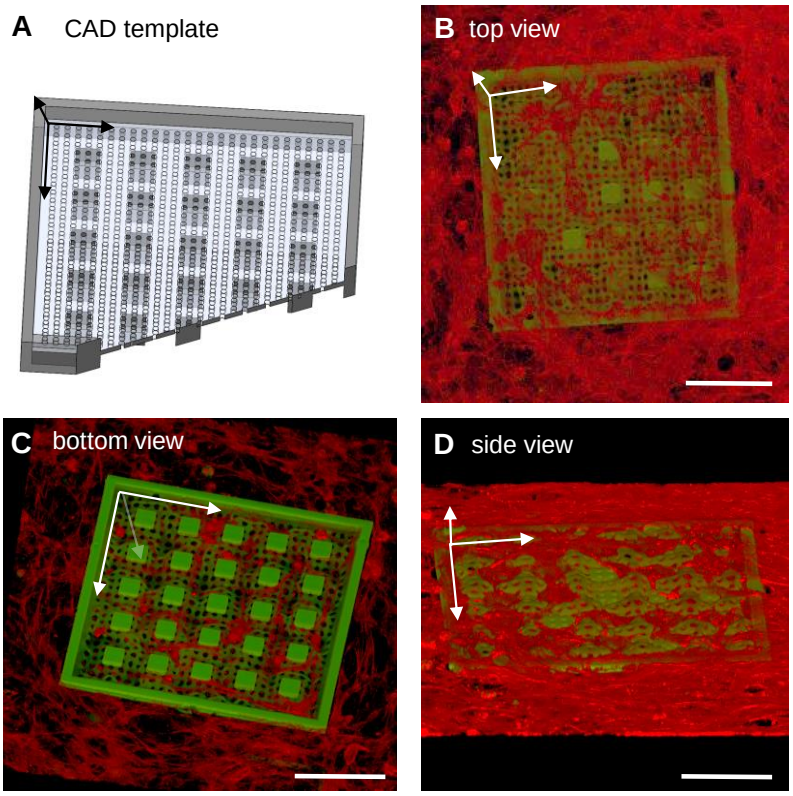

Figure 8: BSA-RB microscaffolds and hMSC colonization thereof. (**A**) A square shaped mesh structure containing circular holes, 5 µm in diameter, supported by posts was designed using CAD software. This design was printed in dip-in mode using BSA-RB resin (green) and colonized with hMSCs. Actin cytoskeletons of hMSCs were stained using phalloidin dye (red) and the cells were imaged in top (**B**), bottom (**C**) and side view (**C**). A cartesian coordinate systems (white arrows) indicates scaffold orientation. Confocal microscopy images show hMSCs on both top and bottom surfaces of the scaffold. (Adapted from Erben et al. 2020)

aspartic acid[159],[193],[194]. Here, GelMa-RB resin containing 25 wt% commercially available GelMa and rose bengal was mixed in the ratio 9:1. As GelMa is in a gelled state at room temperature, this resin composition is only feasible for bottom-up TPS printing mode. To allow for dip-in mode, a layer (200 – 300 µm) of GelMa-RB, thinner than the working distance of the objective was deposited on glass substrates. A diluted photo-initiator pre-mix served as immersion fluid. Resulting scaffolds were colonized with primary human lung fibroblasts (phLFs). Figure 9, A and B show phLFs adhesion to these scaffolds. However, printing time using this approach was limited, as the aqueous immersion medium constantly diluted the pre-applied GelMa layer during the printing process. Alternatively, the BSA pre-mix solution was supplemented with 25 wt% GelMa pre-mix solution in the ratio 4:1 before adding RB. This resulted in the highest possible GelMa concentration for processing at room temperature equating in final concentrations of 26 wt% BSA and 4.5 wt% GelMa. phLFs adhered to the scaffolds printed with BSA-GelMa-RB resin composition in first colonization experiments[1], despite the limited quantity of cell-adherent and matrix metalloproteinase-responsive peptide motifs[193].

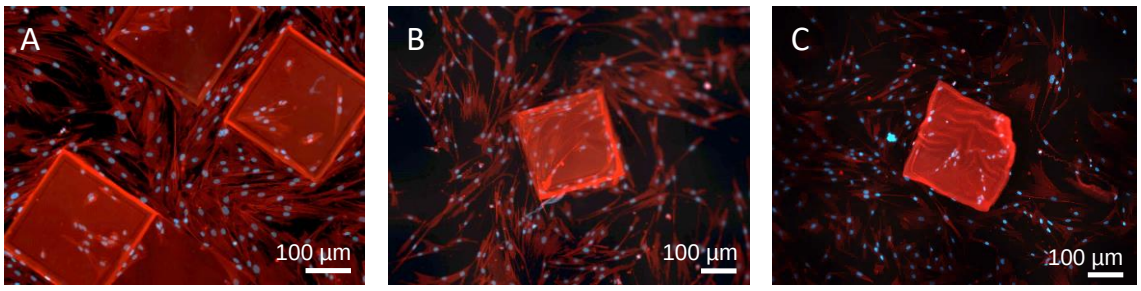

Figure 9: GelMa-RB and BSA&GelMa-RB scaffolds seeded with phLFs. High-precision scaffolds fabricated using TPS with (**A, B**) GelMa-RB resin or (**C**) BSA&GelMa-RB resin. All scaffolds were colonized with phLFs and stained for their actin cytoskeleton using phalloidin (red) and for their cell nuclei using DAPI (blue). Images were taken 48 h after cell seeding using confocal microscopy. (Adapted from Erben et al. 2020)

To increase the volume of gelatin-based high-precision cell scaffolds, the highly substituted gelatin methacryloyl (GM10)[195],[196] was explored. GM10 is a gelatin derivative modified to be liquid at room temperature[197] and is thus beneficial for high-precision 3D bioprinting techniques such as ink jet and TPS[195],[196]. Using a resin composed from GM10 and RB, increased complexity of scaffold geometry was achievable. Exemplary, a double-layered mesh including 2.5 µm holes at the bottom and 5 µm holes at the top was designed in the CAD software Solidworks, including posts arranged in a hexagon layout (Figure 10, A, insert). Similar to BSA-RB scaffolds, these scaffolds were also coated with fibronectin post printing. After 2.5 days of incubation, seeded hMSCs were fixed and stained for their their actin cytoskeleton using phalloidin (red) and cell nuclei using DAPI (blue). Fixed scaffolds were imaged using confocal microscopy revealing hMSC colonization throughout the

scaffold (white arrows in Figure 10, A). Using confocal microscopy, it was observed that phLFs populated GM10-RB scaffolds coated with fibronectin (Figure 10, B) more efficiently than uncoated scaffolds (Figure 10, C). Consistent with previous publications, coating with[59] or integrated printing of ECM[152] proteins is crucial for effective colonization of cells within bioprinted 3D microscaffolds.

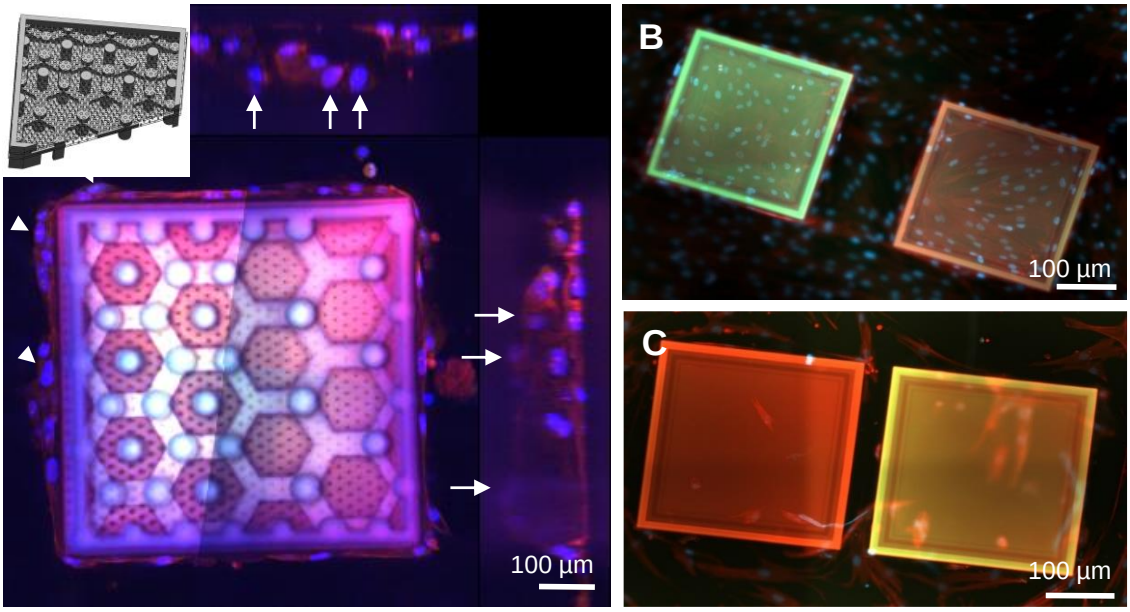

Figure 10: GM10-RB scaffolds seeded with hMSCs. Increased design complexity was introduced by adding a second mesh layer visualized by a CAD rendering (**A,** insert). Hole sizes were 2.5 µm (bottom mesh) and 5 µm (top mesh). (**B**) The design was 3D printed with GM10-RB (pink) resin, colonized with hMSCs and imaged using confocal microscopy. (**C**) On GM10-RB scaffolds previously coated with fibronectin, an increased cell attachment of phLFs was detected compared to uncoated scaffolds. (Adapted from Erben et al. 2020)

Imaging quality of seeded cell scaffolds is crucial for optical cell analysis. All scaffolds printed with proteiaceous resin formulation containing rose bengal as a photo-initiator maintained a strong auto-fluorescence after sample development, which interfered with subsequent fluorescence microscopy of attached cells. Therefore, LAP was explored as a photo-initiator for GM10 printing to substitute or eliminate rose bengal. As high cross-linking efficiency of the photo-resin is necessary for up-scaling of the entire workflow as well as further reduction of the print durations, high concentrations of both protein and photo-initiator are advantageous. Using a resin formulation entailing a final concentration of 25 wt% GM10 and 68 mM LAP, accurate and stable scaffolds for scan speeds from 5 up to 95 mm s^{-1} were achieved (Figure 11)[59],[192]. Here, rectangular scaffolds were printed using a 25x objective and GM10-LAP resin composition printed at 60 mW laser power and varying scan speeds. The scaffolds were imaged during printing using Nanoscribe's built-in microscope[1].

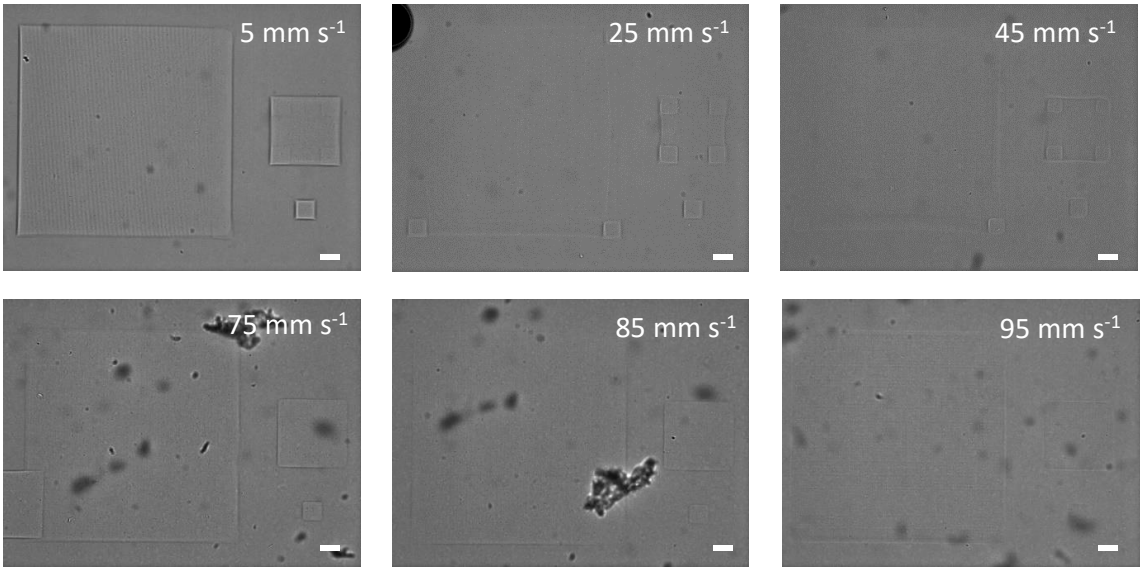

Figure 11: **Print results using GM10-LAP resin composition** printed with 60 mW laser power and scan speeds ranging from 5 – 95 mm s^{-1}. Images derived by the built in microscope of the Nanoscribe GT2 (Nanoscribe GmbH). Scale bars 10 µm (Image from Erben et al. 2020)

Next, the biocompatibility of various different cell types including hMSCs, mouse tendon stem/progenitor cells (mTSPCs), murine NIH3T3 fibroblast wildtype cells (NIH3T3) and human umbilical vein endothelial cells (HUVECs) on fibronectin-coated GM10-LAP was investigated (Figure 12). 280 x 280 x 15 μm^3 scaffolds with 35 µm high frames and various imprinted geometries were seeded with respective cell lines and imaged using epifluorescence microscopy four hours after cell seeding. hMSCs were observed to efficiently adhere to scaffolds containing compartments 100, 75 and 45 µm in width. In contrast, mTSPCs were colonized on rectangular, free hanging geometries, supported by posts at each corner showing only individual adhering cells. NIH3T3 WT cells efficiently colonized both scaffolds with wave patterns (top: 20 µm wavelength, bottom: 10 µm wavelength) as well as scaffolds with 100, 75 and 45 µm compartments. Lastly, the observed morphology of HUVECs indicated their successful spreading throughout the high-precision 3D-printed scaffolds. HUVECs were cultivated on scaffolds containing hexagon towers of -2 – 10 µm height and 50 µm in corner-to-corner diameter[1].

In conclusion, these experiments demonstrate the successful printing of high precision 3D-printed scaffolds with resins tuned for biopinting applications. Scaffolds can easily be adjusted in geometry and can successfully be colonized with various cell types indicating the biocompatibility of the developed GM10-LAP formulation. The prominent benefit of using LAP as a photo-initiator is its optical transparency and low auto-fluorescence in the

visible spectrum (Figure 12), which is crucial for imaging and subsequent analysis of fluorescently labeled cells[1].

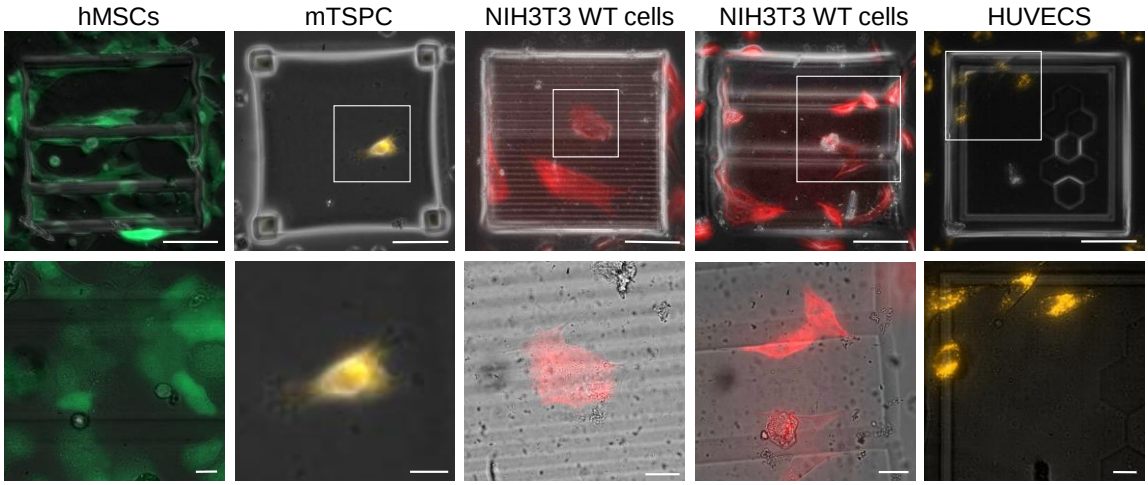

Figure 12: GM10-LAP scaffolds and colonization thereof. Various cell types colonized on different scaffold geometries. All displayed cell types - hMSCs, mTSPCs, NIH3T3 WT cells and HUVECs - adhered to GM10-LAP scaffolds indicating biocompatibility and demonstrating low auto-fluorescence of printed scaffolds. Scale bars top row: 100 µm, bottom row: 25 µm. (Adapted from Erben et al. 2020)

3.3 Mechanical Characterization of Proteinaceous Microscaffolds

Indentation-type atomic force microscopy (IT-AFM) is a common method to evaluate the mechanical properties of native[198],[199] and artificial samples[200],[201]. By indenting TPS printed proteinacous scaffolds using an AFM tip[163],[202], the Young's Modulus (*YM)* can be specified as has been previously demonstrated by several groups[163],[202].

Here, two distinct regions of the force-indentation curves with individual curvatures indicated two sections of the material with specific *YM* for GM10-LAP resin printed with a 25x objective (Figure 13, A): A higher *YM* for > 0.5 µm indentation depth was identified for the bulk region with a *YM* of 26 kPa, compared to a softer interface region at < 0.5 µm indentation depth with a *YM* of 3 kPa. The associated distribution of *YM* values of both bulk and interface was derived from 400 measurements within a 20 x 20 μm^2 area and was plotted in a histogram (Figure 13, B). Here, the mean *YM* values (µ) were found to be 20.49 kPa for the bulk and 1.93 kPa for the interface[1]. These results are consistent with

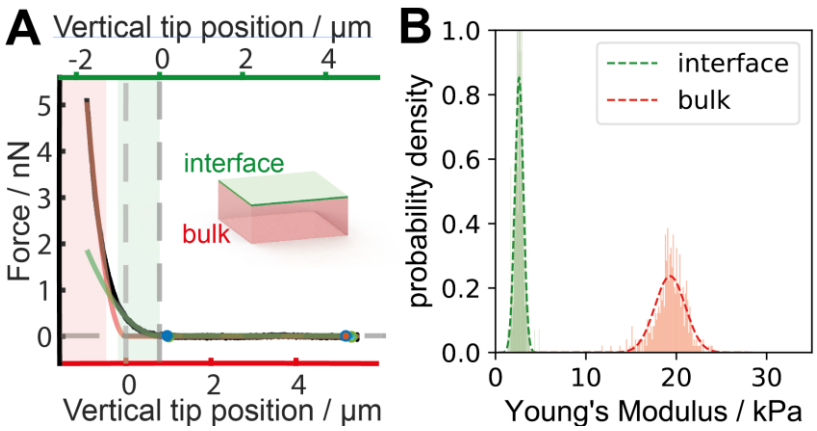

Figure 13: IT-AFM data suggesting distinct interface and bulk regions for TPS printed microscaffolds. (A) High-precision scaffolds printed with TPS and GM10-LAP resin were best characterized combining two fit curves indicating a softer region at the scaffold's interface (last printed layers, green) and a stiffer bulk for 0.5 – 2 µm indentation depths (red). The homogeneous spatial distribution of all sampled Young's Modulus values of both bulk and interface are plotted as histogram. (Adapted from Erben et al. 2020)

the publication of Roether et al., who demonstrated considerably higher local elasticities of cryogelated, proteinaceous scaffolds at the bulk compared to the *YM* at the interface[203].

The influence of various printing parameters on *YM* values of TPS printed scaffolds were evaluated using IT-AFM and were used to draw conclusions on scaffold reproducibility, stability as well as biological conformity with respect to mechanical properties. For this, both BSA-RB (white) and GM10-LAP (grey) resin compositions were evaluated.

For the GM10-LAP composition, scaffolds were printed in dip-in mode with a 25x objective. The mean *YM* values (µ) of the bulk of one scaffold for data sets of 100, 400 and 1600 measurement points amounted to 21.3 kPa, 21.9 kPa and 22.2 kPa with a maximal deviation of 0.9 kPa and a maximal standard deviation (σ) of 2.0 kPa (Figure 14, A). Four different positions measured within a single scaffold resulted in mean *YM* values of the bulk of 21.4 kPa, 21.5 kPa, 20.5 kPa and 21.3 kPa and a maximum standard deviation of 1.2 kPa (Figure 14, A, positions). The stability of the scaffold's bulk *YM* fabricated with BSA-RB resin using bottom-up printing mode with a 63x objective was evaluated over the course of seven days: On the day following printing (day 1) these scaffolds revealed a mean *YM* of 97.9 kPa while *YM* values of samples stored in DMEM cell culture medium at 37°C and 5% CO_2 for seven days (day 7) were measured to be at 103.7 kPa (Figure 14, A, cell culture conditions) - both with a standard deviation of approx. 22 kPa. Contrary, the bulk's *YM* decreased for scaffolds kept in PBS at 4°C from initially 97.9 kPa at day 1 over 65.0 kPa at day 2 to 47.0 kPa at day 7 (Figure 14, A, PBS)[1].

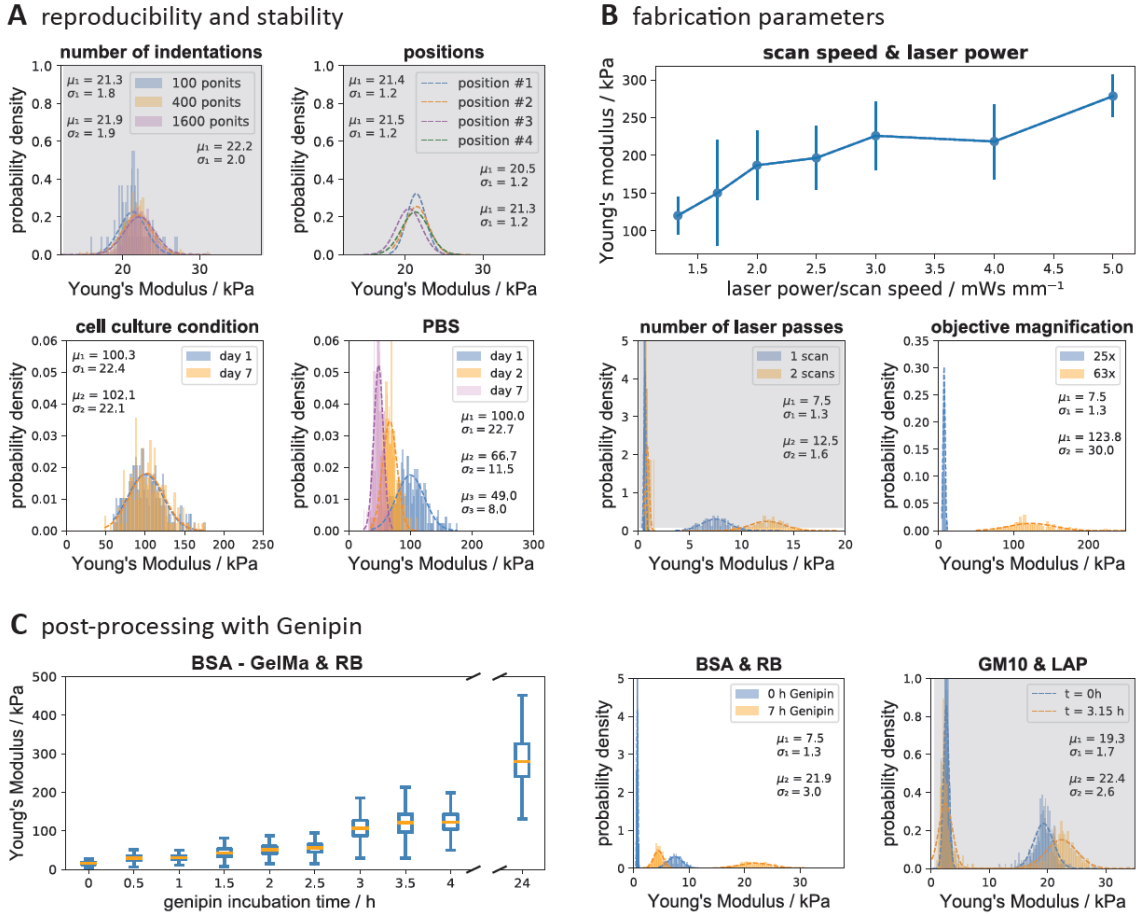

Figure 14: Influence of the fabrication process on the Young's Modulus (*YM*) of TPS printed, proteinaceous scaffolds measured using IT-AFM. Mechanical properties measured on both BSA-RB (white) and GM10-LAP (grey) resin compositions. Respective mean values (μ) and standard deviations (σ) of the *YM* are plotted in histograms. **(A)** IT-AFM evaluation of the *YM* is robust in a range of 100 to 1600 measurements per sample and at various positions within one sample. The temporal stability of proteinaceous scaffolds was evaluated in both storing (PBS, 4°C) and cell culture conditions (DMEM medium, 37°C, 5% CO_2). **(B)** The impact of various fabrication parameters such as laser scan speed, laser power, number of repetitive laser passes and objective magnification on the scaffolds' *YM* are displayed. **(C)** Genipin is shown to be a suitable post-printing, chemical cross linking agent to increase the *YM* of protein scaffolds. The amount of additional cross-links initiated by genipin is dependent on the protein component within the photo-resin. (Images from Erben et al. 2020)

In the following, the impact of the TPS fabrication parameters including scan speed, laser power, number of laser passes as well as objective magnification on the mechanical properties of proteinaceous scaffolds were determined. The *YM* of scaffolds with varying scan speed (SS) and laser power (LP) were investigated. Resulting *YM* values as well as respective standard deviations (error bars) were plotted as a function of deposited laser energy per length (Figure 14, B). As predicted, rising mean *YM* for increasing LP and decreasing SS from 120.4 kPa (σ = 24.3 kPa) at 40 mW LP and 30 mm s^{-1} SS to 278.6 kPa (σ = 69.68 kPa) at 50 mW LP and 10 mm s^{-1} SS were observed. Additionally, multiple laser

exposures of the scaffold geometry throughout printing resulted in an increase of the *YM*. Exposing GM10-LAP scaffold geometries (grey) twice caused an approx. 66.6 % (Δ = 5 kPa) increase of the bulk's *YM* from 7.5 kPa to 12.5 kPa. With 0.9 kPa, the *YM* of the interface region rose by 32.9 % (Δ = 0.22 kPa) and remained softer than the bulk region (Figure 14, B, number of laser passes). Furthermore, the scaffold's *YM* was sensitive to the choice of objective magnification. BSA-RB scaffolds (white) fabricated with a 63x objective in bottom-up mode amounted to a *YM* of 123.8 kPa in comparison to scaffolds printed with a 25x objective in dip-in mode revealing a *YM* of 7.5 kPa. The respective standard deviation decreased 23-fold (Figure 14, B, objective magnification)[1].

In addition to printing parameters, cross-linking agents such as genipin can significantly influence the scaffold's mechanical properties post-printing. The time-dependency of increasing the *YM* as a reaction to the scaffold incubation in 10 mM of the chemical cross-linker genipin was investigated at room temperature (Figure 14, C). Thus, a series of IT-AFM measurements was performed during genipin incubation on scaffolds fabricated with different resin compositions. BSA scaffolds containing 20% GelMa experienced a 270 kPa or almost 20 fold increase in *YM*, increasing from 15.5 kPa (σ = 4.6 kPa) to 288.7 (σ = 75.9 kPa) after 24 hours of incubation. The increase in genipin post-cross-linking for GM10-LAP (gray) and BSA-RB (white) resins was less efficient. The *YM* of the bulk region shifted from 19.3 kPa to 22.4 kPa on GM10-LAP scaffolds after 3.15 hours and from 7.5 kPa to 21.9 kPa on BSA-RB scaffolds after seven hours of genipin incubation[1].

Our IT-AFM results indicate the sufficiency of 100 measuring points for comprehensive *YM* results, as the mean *YM* obtained from 1600 points only deviated by 3% from results derived from 100 measuring points, which was found to be insignificant. For long term cell culture experiments over several days or weeks, it is important to consider deviations of protein-based scaffold mechanics over time. This information can give insights on the aging process of cross-linked hydrogels and can thus indicate either a degradation processes or more likely swelling[1],[203].

In the case of the BSA-RB resin, the mean *YM* was stable for scaffolds incubated in cell culture conditions, in contrary to an observed softening for scaffolds stored in PBS at 4°C. Additionally, the mechanical properties of TPS printed protein-based scaffolds are significantly influenced by the fabrication parameters including scan speed, laser power and objective magnification. For objectives with a higher numerical aperture and magnification of the objective, the voxel size is smaller leading to increased laser intensities as well a an increased number of cross-linking events throughout the polymerizing voxel[1],[204]. It is important to understand, that due to the two-photon absorption phenomena of the photo initiator, the corresponding cross-linking density depends on the laser intensity in a highly non-linear way[1],[205]. Higher cross-linking densities ultimately lead to a denser

and therefore increased rigid polymer network with increased *YM* values. In addition to the fabrication parameters, the scaffold's mechanical properties can also be modified by the addition of cross-linking agents after printing. This time dependent alteration was demonstrated by incubating the scaffolds in genipin[1].

3.4 Actin Fiber Alignment and Cell Colonization on Artificial and *in vivo* Derived 3D-Topographies

Cellular growth and differentiation has been adequately stimulated using 3D printed scaffolds with defined mechanical properties[206]. Similarly, scaffold topography has been used to guide actin filament alignment within single cells[207] and to even enhance tissue maturity[208]. Both stiffness and shape of the ECM have been demonstrated to effect cell behavior, but these aspects have not yet been combined in a single *in vitro* assay. TPS is a powerful manufacturing tool to 3D print scaffolds with high resolution. Being a voxel polymerization technique, it offers extensive design freedom in terms of desired topography and stiffness. Thus, TPS is suitable to produce high-precision 3D scaffolds with tunable *YM* and topographies for cellular applications. The immortalized mouse myoblast cell line (C2C12) is a common model to investigate the biomechanics of single cells[177],[179] and differentiating tissues[209] on scaffolds that emulate the ECM in native properties of myocytes (*YM* ~ 12 kPa)[210]. Actin filament alignment is an indicator for optimal muscle functionality. The regulation and maintenance of muscle mass is facilitated by the differentiation of skeletal muscle into myotubes. In deliberately selected cell culture environments, C2C12 cells have been shown to proliferate, form confluent tissues and differentiate into myotubes *in vitro*[207],[211],[212]. Here, the enhancement of actin filament alignment of C2C12 cells was demonstrated upon protein-based TPS scaffolds which confine the 3D topography in combination with native mechanical matrix properties (stiffness). Actin filament orientation maps (AFOM), color-coding the angles of actin filament alignment, were used to visualize these findings. Figure 15, A, illustrates a typical confluent C2C12 cell layer colonized on a glass substrate lacking tissue-specific topography and *YM* (*YM* glass ~ 50 GPa).

To identify cell orientation, the actin cytoskeleton was stained with Alexa 594 phalloidin (green) and cell nuclei with DAPI (blue). Despite individual cell clusters with aligned actin filaments, cell orientation was observed to be rather homogeneously distributed, indicating a lack of guiding features on the glass substrate (Figure 15, B). To analyze cell behavior on topographically constrained substrates, C2C12 cells were colonized on TPS printed 3D

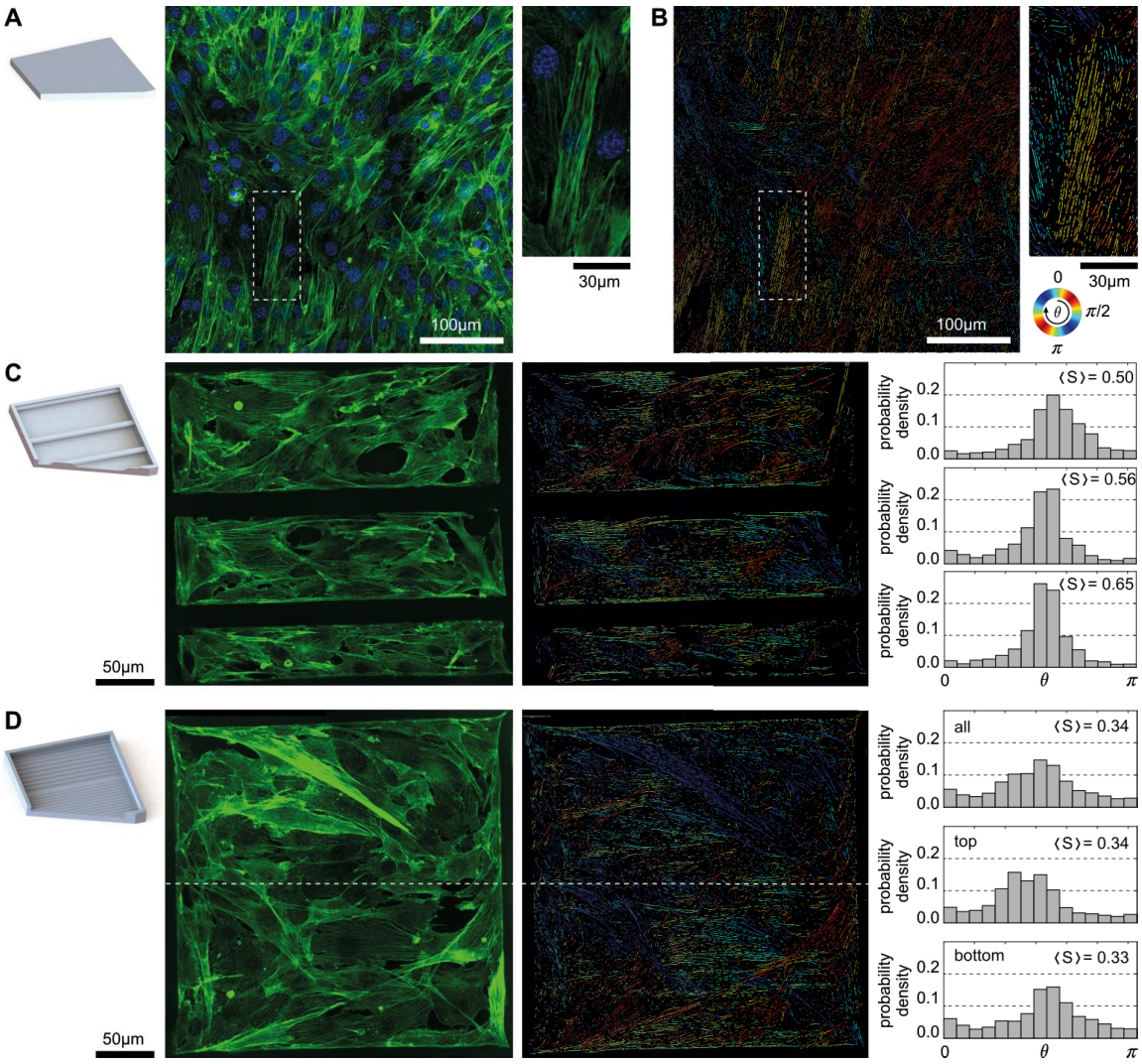

Figure 15: Scaffold topography influences growth phenotypes of mouse muscle cells. (A) Confluent C2C12 cells colonized on a glass substrate lacking spatial confinement with stained actin filaments (green) and nuclei (blue). The right image enlarges a section of the left image (white dashed line) for a detailed view. **(B)** Actin orientation quantification map of cell layer shown in (A). The actin filament orientation angle, θ, is color coded. **(C-D)** Cellular response to spatial confinement in GM10-LAP scaffolds. From left to right: CAD renderings of 3D scaffolds with confined topographies, actin filament (green) stained cell layer (n = 1), actin orientation quantification map, and the respective probability density distributions quantified with the nematic order parameter <S>. **(C)** Cells in scaffold compartments with various widths (top: 100 µm, middle: 75 µm and bottom: 45 µm). **(D)** Cells on scaffolds with two different wave-patterned surfaces (top: coarse wave pattern with 20 µm wavelength; bottom: fine wave pattern with 10 µm wavelength). (Images from Erben et al. 2020)

scaffolds with imprinted compartments or wave patterns. For optimal cell analysis upon scaffolds, these were printed using low auto-fluorescent GM10-LAP resin composition in dip-in mode. The designed scaffolds entailed compartments 100, 75, and 45 µm in width and 300 µm in length. An alternative scaffold design included wave patterns with wavelengths of 10 and 20 µm over the length of 300 µm. The actin filament alignment was quantified using the nematic order parameter <S>, equaling to one for perfect alignment of

all filaments and to zero for homogeneously distributed filament directions. Here, <S> increased with decreasing width of the compartments imprinted on 3D scaffolds (Figure 15, C). While the width of the spatial confinement clearly governed the orientation of the cells' actin filaments, the spatial orientation was further aligned by changing the substrate's topography. For wave-patterned scaffold chambers of 300 x 300 µm^2 an order parameter of <S> = 0.33 was quantified. Hence, wave topographies dictated actin filament alignment, however, no significant difference in <S> was observed between the 10 µm wavelength (top part) and 20 µm wavelength (bottom part). Nevertheless, the cells in the lower part of the scaffold resulted in a narrower distribution of fiber alignment, as shown by the histograms which could result from an enhanced effect of filigree-patterned substrates below the single-cell size of the adherent cells[1].

Primary cell colonization on GM10-LAP, TPS printed, 3D microscaffolds (grey) was demonstrated using a segment of *in vivo* mouse lung parenchymal tissue as print template (Figure 16). After coating scaffolds with fibronectin, phLFs were colonized on scaffolds for 96 hours and fixated prior to staining with phalloidin (red) and DAPI (white). The printed scaffolds spanning 888 x 888 x 104 µm (4 x 4 prints, each with 222 x 222 x 222 µm, n = 3) were imaged using confocal 3D fluorescence microscopy and are displayed as orthoview (Figure 16, A) and as 3D rendering (Figure 16, B). Both displaying modes demonstrate a spatial 3D distribution of colonized cells. Remarkably, the displayed flat and round morphologies of pHLFs found in printed alveolar areas (Figure 16, C) were in some cases highly reminiscent of the morphologies of fibroblasts found in recolonized decellularized 3D ex vivo lung tissue scaffolds[24].

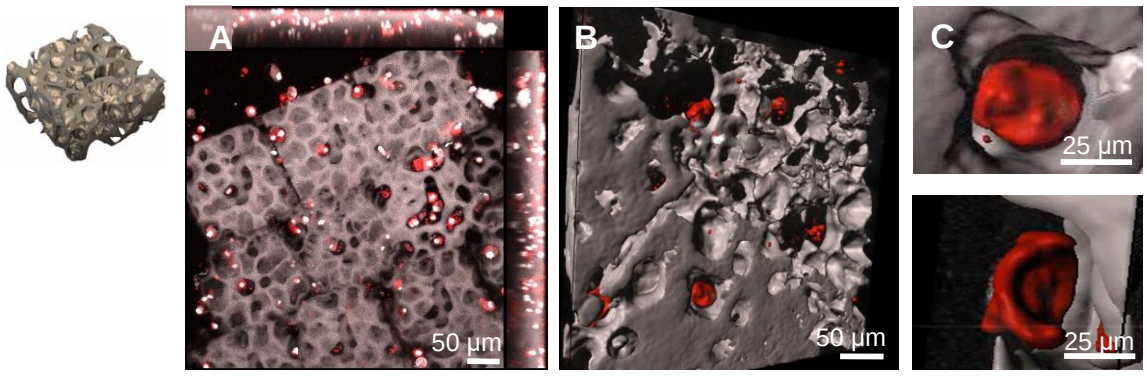

Figure 16: TPS fabricated alveolar scaffolds colonized with primary human lung fibroblasts (phLFs). A replicate of the *in vivo* alveolar tissue geometry printed with TPS using GM10-LAP resin and colonized with phLFs. Cells were stained for the actin cytoskeleton with phalloidin (red) and cell nuclei with DAPI (white) after three days of incubation. **(A)** A stitched orthoview containing a 4 x 4 array of 222 x 222 x 104 µm alveolar scaffolds, demonstrating a 3D distribution of cells throughout the fabricated alveolar microstructure (n = 3). **(B)** 3D rendering of a confocal z-stack and **(C)** close up images of pHLF cell morphologies in alveolar regions. (Adapted from Erben et al. 2020)

3.5 Design and Assembly of an Ultracompact 3D Bio-hybrid Chip

To interface and perfuse individual TPS printed scaffolds, an adapter was designed to seamlessly interface with standard microfluidic equipment (Figure 17). Here, it was aimed to perfuse simple channels embedded in hydrogel as a precursor to enable perfusion of biomimetic micro tissues. For first experiments, a 400 x 215 x 160 µm rectangular geometry containing an 80 µm diameter, curved channel with a minimal wall thickness of 67.5 µm was printed using GM10 directly onto an adapter. Both the GM10 channel and the adapter were 3D printed via TPS using a 25x (0.8 NA) objective. The adapter was printed using IP-S, a commercially available acrylate based TPS resin. The distance between in- and outlet at the interface of adapter and scaffold amounted to 70 µm. The adapter's channel sockets measured 100 µm in diameter to enhance sealing with the hydrogel caps and 368 µm in diameter to match 360 µm outer diameter glass capillary tubing[213]. The glass

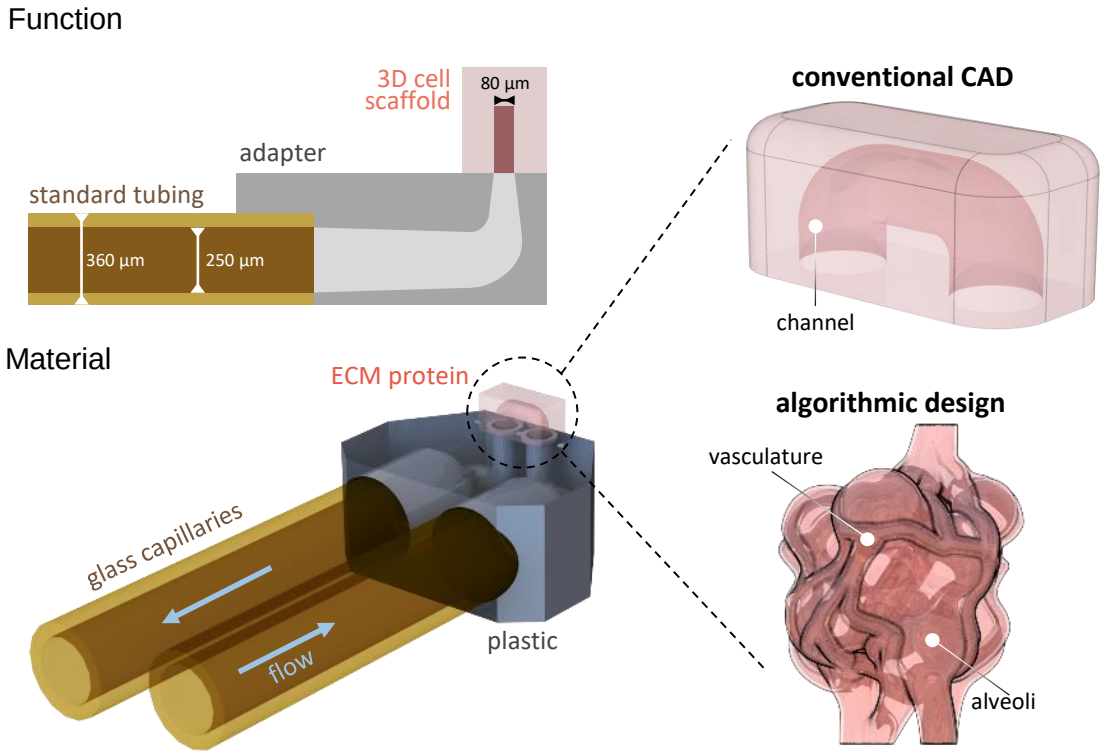

Figure 17: Bio-hybrid perfusion chip concept. The bio-hybrid perfusion chip is designed to bridge scales from microscopic TPS printed protein scaffolds to standard microfluidics. An acrylate-based adapter connects the delicate hydrogel channels within proteinaceous 3D printed cell scaffolds (~80 µm in diameter) with glass micro capillaries (inner and outer diameters of 250 and 360 µm). The two glass capillaries enable in- and outwards flow through both adapter and hydrogel scaffold. The channel diameter is reduced within the adapter to seamlessly interface with the scaffold's channel openings. Perfusable scaffolds can be designed using conventional CAD for simple channel geometries or algorithmic engineering to achieve biomimetic designs mimicking e.g. the alveoli. (Adapted from Erben et al. 2022)

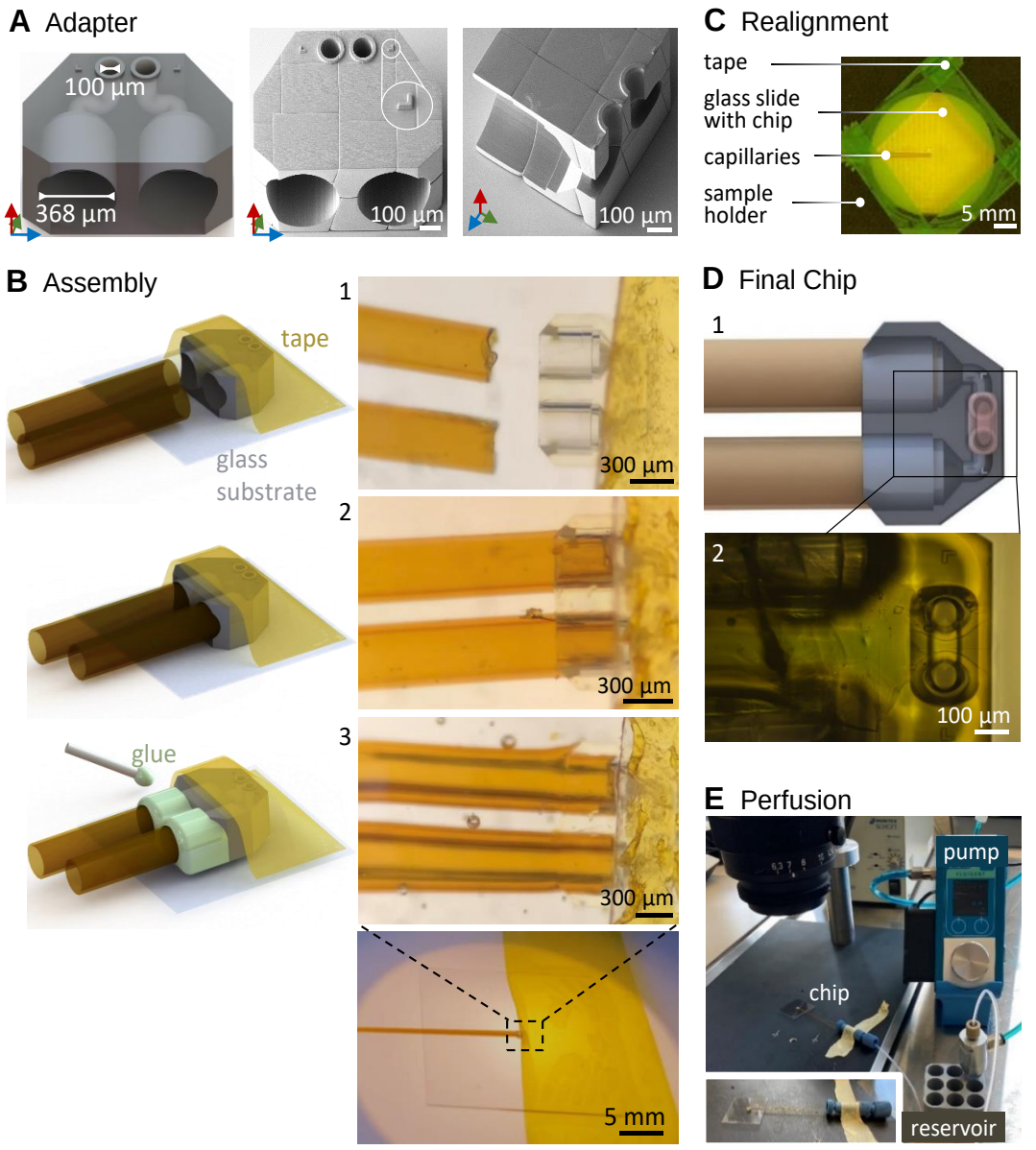

Figure 18: Bio-hybrid perfusion chip assembly: (A) The adapter connects to hydrogel channels via 100 µm diameter channel ports. Two 368 µm diameter ports (left) each accept a standard 360 µm outer diameter HPLC capillary. Entirely (middle) and partially (right) completed adapters fabricated from IP-S resin demonstrate characteristic manufacturing stitching lines on scanning electron microscopy images **(B)** Post-development, adapters were secured to glass substrates using polyimide adhesive tape (1) to insert capillaries with the help of a stereomicroscope (2) prior to fixation with dropwise glueing using epoxy (3). After curing, the adhesive tape was removed (4) (scale bars 1-4: 300 µm) **(C)** Glass substrates with assembled chips including capillaries were centered and secured within the sample holder using adhesive tape. **(D)** Subsequent TPS fabrication of channels embedded in GM10 resin upon a fully assembled adapter (1. top view schematic: capillaries (brown), adapter (grey) and GM10 scaffold (pink); 2. top view; 3. side view of chip and GM10 scaffold (pink)). **(E)** Connection of bio-hybrid perfusion chips to pressure-driven fluid reservoir using standard connectors. (Adapted from Erben et al. 2022)

capillaries were trimmed to a length of 10 cm. The size of the adapter exceeded the field of view of the objective used for TPS and was therefore printed as a sequence of 300 x 300 x 200 µm sections (Figure 18, A), resulting in a rectangular line pattern on the surface. Scanning electron microscopy was used to visualize the geometry of 3D printed

adapters. The adapter's geometry resulted from the requirement for minimal excess material to decrease printing time. Flat surfaces were designed to reduce lensing artifacts in microscopy imaging of internal channels as well as to enable subsequent dip-in mode printing of protein hydrogel scaffolds on top of the adapter. The adapter's glass capillary ports were positioned in parallel to facilitate handling. L-shaped alignment features enabled concurring orientation of both hydrogel and adapter. IP-S adapters were developed in propylene glycol monomethyl ether acetate (PGMEA) solvent subsequent to printing, before rinsing with isopropanol and air-drying. The adapters were then centered and fixed onto 22 x 22 x 0.17 mm microscope cover glass substrates using polyimide adhesive tape (Figure 18, B). As a next step, a glass capillary was inserted into each adapter port under assistance of a stereomicroscope. The two components of 5 minute epoxy glue were homogenized for one minute, cured for further 30 seconds, before carefully applying the glue onto the interface of capillaries and adapter in a dropwise manner. Assembled adapters were allowed to cure for at least 10 minutes before further handling[213]. Finally, the glass substrates holding the assembled adapters were secured onto the sample holder using adhesive tape (green) and a drop of approx. 25 µL GM10 resin was applied on top of each adapter (Figure 18, C). Subsequently, sample holders were reinserted into the TPS printer. The position of the adapter was calibrated in the printer using the L-shaped alignment marks in order to align positions with the GM10 channel segment[214]. Successfully printed GM10 channels were developed in PBS and were visually examined using a stereomicroscope (Figure 18, D). The finalized bio-hybrid perfusion chip was connected to a pressure-based flow control unit via the glass capillaries using MicroTight (IDEX Health & Science LLC) connectors and tubing for perfusion experiments (Figure 18, E).

3.6 Hydrogel Channel Resolution

Organ homeostasis is maintained by the continuous supply of oxygen and nutrients and the removal of waste products through branching blood vessels. Starting from the heart, smaller and smaller blood vessels branch off, down to capillary sizes of 5 to 30 µm[8],[10],[215]. Here, the lowest achievable channel diameter for TPS printing with GM10-LAP-RB was investigated. To calibrate imaging settings, 70 x 70 x 290 µm blocks enclosing an empty cavity with10 µm wall thickness of polymerized resin were printed in 35 mm glass-bottom petri dishes and stored in PBS to keep them moisturized. All substrates were imaged with a 20x (0.95 NA) objective using two-photon excited fluorescence microscopy to obtain x/z cross sections from the imaged z-stacks. Before imaging, substrates were submerged in 0.5 mg/mL fluorescein isothiocyanate-carboxymethyl-dextran solution (FITC-CM-dextran) with an average molecular weight of 150 kDa and a gyration radius of approximately 8 nm[216]. For imaging, the GM10-LAP recipe was doped with 0.5 mg/ml rose bengal as fluorescent dye which was excited with a two-photon excitation wavelength of 1034 nm, while FITC-CM-dextran was emitted at 780 nm (Figure

19, A). Peak absorption and emission wavelengths were 559 nm and 571 nm for rose bengal and 491 nm and 516 nm for FITC-CM-dextran. The emission filters were, thus, chosen to transmit between 610 - 900 nm for rose bengal and 468 - 552 nm for FITC-CM-dextran. These settings allowed for separate imaging of the fluorophores with minimal crosstalk between the two detection channels. The overlay of both rosebengal and FITC recordings reveals only marginal FITC fluorescence within the closed cavity, verifying that the FITC-CM-dextran solution cannot pass the polymerized protein hydrogel (Figure 19, B)[10].

To evaluate channel print fidelity and resolution, scaffolds containing hollow channels with diameters ranging from 5 to 60 µm were designed in CAD. (Figure 19, C). Printed channels reveal non-spherical, but rather elliptical channels, which may result from the extended point spread function in the z-direction of both TPS and two-photon microscopy, causing a larger polymerization and fluorescence detection volume along the z-axis. Superimposed intensity plots and fluorescence images demonstrate FITC-CM-dextran in all channels from 60 µm to 10 µm. However, the 5 µm channel is hardly visible in the fluorescence images. The diffusion of FITC-CM-dextran into channels down to approx. 10 µm in diameter suggests that channels in this range are suitable for perfusion. Thus, TPS printed, proteinaceous micro channels have a high potential to mimic a wide range of microvessel sizes in microfluidic devices[10]. These observations are consistent with the results of Dobos et al. who prepared thiolated gelatin and gelatin-norbor channels down to 10 µm in diameter with a similar TPS setup[8].

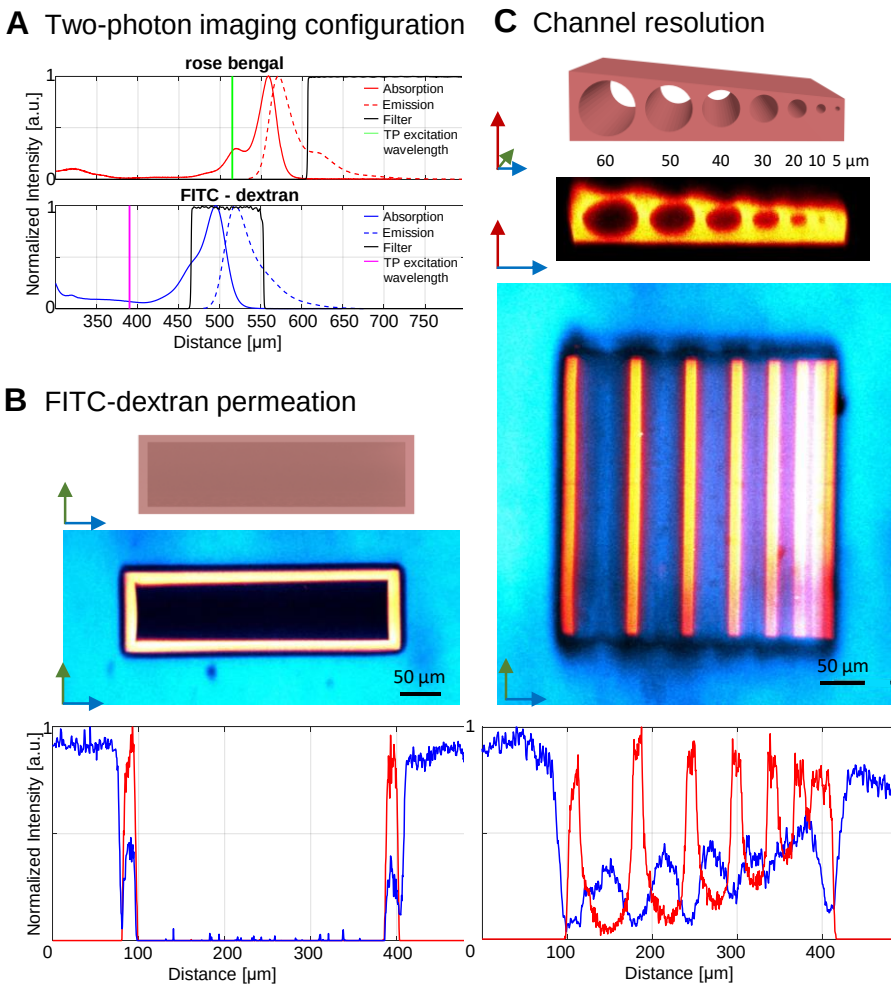

Figure 19: Hydrogel Permeability and Channel Resolution. (A) To determine microchannel diameter resolution in TPS printed GM10 scaffolds, two-photon excitation at 780 nm or 1034 nm for aqueous FITC-CM-dextran (blue) and 0.5 mM rose bengal stained scaffolds (red) was used in combination with matching bandgap emission filters at 468-552 nm and 610-900 nm. Scaffolds were immersed in 0.5 mg/mL FITC-CM-dextran to visualize internal channel sections via confocal sections and corresponding line plots **(B)** FITC-dextran of 150 kDa with a gyration radius in the range of 8 nm, was neither observed to permeate into the hydrogel, nor into internal channels, suggesting that the polymerized GM10 resin mesh size was large enough to enable residual rose bengal to be washed out during scaffold development but small enough to prevent entry of FITC-Dextran. **(C)** A scaffold with channel diameters of 5 to 60 µm and 290 µm in length was printed. The x/z section was derived from imaged z-stacks to compare the printed structure with the designed CAD model. Fluorescence imaging of the central x/y plane (middle) visualizes channel cross-sections. The x/y section of both channels are overlaid and normalized intensities along the cross-section indicate the permeability by FITC-CM-dextran of all channels down to 10 µm. Scale bars 50 µm. (Images from Erben et al. 2022)

3.7 Active Perfusion and Cell Seeding of Hydrogel Channels

In the following, active perfusion of the assembled bio-hybrid chips is evaluated. As a proof-of-concept, a single hydrogel channel with a diameter of 80 µm is perfused by transporting PBS buffer from a reservoir into a the connected chip using 345 mbar pressure (Figure 20). The channel diameter size was chosen to avoid the risk of clogging by cells. Initial air bubbles were successively evacuated from the channel by streaming in PBS buffer until the entire system was bubble-free after a few seconds. The air bubble free system verified a watertight seal between the IP-S contact chip and the protein channel, indicating sufficient adhesion and fit as well as adequate bonding between both materials for the applied pressure gradient.

After demonstrating successful perfusion of hydrogel channels, GFP labelled hMSCs of the SCP1 cell line[217] were introduced to the system. For cell infiltration, the PBS within the reservoir was replaced by cell suspension and the system was once again perfused. Subsequently, the 80 µm hydrogel channel was imaged with bright field and

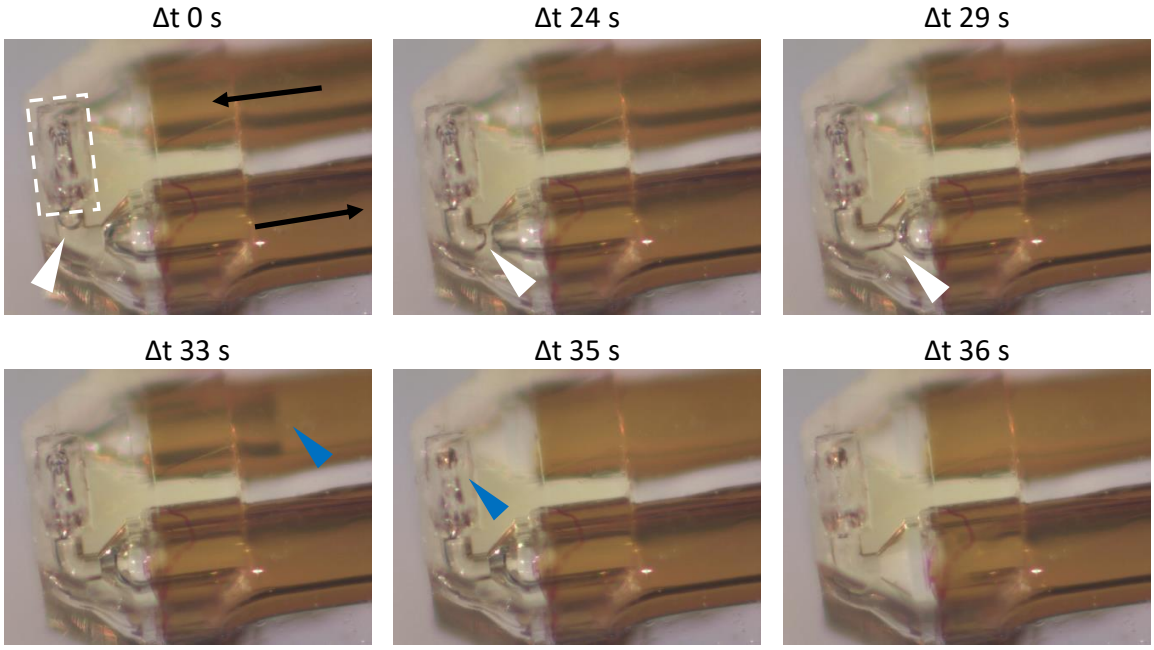

Figure 20: Liquid transport through bio-hybrid perfusion chip. The system is kept humidified by storing it in PBS to prevent drying induced damage to the GM10-LAP channel (white dashed line at t = 0 s). PBS buffer is perfused through the channel (black arrows) by a pressure-based flow control system. Blue arrows indicate the advancing air/PBS buffer meniscus. An air bubble was captured within the channel of the adapter chip (white arrows), but was transported out as soon as a continuous water column (blue arrows) had pushed from the inlet capillary through the entire channel system (t = 33-35 s). The chip was air bubble free after 36 s. (Images from Erben et al. 2022)

epifluorescence microscopy. However, the strong auto fluorescence of the TPS printed,

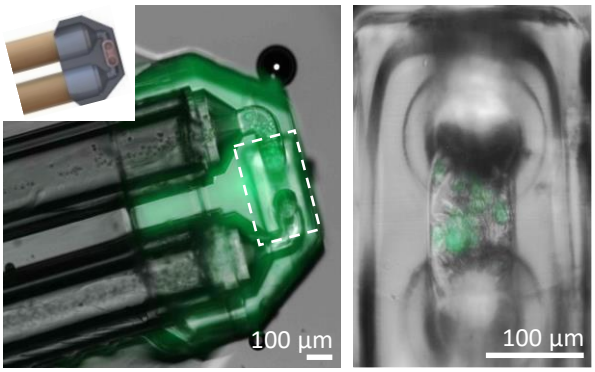

Figure 21: Cell Seeding of bio-hybrid perfusion chip. hMSC cell suspension expressing GFP was flushed into the GM10-LAP channel through the adapter ports (left). The hydrogel block containing a channel is highlighted by a dashed white rectangular box. A close up thereof reveals fluorescent hMSCs (green) within the GM10 channel (right). (Images from Erben et al. 2022)

acrylate based adapter (Figure 21, left) dictated thresholding and background subtraction to resolve individual cells within the GM10 channel (Figure 21, right)[10]. While these experiments demonstrate successful perfusion and cell infiltration of simple channels, further experiments are necessary to study and optimize cellular responses within TPS printed micro channels. Also, the use of lower auto-fluorescent resins seem inevitable to study cellular behavior within these ultra-compact bio-hybrid perfusion chips[218].

3.8 Reusability of Assembled Adapters and Hydrogel Biodegradability

The individual fabrication steps of multi-step assemblies can be quite time consuming. Therefore, recycling of sub-components are desirable. In order to assess the reusability of the adapter chip, the hydrogel block was gently removed from the adapter using a plastic pipette followed by intensive rinsing efforts with double distilled water. The connection between glass capillaries and adapter was left intact. Electron microscopy examination of a stripped adapter showed only minor gelatin remnants on the adapter surface and a protein gel thread spanning one of the adapter ports (Figure 22, A). Basic mechanical cleaning may therefore be sufficient for adapter reuse. Ultrasonic cleaning or washing with sodium hydroxide impaired the integrity of the glass capillary-adapter seal and could therefore not be used to further advance hydrogel removal[10].

In bioprinting, scaffolds are fabricated to provide shape and mechanical strength to cells. However, clinical applications often require defined biodegradability of proteinaceous scaffolds. Ideally, biodegradation is tuned to provide shape and strength, until cells themselves have secreted a sufficient amount of ECM[202]. Here, hMSCs have degraded

GM10-LAP-RB scaffolds over the course of 12 days (Figure 22). While the displayed scaffold appears to be largely intact after 4 days, the cells have removed small chunks from the scaffold by day 12, demonstrating that the cross-linked GM10 can be resorbed by the hMSCs over time[10]. This is in agreement with Van Hoorick et al., demonstrating enzymatic biodegradation of cross-linked gelatin scaffolds[219].

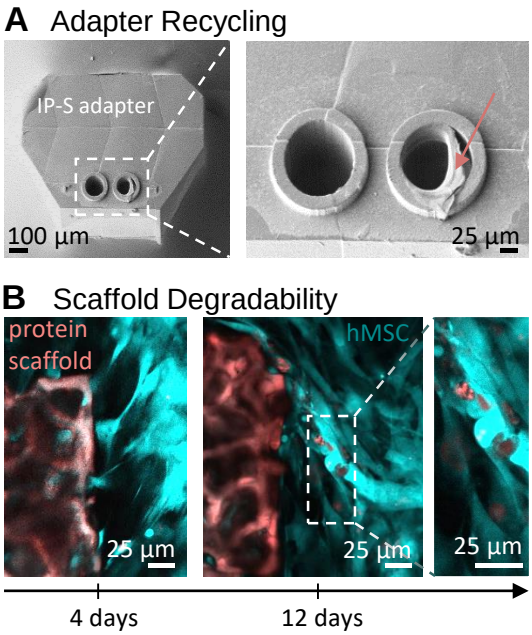

Figure 22: Component Reusability and Scaffolds Biodegradability. (A) Scanning electron microscopy was used to reveal reusability of adapter components after mechanically removing the GM10 block. A magnified image displays a remaining GM10 gel thread spanning one of the two adapter ports (pink arrow). **(B)** Protein scaffolds (red) 4 and 12 days after colonization with human mesenchymal stem cells (hMSC, blue). Cells have gradually begun to degrade the scaffold over the course of 12 days. (Images from Erben et al. 2022)

3.9 Biomimetic Design of Vascularized Alveolar Scaffolds

The alveoli are air filled bubbles spanned by a highly branched capillary system governing the gas exchange within the pulmonary system[42],[220]. The basal membrane spanned with pneumocytes regulates O_2 and CO_2 exchange between red blood cells within the capillaries and the gas phase within the alveoli (Figure 23, A)[53],[221]. Native alveoli dimensions are in the range of 58 µm in mice[222] to approx. 200 µm in humans[60]. The previous approach of using print templates derived from native tissue failed to provide an intact and perfusable

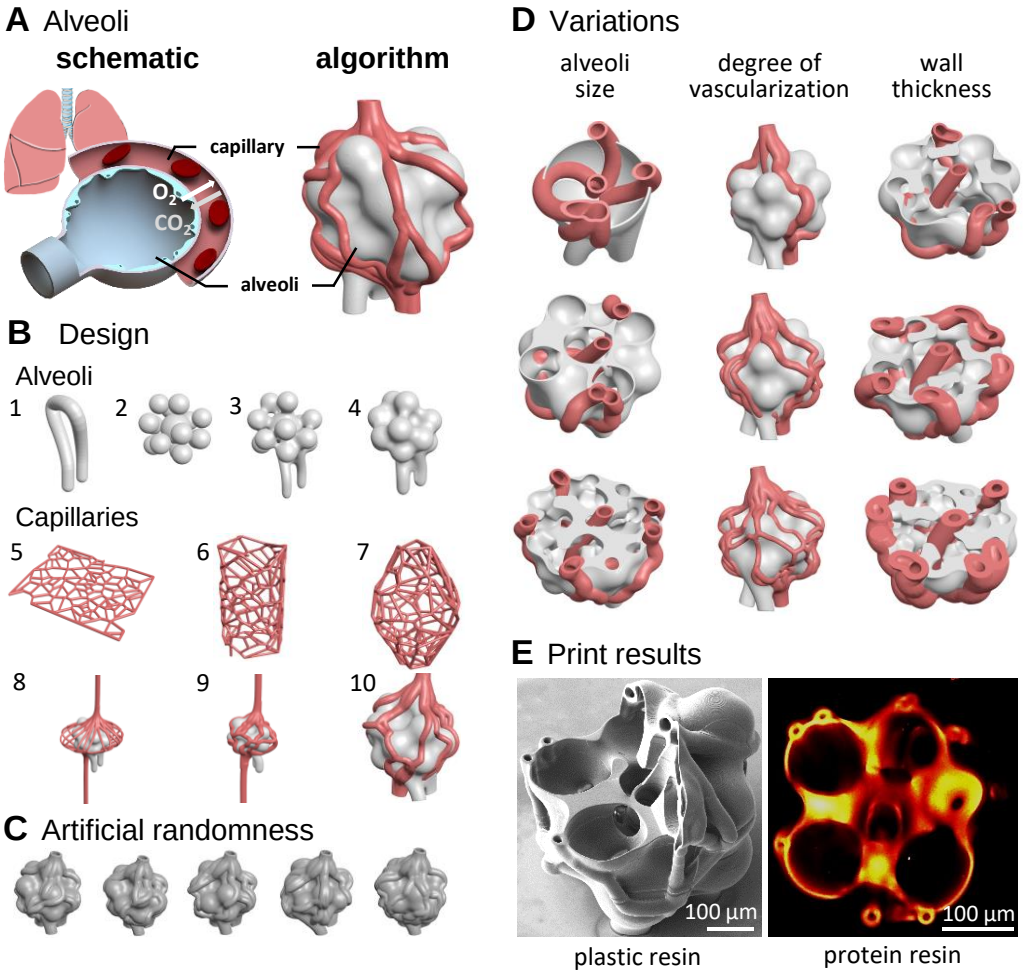

Figure 23: Algorithmic engineering of vascularized alveoli. (A) The alveoli are air filled bubbles at the distal ends of the lung, governing CO_2/O_2 exchange (left). Scaffolds mimicking the native alveoli can be derived by using algorithmic engineering (right) by following these steps: (1) The air path is generated through lattice beams. (2) A spherical foam map of pre-defined min./max. sphere sizes and gaps recapitulates alveolar sacs. (3) Sphere surfaces are connected by computing offsets of each sphere, before combining the air path with the spherical foam map. (4) Subsequently, the surfaces are smoothed. (5) Based on polygonal cells created using random input points on a 2D canvas, (6) a transformation to a 3D cylindrical assembly (7) is followed by describing variable radii, a spine height, variable beam thickness and edge curving. (8) The resulting cylindrical Voronoi mesh is then partially snapped onto the previously designed alveolar base (9) using transition interpolation. (10) Final in- and outlets are cut off. **(C)** All design features such as sphere layout or capillary paths can varied either by artificial randomness or **(D)** by adjusting specific design parameter, such as alveoli size, degree of vascularization and wall thickness. **(E)** Algorithmically engineered alveoli templates were printed true-to-scale using TPS using standard acrylic-based resin (scanning electron microscopy, left) or GM10-LAP-RB resin (two photon fluorescence microscopy, right). (Adapted from Erben et al. 2022)

microvasculature. Furthermore, these templates were not parametric models, in such lacking the ability to be modified according to individual design features such as wall thickness[10]. Towards the goal of experimentally perfusing complex microtissue, algorithmic engineering was used to design an interconnected alveoli model spanned with a vascular network. Alveoli design synthesis (Figure 23, B) was launched by describing an air path using lattice beams[223], followed by the generation of a spherical foam map

mimicking the individuality of the alveoli through variable sphere radii as well as gap dimensions between individual spheres within a bounding geometry. By defining offsets from all spherical surfaces, multiple spheres were combined before connecting them with the initial air path. Thereafter, offset and smoothing functions were executed repeatedly to hollow the geometry, resulting in the final alveolar geometry. Design synthesis of the adjacent capillary network was initiated by defining polygonal cells derived from random input by using a Voronoi algorithm. Subsequently, the 2D canvas was transformed to a 3D cylindrical mesh. Variable radius, beam thickness along the height and curving of edges was implemented. The cylindrical Voronoi mesh was then partially snapped onto the surface of the previously generated alveolar base. Finally, in- and outlets were trimmed to their final lengths. Both alveoli and capillaries are by design contactable through distinct in- and outlets intended for perfusion, cell seeding and tidal ventilation. All designed alveoli in- and outlets are positioned such that they can be interfaced by respective ports of the IP-S adapter chip[10].

In contrast to conventional CAD, algorithmic engineering allows to define every parameter influencing the design to be either fixed, random or to vary within a preset range, enabling artificial randomness at all design stages (Figure 23, C). Here, the total construct size and air path design were maintained, while capillary and sphere locations were randomly located. As a result, different combinations of the design parameters were explored. Additionally, selected design parameters have been deliberately defined to demonstrate systematic design variation in alveoli size, degree of vascularization and wall thickness (Figure 23, D)[10].

A selected variant of the algorithmically engineered alveoli was printed using dip-in mode TPS printing with acrylate-based IP-S resin and imaged using scanning electron microscopy (Figure 23, E, left). A proteincaous version was printed using GM10-LAP-RB resin and imaged using two-photon fluorescence microscopy (Figure 23, E, right). The alveoli model entails features to recapitulate breathing dynamics and controlled medium distribution in accordance with the bioinspired alveolar models from Grigoryan et al.[99]. For that particular study, the authors used a custom built one-photon stereolithography device to print simplified vascularized alveolar model topographies using poly(ethylene glycol) diacrylate. Strikingly, tidal ventilation and oxygenation within channels down to approx. 200 µm were demonstrated. However, these scaffolds were 2 - 10x larger than human alveoli. The designs presented here show higher resolution using TPS printing: For acrylate-based plastic prints, alveoli sizes of approx. 80-170 µm, inner capillary diameters of approx. 15 µm and minimal wall thicknesses of approx. 6 µm were achieved. For GM10 prints respective sizes rendered approx. 50-100 µm, approx. 10 µm and approx. 4 µm. Other studies set out to recreate micro-scale, proteinaceous interfaces including simple membranes[59] or channels[8] using TPS. However, these channels have note been

selectively contacted and all features were rigidly enclosed. The scaffolds realized in this set of experiments render true-to-scale human[60] and mouse[222] alveoli[10]. By exploiting parametric design, complex scaffold templates can easily be customized, adapted to various murine or human lung tissue features or tailored to recapitulate pathological tissue e.g. to study cellular response on fibrotic tissues[41].

4 Conclusion and Future Prospects

Closing remarks are partially adapted from previously published publications (Erben et al. 2020[1], Erben et al. 2022[10]).

Comprehending the development and maintenance of native tissues has been a long going effort by an interdisciplinary community. Technical advancements ranging from high-resolution imaging[17],[224], over proteomics and transcriptomics[32],[225], to computational modelling[33] have substantially increased our understanding of molecular composition and architecture of the ECM[1]. In particular, ECM properties on the micro scale have been shown to be essential in guiding cell growth, migration and differentiation, ultimately governing tissue architecture[1],[24],[43],[169]. Beyond biochemical and biophysical properties, the tissue architecture has a large impact on organotypical tissue functionality[160],[226],[227]. Bioprinting is frequently used to mimic native tissues *in vitro* across all scales. Although bioprinting methods to recapitulate microscopic features in a controlled manner have been developed, creating clinically relevant tissues mimicking their native counterpart in composition, mechanics and geometry and including an interconnected microvasculatory system poses a challenge up to date.

4.1 3D printed cell niches with the highest biological conformity and resolution

The transition from previous methods, such as 2D micro-patterning including elastomere stamps[228],[229], spotted DNA microarrays[230], or polyacrylamide gels[159], to additive manufacturing has enabled the fabrication of more realistic 3D cell and tissue environments *in vitro*[1],[37]. Especially, one-photon stereolithography[99] and volumetric bioprinting[147],[231] allow for the rapid 3D printing of biological tissue constructs in the dimensions of several cm with double digit µm resolution. However, to achieve models of native tissue with higher detail, manufacturing techniques such as TPS with significantly higher resolution are necessary. Yet, the implementation of protein-based TPS printing poses several difficulties: Firstly, in voxel-based additive manufacturing print time and spatial resolution are inversely linked to each other and are limited by 3D voxel size, impeding up-scaling of overall print volumes[1],[147],[232]. As a result, total dimensions of proteinaceous scaffolds with single digit µm resolution are typically < 0.03 mm^3 [58],[164],[165],[172]–[174]. Printing volume and resin quality is further limited by uncontrolled water evaporation of hydrogel photo-resins, which can quickly affect printing

success. Additionally, recapitulating native features on the single digit µm scale renders difficult using proteinaceous resin formulations[1],[161],[192].

Cell scaffolds mimicking native tissue in terms of scaffold geometry, size and composition were improved throughout this study. By transforming a decellularized mouse alveoli tissue data set, imaged using confocal microscopy, to a 3D print template, the replication of the native ECM geometry with highest resolution was enabled. By optimizing ECM derived gelatin methacryloyl photo-resin composition and TPS print setup including the design of an objective seal to prevent uncontrolled evaporation during printing, up to mm-sized 3D scaffolds with micrometer precision, defined mechanical properties and low auto-fluorescence were achieved. Subsequently, cell growth and analysis of various colonized cell types including stem and primary cells on our precision 3D printed scaffolds were observed, both on classic 2.5D, as well as on complex *in vivo* derived 3D topographies[1].

To further enhance printing volumes, an optimization of photo-resin chemistry including photo-initiators[163],[233] and the advancement of TPS technology by implementing multiple laser foci in parallel are recommended[234]. In future, the photo-resin composition can be tweaked towards the native ECM composition, e.g. by including a variety of native proteins, to enhance the biological relevance of these precision printed 3D scaffolds[235]. Moreover, a specific spatial distribution of individual resins could enable spatially defined proteinaceous multi-material printing[158],[192], specifically addressing and guiding individual cell types within co-cultures[1]. By introducing an enclosed environment providing sterile conditions accompanied by humidity and temperature control to the printing process will enable direct cell encapsulation within 3D printed scaffolds during the printing process[1],[8],[165],[169].

4.2 Mechanical Analysis

Micro-scale ECM properties including mechanical cues have been discovered to be decisive in governing and guiding cellular growth, migration, and differentiation, to ultimately define tissue architecture[43],[169]. The wide range of stiffness found *in vivo* such as in the lung (~1 – 2 kPa) or in cartilage (~500 - 1700 kPa)[1],[24],[236] have been emulated by several bioprinting techniques and using various proteinaceous resin compositions[1],[193],[194]. To achieve an equally wide range of mechanical properties on the micro scale using TPS requires a rigorous mechanical analysis of microscaffolds. The Young's modulus (*YM*) of micro- to nanoscale structures has been previously quantified by nanoindentation[237], laser Doppler vibrometry[238],[239], or atomic force microscopy (AFM)[1],[163],[173]. Indentation-type AFM (IT-AFM) is particularly suitable for the

mechanical characterization of biomaterials, as measurements can be conducted in a physiological environment being able to sense pN forces with nanometer spatial resolution[1],[182],[240]–[242].

Several groups have previously published *YM* values of TPS printed hydrogels, including gelatin, silk fibroin and bovine serum albumin, ranging from 2 kPa – 220 MPa. In these studies, photo-initiators such as methylene blue, rose bengal and flavin adenine dinucleotide were used[162],[163],[166],[168],[173],[202],[243].

The detailed analysis of *YM* on precision printed proteinaceous scaffolds using IT-AFM, suggests that listed literature values are not directly comparable with each other, since even the smallest changes not only in the fabrication parameters, but also in the post-processing and storage conditions can have a large impact on the resulting *YM* values. *YM* values of precision printed scaffolds fabricated with BSA-RB or GM10-LAP ranged between 7 – 300 kPa, equivalent to many biological tissues[1]. Further, a stiffer bulk and softer interface region were observed. This may have an effect on cell-scaffold interactions and should be further investigated.[1],[244] By increasing energy per volume and time the cross-linking density within the polymerizing voxel is enhanced in a highly non-linear way due to the two-photon absorption of the photo-initiator, resulting in elevated *YM* values[1],[204],[245]. Increasingly rigid polymer networks due to higher cross-link densities were demonstrated by increasing laser intensities, the number of subsequent laser passes, the objective magnification and respective numerical aperture or by decreasing scan speeds. The *YM* can also be altered chemically post-printing by tailoring cross-linking densities using e.g. genipin[1]. The adjustment of the *YM* during and after TPS fabrication can be used to locally adjust the scaffolds to address specific cellular cues, thereby directing cellular maturation and functions in a highly controlled manner[1],[37]. Also, batch to batch variability of resin components, the storage conditions of scaffolds as well as the time delta between printing and IT-AFM experiments can have a major influence on mechanical properties and should, thus, be taken into account when comparing the mechanical properties of proteinaceous scaffolds[1].

In future, the spatial distribution of mechanical properties should occur automatically by defining them within the print templates. Given the high sensitivity of the *YM* to small changes such as batch to batch variations of resin components, scaffold storage conditions or duration between printing and measurements, scaffolds should be subjected to regular quality control and these parameters must be taken into account when comparing such values. Advanced methods such as Brillouin microscopy are paving the way to non-destructive, label- and contact free optical elastography making such technologies highly suited for mechanobiological analysis[16],[244].

4.3 Perfusion of Precision Printed Scaffolds

Organ-on-a-chip systems that emulate relevant aspects of human tissue physiology have evolved as a powerful technique for investigating intricate biological phenomena[10],[49],[53]. Recently, biomimetic *in vitro* models combining microfluidic perfusion and protein-based cell niches have enabled even more precise control and manipulation of cellular micro environments while ensuring an adequate supply of nutrients for short- and long-term cultivation[10],[246]. Additive manufacturing techniques are highly beneficial for the fabrication of 3D microfluidics due to their general design freedom. However, the feasible 3D printing resolution impedes with the desire to manufacture highly intricate shapes at submicron accuracy[10],[247]. Thus, TPS provides unique performance improvements to microfluidic applications[10],[107],[143],[213],[248]. Previously published work on TPS-fabricated 3D microfluidics fabricated with synthetic materials include in-chip scaffolds to study cell migration[249], microfluidic enzyme reactors[250], filters within microfluidic channels[251],[252] as well as nozzles and mixers for serial crystallography[10],[213],[214].

Inspired by a new generation of more realistic organs-on-a-chips combining rigid microfluidic systems with hydrogel bioprinting, a proof-of-principle ultracompact bio-hybrid perfusion chip allowing to selectively connect double digit micrometer channels embedded in precision printed scaffolds and connected to standard microfluidics was developed. To the best of my knowledge, this was the first study demonstrating the contacting, perfusion and cell seeding of individual channels with double digit µm dimension within TPS printed scaffolds[10]. In future, further reduction of channel diameters to below 10 µm seems desirable in order to recapitulate minute units of native microvasculature[10],[233]. Perhaps higher numerical aperture writing objectives and optimized photo-absorbing resin additives such as tartrazine[99] will further increase achievable microscaffold resolution[10]. Perfusion of reduced channel diameters can be tested by adjusting the dimensions of the connectors on the adapter. To supply a branched microvasculature, the number of channels and/or ports can be increased. Future experiments should also tackle long-term cell cultivation of the hydrogel channels including cell types such as epithelial cells, as well as continuous perfusion and even ventilation[10]. Additionally, lower auto-fluorescent resins for adapter fabrication are desirable for optical cell culture analysis[218]. Besides the fabrication of scaffolds mimicking the alveoli, our microfluidic approach is applicable to all tissues and is especially valuable to mimic the interveined (micro-) vasculature system. Our developed design, which does not encapsulate perfused biological scaffolds within rigid enclosures, may allow for simple upscaling and unrestricted growth of tissue segments in future[1]. In combination with other methods such as laser-induced forward transfer[130], cells can selectively be distributed on our precision 3D printed scaffolds to achieve spatially defined

co-cultures[130]. By combining additive manufacturing methods with different resolutions, e.g. by combining one- and two-photon stereolithography, our synthetic adapters could be replaced by hydrogel adapters, eventually scaling to full organs while maintaining high resolution where necessary. These additional milestones will not only allow for the selective cell seeding and subsequent perfusion of individual channels, but will enable the sufficient supply of nutrients throughout ever larger precision 3D printed scaffolds, facilitating long-term cultivation[99].

4.4 Automated Design

In nature, growth follows sophisticated patterns of branching phenomena which have mathematically been described by biologically inspired algorithms such as Mandelbrot's fractal model, the reaction-diffusion model based on Turing instability[138], or digital morphogenesis applied to architecture[10],[139].

In the field of bioprinting, 3D print templates are commonly manually designed using a CAD software[253]. Due to the complexity of anatomical designs, this is a rather time consuming approach, often resulting in rather abstract than organic designs. Alternatively, image scans of native ECMs are used to fully recapitulate ECM architecture. However, both approaches impede with fast and personalized adjustments[10]. Additionally, bioprinted results often considerably differ from 3D print templates due to swelling or over extrusion and such compensation should be accounted for automatically in the design process[143],[254]. Similarly, fabrication parameters including local mechanical properties, degradability or specific materials should be incorporated into the designs to be executed by the 3D printer. To fully leverage available 3D biofabrication methods hence requires design-driven ECM architectures and seamless integration into existing biofabrication workflows[10],[143].

Towards this goal, the potential of algorithmic design to drastically enhance customization and optimization of organic designs was demonstrated. By varying individual design parameters such as wall thickness, curvature, surface roughness or degree of vascularization deliberately or driven by artificial randomness will help to attain a detailed understanding of geometrical influences on tissue formation, sustainment and healing *in vitro* and is thus a substantial building block in clinical translation. True to scale printability of alveoli models with both acrylate- resin and gelatin based resin was demonstrated.

In future, the alveolar wall-capillary interface may serve as an organotypic 3D *in vitro* model to explore direct interactions between alveoli specific pneumocytes and capillary specific endothelial cells[10] as well as patient specific drug testing of respiratory drugs.

Additionally, machine learning and artificial intelligence approaches will enable rapid optimization of organotypical 3D print templates[129]. Thinking one step ahead, this voxel based design approach combined with volumetric data and novel approaches concerning print drivers will allow for even more complex print results, e.g. by enabling the mapping of spatially defined features such as ECM stiffness or protein concentrations based on biological data sets. These can ultimately be complemented with field driven optimization including multimodal simulations and experimental feedback[10].

Acknowledgements

Thanks to the many, I had the chance to scientifically interact with and a very special note dedicated to those accompanying me throughout this journey. Thanks to all of you that have lifted the spirits and made this a fantastic chapter in my life! I would particularly like to thank:

Prof. Hauke Clausen-Schaumann and Dr. Stefanie Sudhop: Thank you Hauke and Stefanie for supervising me during this journey. Thank you for always supporting me and giving me many opportunities for my academic and personal development.

Prof. Oliver Hayden: Thank you Oli, for taking on the role of my doctoral supervisor. I especially appreciated your drive, mindset and your way of connecting people.

Prof. Michal Heymann: A special thanks goes to you, Micha. Even though our paths crossed more or less by accident, you became my mentor from day 1, I understood what you were saying from day 2 and a life long friend from day 3. Besides instrumentational developments, microfluidics, etc., it was you, who taught me so many lab hacks without I would probably still be printing a single scaffold a days. Your passion for research truly inspired me and our jokes in seemingly timeless clean room sessions kept me motivated. Incredibly, you were able to do all this while pursuing numerous other projects and becoming Junior Professor. Congratulations!

Conny Hasselberg-Christoph, Benedikt Kaufmann, Lutz Fleischhauer, Bastian Hartmann, Jun Zhang, Dr. Stefanie Kiderlen & Dr. Tanja Becke: A big thanks to the entire CANTER group including all students for the endless discussions, nice meals on the sunny patio and relaxing cake & coffee breaks.

Dr. Gerald Burgstaller, Séverine Cranz, Thomas Kellerer, Leroy Grob, Francisco Zurita, Jeanine Pestoni, Josfine Lissner & Markus Finke: Thank for being great cooperation partners. I learned a lot from all of you and was always thrilled to see new applications and methods come to life.

Bavarian State Ministry of Science and the Arts | Bavarian Research Institute for Digital Transformation (bidt): I feel honored to have been chosen as a bidt fellow and blessed to have been funded by you. Thank you **Dr. Maria Staudte** for the wonderful coordination and for bringing the graduate school to life. Another big thanks goes to the **Bavarian Academic Formum (BayWISS)** for the additional funding of my project.

Christoph Wellnhofer: A very special thank you for your continuous support in programming and data analysis. You are the best!

I would also like to thank all the wonderful people I met during my time as doctoral researcher in the CANTER group, Heymann group, Schwille group, Helmholz group and at TranslaTUM, who contributed to the inspiring work atmosphere. It has been a pleasure to work with all of you!

References

[1] Erben, A., Hörning, M., Hartmann, B., Becke, T., Eisler, S. A., Southan, A., Cranz, S., Hayden, O., Kneidinger, N., Königshoff, M., Lindner, M., Tovar, G. E. M., Burgstaller, G., Clausen-schaumann, H., Sudhop, S., Heymann, M. Precision 3D-Printed Cell Scaffolds Mimicking Native Tissue Composition and Mechanics. **2020**. https://doi.org/10.1002/adhm.202000918.

[2] Chaudhuri, O. Viscoelastic Hydrogels for 3D Cell Culture. *Biomaterials Science* **2017**. https://doi.org/10.1039/c7bm00261k.

[3] Qiu, B., Bessler, N., Figler, K., Buchholz, M. B., Rios, A. C., Malda, J., Levato, R., Caiazzo, M. Bioprinting Neural Systems to Model Central Nervous System Diseases. *Advanced Functional Materials* **2020**. https://doi.org/10.1002/adfm.201910250.

[4] Chen, Z., Zhao, R. Engineered Tissue Development in Biofabricated 3D Geometrical Confinement-A Review. *ACS Biomaterials Science and Engineering* **2019**. https://doi.org/10.1021/acsbiomaterials.8b01195.

[5] Loessner, D., Stok, K. S., Lutolf, M. P., Hutmacher, D. W., Clements, J. A., Rizzi, S. C. Bioengineered 3D Platform to Explore Cell-ECM Interactions and Drug Resistance of Epithelial Ovarian Cancer Cells. *Biomaterials* **2010**. https://doi.org/10.1016/j.biomaterials.2010.07.064.

[6] Duval, K., Grover, H., Han, L. H., Mou, Y., Pegoraro, A. F., Fredberg, J., Chen, Z. Modeling Physiological Events in 2D vs. 3D Cell Culture. *Physiology* **2017**. https://doi.org/10.1152/physiol.00036.2016.

[7] Bao, M., Xie, J., Piruska, A., Huck, W. T. S. 3D Microniches Reveal the Importance of Cell Size and Shape. *Nature Communications* **2017**. https://doi.org/10.1038/s41467-017-02163-2.

[8] Dobos, A., Gantner, F., Markovic, M., Hoorick, J. Van, Tytgat, L. On-Chip High-Definition Bioprinting of Microvascular Structures. *Biofabrication* **2020**. https://doi.org/https://doi.org/10.1088/1758-5090/abb063.

[9] Datta, P., Ayan, B., Ozbolat, I. T. Bioprinting for Vascular and Vascularized Tissue Biofabrication. *Acta Biomaterialia* **2017**. https://doi.org/10.1016/j.actbio.2017.01.035.

[10] Erben, A., Kellerer, T., Lissner, J., Eulenkamp, C., Hellerer, T., Sudhop, S., Heymann, M. Engineering Principles and Algorithmic Design Synthesis for Ultracompact Bio- Hybrid Perfusion Chip. *bioRxiv* **2022**. https://doi.org/https://doi.org/10.1101/2022.03.16.484492.

[11] Melnik, S. *Generic Model Management: Concepts and Algorithms*; Springer Science & Business Media, 2004.

[12] Forbes, G. B. *Human Body Composition*; Springer-Verlag New York Inc., 1987. https://doi.org/10.1007/978-1-4612-4654-1.

[13] Kirz, J., Jacobsen, C. The History and Future of X-Ray Microscopy. *Journal of Physics: Conference Series* **2009**. https://doi.org/10.1088/1742-6596/186/1/012001.

[14] Haguenau, F., Hawkes, P. W., Hutchison, J. L., Satiat-Jeunemaitre, B. Key Events in the History of Electron Microscopy (Multiple Letters). *Microscopy and Microanalysis* **2003**. https://doi.org/10.1017/s1431927603030538.

[15] Qin, Z., He, S., Yang, C., Yung, J. S. Y., Chen, C., Leung, C. K. S., Liu, K., Qu, J. Y. Adaptive Optics Two-Photon Microscopy Enables near-Diffraction-Limited and Functional Retinal Imaging in Vivo. *Light: Science and Applications* **2020**. https://doi.org/10.1038/s41377-020-0317-9.

[16] Prevedel, R., Diz-Muñoz, A., Ruocco, G., Antonacci, G. Brillouin Microscopy: An Emerging Tool for Mechanobiology. *Nature Methods* **2019**. https://doi.org/10.1038/s41592-019-0543-3.

[17] Seeger, M., Karlas, A., Soliman, D., Pelisek, J., Ntziachristos, V. Multimodal Optoacoustic and Multiphoton Microscopy of Human Carotid Atheroma. *Photoacoustics* **2016**. https://doi.org/10.1016/j.pacs.2016.07.001.

[18] Nguyen, V. P., Qian, W., Li, Y., Liu, B., Aaberg, M., Henry, J., Zhang, W., Wang, X., Paulus, Y. M. Chain-like Gold Nanoparticle Clusters for Multimodal Photoacoustic Microscopy and Optical Coherence Tomography Enhanced Molecular Imaging. *Nature Communications* **2021**. https://doi.org/10.1038/s41467-020-20276-z.

[19] Nair, G., Dodd, S., Ha, S. K., Koretsky, A. P., Reich, D. S. Ex Vivo MR Microscopy of a Human Brain with Multiple Sclerosis: Visualizing Individual Cells in Tissue Using Intrinsic Iron. *NeuroImage* **2020**. https://doi.org/10.1016/j.neuroimage.2020.117285.

[20] Espíndola, D., DeRuiter, R. M., Santibanez, F., Dayton, P. A., Pinton, G. Quantitative Sub-Resolution Blood Velocity Estimation Using Ultrasound Localization Microscopy Ex-Vivo and in-Vivo. *Biomedical Physics & Engineering Express* **2020**.

[21] Gupta, P., Lorentz, K. L., Haskett, D. G., Cunnane, E. M., Ramaswamy, A. K., Weinbaum, J. S., Vorp, D. A., Mandal, B. B. *Bioresorbable Silk Grafts for Small Diameter Vascular Tissue Engineering Applications: In Vitro and in Vivo Functional Analysis*; Elsevier Ltd, 2020; Vol. 105. https://doi.org/10.1016/j.actbio.2020.01.020.

[22] Engler, A. J., Sen, S., Sweeney, H. L., Discher, D. E. Matrix Elasticity Directs Stem Cell Lineage Specification. *Cell* **2006**. https://doi.org/10.1016/j.cell.2006.06.044.

[23] Berger, A. J., Linsmeier, K. M., Kreeger, P. K., Masters, K. S. Decoupling the Effects of Stiffness and Fiber Density on Cellular Behaviors via an Interpenetrating Network of Gelatin-Methacrylate and Collagen. *Biomaterials* **2017**. https://doi.org/10.1016/j.biomaterials.2017.06.039.

[24] Burgstaller, G., Sengupta, A., Vierkotten, S., Preissler, G., Lindner, M., Behr, J., Königshoff, M., Eickelberg, O. Distinct Niches within the Extracellular Matrix Dictate Fibroblast Function in (Cell Free) 3D Lung Tissue Cultures. *American journal of physiology. Lung cellular and molecular physiology* **2018**.

https://doi.org/10.1152/ajplung.00408.2017.

[25] Rianna, C., Kumar, P., Radmacher, M. The Role of the Microenvironment in the Biophysics of Cancer. *Seminars in Cell and Developmental Biology* **2018**. https://doi.org/10.1016/j.semcdb.2017.07.022.

[26] Wu, P. H., Gilkes, D. M., Wirtz, D. The Biophysics of 3D Cell Migration. *Annual Review of Biophysics* **2018**. https://doi.org/10.1146/annurev-biophys-070816-033854.

[27] Susaki, E. A., Shimizu, C., Kuno, A., Tainaka, K., Li, X., Nishi, K., Morishima, K., Ono, H., Ode, K. L., Saeki, Y., Miyamichi, K., Isa, K., Yokoyama, C., Kitaura, H., Ikemura, M., Ushiku, T., Shimizu, Y., Saito, T., Saido, T. C., Fukayama, M., Onoe, H., Touhara, K., Isa, T., Kakita, A., Shibayama, M., Ueda, H. R. Versatile Whole-Organ/Body Staining and Imaging Based on Electrolyte-Gel Properties of Biological Tissues. *Nature Communications* **2020**. https://doi.org/10.1038/s41467-020-15906-5.

[28] Darrigues, E., Nima, Z. A., Nedosekin, D. A., Watanabe, F., Alghazali, K. M., Zharov, V. P., Biris, A. S. Tracking Gold Nanorods' Interaction with Large 3D Pancreatic-Stromal Tumor Spheroids by Multimodal Imaging: Fluorescence, Photoacoustic, and Photothermal Microscopies. *Scientific reports* **2020**. https://doi.org/10.1038/s41598-020-59226-6.

[29] Bergenstråhle, J., Larsson, L., Lundeberg, J. Seamless Integration of Image and Molecular Analysis for Spatial Transcriptomics Workflows. *BMC Genomics* **2020**. https://doi.org/10.1186/s12864-020-06832-3.

[30] Alon, S., Goodwin, D. R., Sinha, A., Wassie, A. T., Chen, F., Daugharthy, E. R., Bando, Y., Kajita, A., Xue, A. G., Marrett, K., Prior, R., Cui, Y., Payne, A. C., Yao, C. C., Suk, H. J., Wang, R., Yu, C. C., Tillberg, P., Reginato, P., Pak, N., Liu, S., Punthambaker, S., Iyer, E. P. R., Kohman, R. E., Miller, J. A., Lein, E. S., Lako, A., Cullen, N., Rodig, S., Helvie, K., Abravanel, D. L., Wagle, N., Johnson, B. E., Klughammer, J., Slyper, M., Waldman, J., Jané-Valbuena, J., Rozenblatt-Rosen, O., Regev, A., Church, G. M., Marblestone, A. H., Boyden, E. S. Expansion Sequencing: Spatially Precise in Situ Transcriptomics in Intact Biological Systems. *Science* **2021**. https://doi.org/10.1126/science.aax2656.

[31] Melby, J. A., De Lange, W. J., Zhang, J., Roberts, D. S., Mitchell, S. D., Tucholski, T., Kim, G., Kyrvasilis, A., Mcilwain, S. J., Kamp, T. J., Ralphe, J. C., Ge, Y. Functionally Integrated Top-Down Proteomics for Standardized Assessment of Human Induced Pluripotent Stem Cell-Derived Engineered Cardiac Tissues. *Journal of Proteome Research* **2021**. https://doi.org/10.1021/acs.jproteome.0c00830.

[32] Kuo, C. Y., Guo, T., Cabrera-Luque, J., Arumugasaamy, N., Bracaglia, L., Garcia-Vivas, A., Santoro, M., Baker, H., Fisher, J., Kim, P. Placental Basement Membrane Proteins Are Required for Effective Cytotrophoblast Invasion in a Three-Dimensional Bioprinted Placenta Model. *Journal of Biomedical Materials Research - Part A* **2018**. https://doi.org/10.1002/jbm.a.36350.

[33] Kim, M. C., Silberberg, Y. R., Abeyaratne, R., Kamm, R. D., Asada, H. H. Computational Modeling of Three-Dimensional ECMrigidity Sensing to Guide Directed Cell Migration. *PNAS* **2018**. https://doi.org/10.1073/pnas.1717230115.

[34] Müller, S. J., Weigl, F., Bezold, C., Bächer, C., Albrecht, K., Gekle, S. A Hyperelastic Model for Simulating Cells in Flow. **2020**.

[35] Roth, C. J., Ehrl, A., Becher, T., Frerichs, I., Schittny, J. C., Weiler, N., Wall, W. A. Correlation between Alveolar Ventilation and Electrical Properties of Lung Parenchyma. *Physiological Measurement* **2015**. https://doi.org/10.1088/0967-3334/36/6/1211.

[36] Roth, C. J., Yoshihara, L., Wall, W. A. A Simplified Parametrised Model for Lung Microstructures Capable of Mimicking Realistic Geometrical and Mechanical Properties. *Computers in Biology and Medicine* **2017**. https://doi.org/10.1016/j.compbiomed.2017.07.017.

[37] Lemma, E. D., Spagnolo, B., De Vittorio, M., Pisanello, F. Studying Cell Mechanobiology in 3D: The Two-Photon Lithography Approach. *Trends in Biotechnology* **2019**. https://doi.org/10.1016/j.tibtech.2018.09.008.

[38] Levato, R., Jungst, T., Scheuring, R. G., Blunk, T., Groll, J., Malda, J. From Shape to Function: The Next Step in Bioprinting. *Advanced Materials* **2020**. https://doi.org/10.1002/adma.201906423.

[39] Matai, I., Kaur, G., Seyedsalehi, A., McClinton, A., Laurencin, C. T. Progress in 3D Bioprinting Technology for Tissue/Organ Regenerative Engineering. *Biomaterials* **2020**. https://doi.org/10.1016/j.biomaterials.2019.119536.

[40] Fendler, C. From 2D to 3D - Neurite Guiding Scaffolds for Designer Neuronal Networks. **2019**.

[41] Sacchi, M., Bansal, R., Rouwkema, J. Bioengineered 3D Models to Recapitulate Tissue Fibrosis. *Trends in Biotechnology* **2020**. https://doi.org/10.1016/j.tibtech.2019.12.010.

[42] Thannickal, V. J., Henke, C. A., Horowitz, J. C., Noble, P. W., Roman, J., Sime, P. J., Zhou, Y., Wells, R. G., White, E. S., Tschumperlin, D. J. Matrix Biology of Idiopathic Pulmonary Fibrosis: A Workshop Report of the National Heart, Lung, and Blood Institute. *American Journal of Pathology* **2014**. https://doi.org/10.1016/j.ajpath.2014.02.003.

[43] Burgstaller, G., Oehrle, B., Gerckens, M., White, E. S., Schiller, H. B., Eickelberg, O. The Instructive Extracellular Matrix of the Lung: Basic Composition and Alterations in Chronic Lung Disease. *European Respiratory Journal* **2017**. https://doi.org/10.1183/13993003.01805-2016.

[44] Bellas, E., Chen, C. S. Curr Opin Cell Biol. 2014. *Bone* **2014**. https://doi.org/10.1016/j.ceb.2014.09.006.

[45] McBeath, R., Pirone, D. M., Nelson, C. M., Bhadriraju, K., Chen, C. S. Cell Shape, Cytoskeletal Tension, and RhoA Regulate Stem Cell Lineage Commitment Rowena. *Developmental Cell* **2004**. https://doi.org/10.1016/S1534-5807(04)00075-9.

[46] Lautenschläger, F., Piel, M. Microfabricated Devices for Cell Biology: All for One and One for All. *Current Opinion in Cell Biology* **2013**. https://doi.org/10.1016/j.ceb.2012.10.017.

[47] Hippler, M., Lemma, E. D., Bertels, S., Blasco, E., Barner-Kowollik, C., Wegener,

M., Bastmeyer, M. 3D Scaffolds to Study Basic Cell Biology. *Advanced Materials* **2019**. https://doi.org/10.1002/adma.201808110.

[48] Tijore, A., Irvine, S. A., Sarig, U., Mhaisalkar, P., Baisane, V., Venkatraman, S. Contact Guidance for Cardiac Tissue Engineering Using 3D Bioprinted Gelatin Patterned Hydrogel. *Biofabrication* **2018**. https://doi.org/10.1088/1758-5090/aaa15d.

[49] Fetah, K., Tebon, P., Goudie, M. J., Eichenbaum, J., Ren, L., Barros, N., Nasiri, R., Ahadian, S., Ashammakhi, N., Dokmeci, M. R., Khademhosseini, A. The Emergence of 3D Bioprinting in Organ-on-Chip Systems. *Progress in Biomedical Engineering* **2019**. https://doi.org/10.1088/2516-1091/ab23df.

[50] Buchanan, C. F., Verbridge, S. S., Vlachos, P. P., Rylander, M. N. Flow Shear Stress Regulates Endothelial Barrier Function and Expression of Angiogenic Factors in a 3D Microfluidic Tumor Vascular Model. *Cell Adhesion and Migration* **2014**. https://doi.org/10.4161/19336918.2014.970001.

[51] Pisano, M., Triacca, V., Barbee, K. A., Swartz, M. A. An in Vitro Model of the Tumor-Lymphatic Microenvironment with Simultaneous Transendothelial and Luminal Flows Reveals Mechanisms of Flow Enhanced Invasion. *Integrative Biology* **2015**. https://doi.org/10.1039/c5ib00085h.

[52] Bock, C., Boutros, M., Camp, J. G., Clarke, L., Clevers, H., Knoblich, J. A., Liberali, P., Regev, A., Rios, A. C., Stegle, O., Stunnenberg, H. G., Teichmann, S. A., Treutlein, B., Vries, R. G. J. The Organoid Cell Atlas. *Nature Biotechnology* **2021**. https://doi.org/10.1038/s41587-020-00762-x.

[53] Dellaquila, A., Thomée, E. K., McMillan, A. H., Lesher-Pérez, S. C. *Lung-on-a-Chip Platforms for Modeling Disease Pathogenesis*; Elsevier, 2019. https://doi.org/10.1016/B978-0-12-817202-5.00004-8.

[54] Baptista, D., Teixeira, L. M., Birgani, Z. T., van Riet, S., Pasman, T., Poot, A., Stamatialis, D., Rottier, R. J., Hiemstra, P. S., Habibović, P., van Blitterswijk, C., Giselbrecht, S., Truckenmüller, R. 3D Alveolar in Vitro Model Based on Epithelialized Biomimetically Curved Culture Membranes. *Biomaterials* **2020**. https://doi.org/10.1016/j.biomaterials.2020.120436.

[55] Yi, H. G., Jeong, Y. H., Kim, Y., Choi, Y. J., Moon, H. E., Park, S. H., Kang, K. S., Bae, M., Jang, J., Youn, H., Paek, S. H., Cho, D. W. A Bioprinted Human-Glioblastoma-on-a-Chip for the Identification of Patient-Specific Responses to Chemoradiotherapy. *Nature Biomedical Engineering* **2019**. https://doi.org/10.1038/s41551-019-0363-x.

[56] Caballero, D., Kaushik, S., Correlo, V. M., Oliveira, J. M., Reis, R. L., Kundu, S. C. Organ-on-Chip Models of Cancer Metastasis for Future Personalized Medicine: From Chip to the Patient. *Biomaterials* **2017**. https://doi.org/10.1016/j.biomaterials.2017.10.005.

[57] Mirdamadi, E., Tashman, J. W., Shiwarski, D. J., Palchesko, R. N., Feinberg, A. W. FRESH 3D Bioprinting a Full-Size Model of the Human Heart. *ACS Biomaterials Science and Engineering* **2020**. https://doi.org/10.1021/acsbiomaterials.0c01133.

[58] Shrestha, A., Allen, B. N., Wiley, L. A., Tucker, B. A., Worthington, K. S. Development of High-Resolution Three-Dimensional-Printed Extracellular Matrix

Scaffolds and Their Compatibility with Pluripotent Stem Cells and Early Retinal Cells. *Journal of Ocular Pharmacology and Therapeutics* **2019**. https://doi.org/10.1089/jop.2018.0146.

[59] Mandt, D., Gruber, P., Markovic, M., Tromayer, M., Rothbauer, M., Adam Kratz, S. R., Ali, S. F., Van Hoorick, J., Holnthoner, W., Mühleder, S., Dubruel, P., Van Vlierberghe, S., Ertl, P., Liska, R., Ovsianikov, A. Fabrication of Biomimetic Placental Barrier Structures within a Microfluidic Device Utilizing Two-Photon Polymerization. *International Journal of Bioprinting* **2018**. https://doi.org/10.18063/IJB.v4i2.144.

[60] Ochs, M., Nyengaard, J. R., Jung, A., Knudsen, L., Voigt, M., Wahlers, T., Richter, J., Gundersen, H. J. G. The Number of Alveoli in the Human Lung. *American Journal of Respiratory and Critical Care Medicine* **2004**. https://doi.org/10.1164/rccm.200308-1107oc.

[61] McKleroy, W., Lyn-Kew, K., Lyn-Kew (eds), K. 500 Million Alveoli from 30,000 Feet: A Brief Primer on Lung Anatomy. In *Methods in Molecular Biology*; Humana Press, New York, NY., 2018; Vol. 1809, pp 3–15. https://doi.org/10.1007/978-1-4939-8570-8_1.

[62] Miller, A. J., Spence, J. R. In Vitro Models to Study Human Lung Development, Disease and Homeostasis The. *Physiology* **2017**. https://doi.org/10.1152/physiol.00041.2016.

[63] Fung, Y. C., Sobin, S. S. Pulmonary Alveolar Blood Flow. *Circulation research* **1972**. https://doi.org/10.1161/01.RES.32.1.117.

[64] Ivanov, K. P., Kalinina, M. K., Levkovich, Y. I. Blood Flow Velocity in Capillaries of Brain and Muscles and Its Physiological Significance. *Microvascular Research* **1981**. https://doi.org/10.1016/0026-2862(81)90084-4.

[65] Cei, D., Doryab, A., Lenz, A., Schröppel, A., Mayer, P., Burgstaller, G., Nossa, R., Ahluwalia, A., Schmid, O. Development of a Dynamic in Vitro Stretch Model of the Alveolar Interface with Aerosol Delivery. *Biotechnology and Bioengineering* **2020**. https://doi.org/10.1002/bit.27600.

[66] Davies, P. F., Tripathi, S. C. Mechanical Stress Mechanisms and the Cell: An Endothelial Paradigm. *Circulation Research* **1993**. https://doi.org/10.1161/01.res.72.2.239.

[67] Weibel, E. R. It Takes More than Cells to Make a Good Lung. *American Journal of Respiratory and Critical Care Medicine* **2013**. https://doi.org/10.1164/rccm.201212-2260OE.

[68] Hsia, C. C. W., Hyde, D. M., Weibel, E. R. Lung Structure and Gas Exchange. *Physiology & behavior* **2016**. https://doi.org/doi:10.1002/cphy.c150028.

[69] Doryab, A., Tas, S., Taskin, M. B., Yang, L., Hilgendorff, A., Groll, J., Wagner, D. E., Schmid, O. Evolution of Bioengineered Lung Models: Recent Advances and Challenges in Tissue Mimicry for Studying the Role of Mechanical Forces in Cell Biology. *Advanced Functional Materials* **2019**. https://doi.org/10.1002/adfm.201903114.

[70] Booth, A. J., Hadley, R., Cornett, A. M., Dreffs, A. A., Matthes, S. A., Tsui, J. L.,

Weiss, K., Horowitz, J. C., Fiore, V. F., Barker, T. H., Moore, B. B., Martinez, F. J., Niklason, L. E., White, E. S. Acellular Normal and Fibrotic Human Lung Matrices as a Culture System for in Vitro Investigation. *American Journal of Respiratory and Critical Care Medicine* **2012**. https://doi.org/10.1164/rccm.201204-0754OC.

[71] Goss, B. C., McGee, K. P., Ehman, E. C., Manduca, A., Ehman, R. L. Magnetic Resonance Elastography of the Lung: Technical Feasibility. *Magnetic Resonance in Medicine* **2006**. https://doi.org/10.1002/mrm.21053.

[72] Roan, E., Waters, C. M. What Do We Know about Mechanical Strain in Lung Alveoli? *American Journal of Physiology - Lung Cellular and Molecular Physiology* **2011**. https://doi.org/10.1152/ajplung.00105.2011.

[73] Wagner, D. E., Ubags, N. D., Troosters, T., Alejandre Alcazar, M. A. Fostering the Integration of Basic Respiratory Science and Translational Pulmonary Medicine for the Future. *American journal of physiology. Lung cellular and molecular physiology* **2020**. https://doi.org/10.1152/ajplung.00361.2020.

[74] Singhal, T. Review on COVID19 Disease so Far. *The Indian Journal of Pediatrics* **2020**.

[75] Mannino, D. M., Sanderson, W. T. Using Big Data to Reveal Chronic Respiratory Disease Mortality Patterns and Identify Potential Public Health Interventions. *JAMA - Journal of the American Medical Association* **2017**. https://doi.org/10.1001/jama.2017.11746.

[76] Ma, J., Ward, E. M., Siegel, R. L., Jemal, A. Temporal Trends in Mortality in the United States, 1969-2013. *JAMA - Journal of the American Medical Association* **2015**. https://doi.org/10.1001/jama.2015.12319.

[77] Nossa, R., Costa, J., Cacopardo, L., Ahluwalia, A. Breathing in Vitro: Designs and Applications of Engineered Lung Models. *Journal of tissue engineering* **2021**. https://doi.org/10.1177/20417314211008696.

[78] Perrin, S. Preclinical Research: Make Mouse Studies Work. *Nature* **2014**. https://doi.org/10.1038/507423a.

[79] Scott, S., Kranz, J. E., Cole, J., Lincecum, J. M., Thompson, K., Kelly, N., Bostrom, A., Theodoss, J., Al-Nakhala, B. M., Vieira, F. G., Ramasubbu, J., Heywood, J. A. Design, Power, and Interpretation of Studies in the Standard Murine Model of ALS. *Amyotrophic Lateral Sclerosis* **2008**. https://doi.org/10.1080/17482960701856300.

[80] Liu, M., Xu, J., Souza, P., Tanswell, B., Tanswell, A. K., Post, M. The Effect of Mechanical Strain on Fetal Rat Lung Cell Proliferation: Comparison of Two-and Three-Dimensional Culture Systems. *In Vitro Cell Dev. Biol. Anim.* **1995**.

[81] Wirtz, H. R., Dobbs, L. G. The Effects of Mechanical Forces on Lung Functions. *Respiration Physiology* **2000**. https://doi.org/10.1016/S0034-5687(99)00092-4.

[82] Branchfield, K., Li, R., Lungova, V., Verheyden, J. M., McCulley, D., Sun, X. A Three-Dimensional Study of Alveologenesis in Mouse Lung. *Developmental Biology* **2016**. https://doi.org/10.1016/j.ydbio.2015.11.017.

[83] Harunaga, J. S., Doyle, A. D., Yamada, K. M. Local and Global Dynamics of the Basement Membrane during Branching Morphogenesis Require Protease Activity and Actomyosin Contractility. *Developmental Biology* **2014**.

https://doi.org/10.1016/j.ydbio.2014.08.014.

[84] Rockich, B. E., Hrycaj, S. M., Shih, H. P., Nagy, M. S., Ferguson, M. A. H., Kopp, J. L., Sander, M., Wellik, D. M., Spence, J. R. Sox9 Plays Multiple Roles in the Lung Epithelium during Branching Morphogenesis. *Proceedings of the National Academy of Sciences of the United States of America* **2013**. https://doi.org/10.1073/pnas.1311847110.

[85] Fröhlich, E., Salar-Behzadi, S. Toxicological Assessment of Inhaled Nanoparticles: Role of in Vivo, Ex Vivo, in Vitro, and in Silico Studies. *International Journal of Molecular Sciences* **2014**. https://doi.org/10.3390/ijms15034795.

[86] Irvin, C. G., Bates, J. H. Measuring the Lung Function in the Mouse: The Challenge of Size Airwayanimal Models of Diseaseasthmaforced Oscillationlungmechanicsmouse. *Respiratory Research* **2003**.

[87] Lewis, K. J. R., Hall, J. K., Kiyotake, E. A., Christensen, T., Balasubramaniam, V., Anseth, K. S. Epithelial-Mesenchymal Crosstalk Influences Cellular Behavior in a 3D Alveolus-Fibroblast Model System. *Biomaterials* **2018**. https://doi.org/10.1016/j.biomaterials.2017.11.008.

[88] Kamotani, Y., Bersano-Begey, T., Kato, N., Tung, Y. C., Huh, D., Song, J. W., Takayama, S. Individually Programmable Cell Stretching Microwell Arrays Actuated by a Braille Display. *Biomaterials* **2008**. https://doi.org/10.1016/j.biomaterials.2008.02.019.

[89] Huh, D., Kim, H. J., Fraser, J. P., Shea, D. E., Khan, M., Bahinski, A., Hamilton, G. A., Ingber, D. E. Microfabrication of Human Organs-on-Chips. *Nature Protocols* **2013**. https://doi.org/10.1038/nprot.2013.137.

[90] Huh, D., Matthews, B. D., Mammoto, A., Montoya-Zavala, M., Hsin, H. Y., Ingber, D. E. Reconstituting Organ-Level Lung. *Science* **2010**. https://doi.org/10.1126/science.1188302.

[91] Huh, D. A Human Breathing Lung-on-a-Chip. *Annals of the American Thoracic Society* **2015**. https://doi.org/10.1513/AnnalsATS.201410-442MG.

[92] Almacellas-Rabaiget, O., Monaco, P., Huertas-Martinez, J., García-Monclús, S., Chicón-Bosch, M., Maqueda-Marcos, S., Fabra-Heredia, I., Herrero-Martín, D., Rello-Varona, S., de Alava, E., López-Alemany, R., Giangrande, P. H., Tirado, O. M. LOXL2 Promotes Oncogenic Progression in Alveolar Rhabdomyosarcoma Independently of Its Catalytic Activity. *Cancer Letters* **2020**. https://doi.org/10.1016/j.canlet.2019.12.040.

[93] Harney, J., Bajaj, P., Finley, J. E., Kopec, A. K., Koza-Taylor, P. H., Boucher, G. G., Lanz, T. A., Doshna, C. M., Somps, C. J., Adkins, K., Houle, C. An in Vitro Alveolar Epithelial Cell Model Recapitulates LRRK2 Inhibitor-Induced Increases in Lamellar Body Size Observed in Preclinical Models. *Toxicology in Vitro* **2020**. https://doi.org/10.1016/j.tiv.2020.105012.

[94] Zamprogno, P., Wüthrich, S., Achenbach, S., Thoma, G., Stucki, J. D., Hobi, N., Schneider-Daum, N., Lehr, C. M., Huwer, H., Geiser, T., Schmid, R. A., Guenat, O. T. Second-Generation Lung-on-a-Chip with an Array of Stretchable Alveoli Made with a Biological Membrane. *Communications Biology*. 2021.

https://doi.org/10.1038/s42003-021-01695-0.

[95] Dong, J., Qiu, Y., Lv, H., Yang, Y., Zhu, Y. Investigation on Microparticle Transport and Deposition Mechanics in Rhythmically Expanding Alveolar Chip. *Micromachines* **2021**. https://doi.org/10.3390/mi12020184.

[96] van der Vaart, J., Clevers, H. Airway Organoids as Models of Human Disease. *Journal of Internal Medicine* **2020**. https://doi.org/10.1111/joim.13075.

[97] Li, Y., Wu, Q., Sun, X., Shen, J., Chen, H. Organoids as a Powerful Model for Respiratory Diseases. *Stem Cells International* **2020**. https://doi.org/10.1155/2020/5847876.

[98] Sano, K., Usui, M., Moritani, Y., Nakazawa, K., Hanatani, T., Kondo, H., Nakatomi, M., Onizuka, S., Iwata, T., Sato, T., Togari, A., Ariyoshi, W., Nishihara, T., Nakashima, K. Co-Cultured Spheroids of Human Periodontal Ligament Mesenchymal Stem Cells and Vascular Endothelial Cells Enhance Periodontal Tissue Regeneration. *Regenerative Therapy* **2020**. https://doi.org/10.1016/j.reth.2019.12.008.

[99] Grigoryan, B., Paulsen, S. J., Corbett, D. C., Sazer, D. W., Fortin, C. L., Zaita, A. J., Greenfield, P. T., Calafat, N. J., Gounley, J. P., Ta, A. H., Johansson, F., Randles, A., Rosenkrantz, J. E., Louis-Rosenberg, J. D., Galie, P. A., Stevens, K. R., Miller, J. S. Multivascular Networks and Functional Intravascular Topologies within Biocompatible Hydrogels. *Science* **2019**. https://doi.org/10.1126/science.aav9750.

[100] Kang, D., Park, J. A., Kim, W., Kim, S., Lee, H. R., Kim, W. J., Yoo, J. Y., Jung, S. All-Inkjet-Printed 3D Alveolar Barrier Model with Physiologically Relevant Microarchitecture. *Advanced Science* **2021**. https://doi.org/10.1002/advs.202004990.

[101] Ng, W. L., Ayi, T. C., Liu, Y.-C., Sing, S. L., Yeong, W. Y., Tan, B.-H. Fabrication and Characterization of 3D Bioprinted Triple-Layered Human Alveolar Lung Models. *International Journal of Bioprinting* **2021**. https://doi.org/10.18063/ijb.v7i2.332.

[102] Dong, Y., Jin, G., Hong, Y., Zhu, H., Lu, T. J., Xu, F., Bai, D., Lin, M. Engineering the Cell Microenvironment Using Novel Photoresponsive Hydrogels. *ACS Applied Materials and Interfaces* **2018**. https://doi.org/10.1021/acsami.7b17751.

[103] Dunphy, S. E., Bratt, J. A. J., Akram, K. M., Forsyth, N. R., El Haj, A. J. Hydrogels for Lung Tissue Engineering: Biomechanical Properties of Thin Collagen-Elastin Constructs. *Journal of the Mechanical Behavior of Biomedical Materials*. 2014, pp 251–259. https://doi.org/10.1016/j.jmbbm.2014.04.005.

[104] Griffith, C. K., Miller, C., Sainson, R. C. A., Calvert, J. W., Jeon, N. L., Hughes, C. C. W., George, S. C. Diffusion Limits of an in Vitro Thick Prevascularized Tissue. *Tissue Engineering* **2005**. https://doi.org/10.1089/ten.2005.11.257.

[105] Murphy, S. V., Atala, A. 3D Bioprinting of Tissues and Organs. *Nature Biotechnology* **2014**. https://doi.org/10.1038/nbt.2958.

[106] Hinz, B. Mechanical Aspects of Lung Fibrosis: A Spotlight on the Myofibroblast. *Proc Am Thorac Soc.* **2012**. https://doi.org/10.1513/pats.201202-017AW.

[107] Xu, B.-B., Zhang, Y.-L., Xia, H., Dong, W.-F., Ding, H., Sun, H.-B. Fabrication and

Multifunction Integration of Microfluidic Chips by Femtosecond Laser Direct Writing. *Lab on a Chip* **2013**. https://doi.org/10.1039/c3lc50160d.

[108] Ishahak, M., Hill, J., Amin, Q., Wubker, L., Hernandez, A., Mitrofanova, A., Sloan, A., Fornoni, A., Agarwal, A. Modular Microphysiological System for Modeling of Biologic Barrier Function. *Frontiers in Bioengineering and Biotechnology* **2020**. https://doi.org/10.3389/fbioe.2020.581163.

[109] Huh, D., Hamilton, G. A., Ingber, D. E. From 3D Cell Culture to Organs-on-Chips. *Trends in Cell Biology* **2011**. https://doi.org/10.1016/j.tcb.2011.09.005.

[110] Kaushik, G., Ponnusamy, M. P., Batra, S. K. Concise Review: Current Status of Three-Dimensional Organoids as Preclinical Models. *Stem Cells* **2018**. https://doi.org/10.1002/stem.2852.

[111] Qian, X., Song, H., Ming, G. L. Brain Organoids: Advances, Applications and Challenges. *Development (Cambridge)* **2019**. https://doi.org/10.1242/dev.166074.

[112] McGowan, S. E. Extracellular Matrix and the Regulation of Lung Development and Repair 1. *The FASEB Journal* **1992**. https://doi.org/10.1096/fasebj.6.11.1644255.

[113] Workman, M. J., Mahe, M. M., Trisno, S., Poling, H. M., Watson, C. L., Sundaram, N., Chang, C. F., Schiesser, J., Aubert, P., Stanley, E. G., Elefanty, A. G., Miyaoka, Y., Mandegar, M. A., Conklin, B. R., Neunlist, M., Brugmann, S. A., Helmrath, M. A., Wells, J. M. Engineered Human Pluripotent-Stem-Cell-Derived Intestinal Tissues with a Functional Enteric Nervous System. *Nature Medicine* **2017**. https://doi.org/10.1038/nm.4233.

[114] Bhise, N. S., Manoharan, V., Massa, S., Tamayol, A., Ghaderi, M., Miscuglio, M., Lang, Q., Zhang, Y. S., Shin, S. R., Calzone, G., Annabi, N., Shupe, T. D., Bishop, C. E., Atala, A., Dokmeci, M. R., Khademhosseini, A. A Liver-on-a-Chip Platform with Bioprinted Hepatic Spheroids. *Biofabrication* **2016**. https://doi.org/10.1088/1758-5090/8/1/014101.

[115] Lee, J. M., Yeong, W. Y. Design and Printing Strategies in 3D Bioprinting of Cell-Hydrogels: A Review. *Advanced Healthcare Materials* **2016**. https://doi.org/10.1002/adhm.201600435.

[116] Colosi, C., Shin, S. R., Manoharan, V., Massa, S., Costantini, M., Barbetta, A., Dokmeci, Mehmet Remzi Dentini, M., Khademhosseini, A. Microfluidic Bioprinting of Heterogeneous 3D Tissue Constructs Using Low Viscosity Bioink. *Advanced Materials* **2016**. https://doi.org/10.1002/adma.201503310.

[117] Duan, B. State-of-the-Art Review of 3D Bioprinting for Cardiovascular Tissue Engineering. *Annals of Biomedical Engineering* **2017**. https://doi.org/10.1007/s10439-016-1607-5.

[118] Fransen, M. F. J., Addario, G., Bouten, C. V. C., Halary, F., Moroni, L., Mota, C. Bioprinting of Kidney in Vitro Models: Cells, Biomaterials, and Manufacturing Techniques. *Essays in Biochemistry* **2021**. https://doi.org/10.1042/EBC20200158.

[119] Augustine, R. Skin Bioprinting: A Novel Approach for Creating Artificial Skin from Synthetic and Natural Building Blocks. *Progress in Biomaterials* **2018**. https://doi.org/10.1007/s40204-018-0087-0.

[120] Albanna, M., Binder, K. W., Murphy, S. V., Kim, J., Qasem, S. A., Zhao, W., Tan, J., El-Amin, I. B., Dice, D. D., Marco, J., Green, J., Xu, T., Skardal, A., Holmes, J. H., Jackson, J. D., Atala, A., Yoo, J. J. In Situ Bioprinting of Autologous Skin Cells Accelerates Wound Healing of Extensive Excisional Full-Thickness Wounds. *Scientific Reports* **2019**. https://doi.org/10.1038/s41598-018-38366-w.

[121] He, P., Zhao, J., Zhang, J., Li, B., Gou, Z., Gou, M., Li, X. Bioprinting of Skin Constructs for Wound Healing. *Burns & Trauma* **2018**. https://doi.org/10.1186/s41038-017-0104-x.

[122] Galliger, Z., Vogt, C. D., Panoskaltsis-Mortari, A. 3D Bioprinting for Lungs and Hollow Organs. *Translational Research* **2019**. https://doi.org/10.1016/j.trsl.2019.05.001.

[123] Barros, A. S., Costa, A., Sarmento, B. Building Three-Dimensional Lung Models for Studying Pharmacokinetics of Inhaled Drugs. *Advanced Drug Delivery Reviews* **2021**. https://doi.org/10.1016/j.addr.2020.09.008.

[124] Wang, X., Zhang, X., Dai, X., Wang, X., Li, X., Diao, J., Xu, T. Tumor-like Lung Cancer Model Based on 3D Bioprinting. *3 Biotech* **2018**. https://doi.org/10.1007/s13205-018-1519-1.

[125] Knowlton, S., Onal, S., Yu, C. H., Zhao, J. J., Tasoglu, S. Bioprinting for Cancer Research. *Trends in Biotechnology* **2015**. https://doi.org/http://dx.doi.org/10.1016/j.tibtech.2015.06.007.

[126] Mao, S., Pang, Y., Liu, T., Shao, Y., He, J., Yang, H., Mao, Y., Sun, W. Bioprinting of in Vitro Tumor Models for Personalized Cancer Treatment: A Review. *Biofabrication* **2020**. https://doi.org/10.1088/1758-5090/ab97c0.

[127] Horvath, L., Umehara, Y., Jud, C., Blank, F., Petri-Fink, A., Rothen-Rutishauser, B. Engineering an in Vitro Air-Blood Barrier by 3D Bioprinting. *Scientific Reports* **2015**. https://doi.org/10.1038/srep07974.

[128] Park, J. Y., Ryu, H., Lee, B., Ha, D. H., Ahn, M., Kim, S., Kim, J. Y., Jeon, N. L., Cho, D. W. Development of a Functional Airway-on-a-Chip by 3D Cell Printing. *Biofabrication*. 2019. https://doi.org/10.1088/1758-5090/aae545.

[129] Murphy, S. V., De Coppi, P., Atala, A. Opportunities and Challenges of Translational 3D Bioprinting. *Nature Biomedical Engineering* **2020**. https://doi.org/10.1038/s41551-019-0471-7.

[130] Zhang, J., Byers, P., Erben, A., Frank, C., Schulte-Spechtel, L., Heymann, M., Docheva, D., Huber, H. P., Sudhop, S., Clausen-Schaumann, H. Single Cell Bioprinting with Ultrashort Laser Pulses. *Advanced Functional Materials* **2021**. https://doi.org/10.1002/adfm.202100066.

[131] Smith, L. E., Smallwood, R., Macneil, S. A Comparison of Imaging Methodologies for 3D Tissue Engineering. *Microscopy Research and Technique* **2010**. https://doi.org/10.1002/jemt.20859.

[132] Jonkman, J., Brown, C. M., Wright, G. D., Anderson, K. I., North, A. J. Tutorial: Guidance for Quantitative Confocal Microscopy. *Nature Protocols* **2020**. https://doi.org/10.1038/s41596-020-0313-9.

[133] Helmchen, F., Denk, W. Deep Tissue Two-Photon Microscopy. *Nature Methods*

2005. https://doi.org/10.1038/nmeth818.

[134] Yang, B., Lange, M., Millett-Sikking, A., Solak, A. C., Kumar, S. V., Wang, W., Kobayashi, H., McCarroll, M. N., Whitehead, L. W., Fiolka, R. P., Kornberg, T. B., York, A. G., Royer, L. A. High-Resolution , Large Imaging Volume , and Multi-View Single Objective Light-Sheet Microscopy. *bioRxiv* **2021**.

[135] Ueda, H. R., Dodt, H. U., Osten, P., Economo, M. N., Chandrashekar, J., Keller, P. J. Whole-Brain Profiling of Cells and Circuits in Mammals by Tissue Clearing and Light-Sheet Microscopy. *Neuron* **2020**. https://doi.org/10.1016/j.neuron.2020.03.004.

[136] Rawson, S. D., Maksimcuka, J., Withers, P. J., Cartmell, S. H. X-Ray Computed Tomography in Life Sciences. *BMC Biology* **2020**. https://doi.org/10.1186/s12915-020-0753-2.

[137] Booij, T. H., Price, L. S., Danen, E. H. J. 3D Cell-Based Assays for Drug Screens: Challenges in Imaging, Image Analysis, and High-Content Analysis. *SLAS Discovery* **2019**. https://doi.org/10.1177/2472555219830087.

[138] Zhu, X., Wang, Z., Teng, F. A Review of Regulated Self-Organizing Approaches for Tissue Regeneration. *Progress in Biophysics and Molecular Biology* **2021**. https://doi.org/10.1016/j.pbiomolbio.2021.07.006.

[139] Roudavski, S. Towards Morphogenesis in Architecture. *International Journal of Architectural Computing* **2009**. https://doi.org/10.1260/147807709789621266.

[140] Zhang, X., Zhang, Y. Tissue Engineering Applications of Three-Dimensional Bioprinting. *Cell Biochemistry and Biophysics*. 2015, pp 777–782. https://doi.org/10.1007/s12013-015-0531-x.

[141] du Plessis, A., Broeckhoven, C., Yadroitsava, I., Yadroitsev, I., Hands, C. H., Kunju, R., Bhate, D. Beautiful and Functional: A Review of Biomimetic Design in Additive Manufacturing. *Additive Manufacturing* **2019**. https://doi.org/10.1016/j.addma.2019.03.033.

[142] Szojka, A., Lalh, K., Andrews, S. H. J., Jomha, N. M., Osswald, M., Adesida, A. B. Biomimetic 3D Printed Scaffolds for Meniscus Tissue Engineering. *Bioprinting* **2017**. https://doi.org/10.1016/j.bprint.2017.08.001.

[143] Ozbolat, I., Gudapati, H. A Review on Design for Bioprinting. *Bioprinting*. 2016, pp 1–14. https://doi.org/10.1016/j.bprint.2016.11.001.

[144] Junk, S., Burkart, L. Comparison of CAD Systems for Generative Design for Use with Additive Manufacturing. *Procedia CIRP* **2021**. https://doi.org/10.1016/j.procir.2021.05.126.

[145] brahim T. Ozbolat, M. H. Current Advances and Future Perspectives in Extrusion-Based Bioprinting. *Biomaterials* **2016**. https://doi.org/http://dx.doi.org/10.1016/j.biomaterials.2015.10.076.

[146] Gómez, S., Vlad, M. D., López, J., Fernández, E. Design and Properties of 3D Scaffolds for Bone Tissue Engineering. *Acta Biomaterialia*. 2016, pp 341–350. https://doi.org/10.1016/j.actbio.2016.06.032.

[147] Bernal, P. N., Delrot, P., Loterie, D., Li, Y., Malda, J., Moser, C., Levato, R.

Volumetric Bioprinting of Complex Living-Tissue Constructs within Seconds. *Advanced Materials* **2019**. https://doi.org/10.1002/adma.201904209.

[148] Li, X., Liu, B., Pei, B., Chen, J., Zhou, D., Peng, J., Zhang, X., Jia, W., Xu, T. Inkjet Bioprinting of Biomaterials. *Chemical Reviews* **2020**. https://doi.org/10.1021/acs.chemrev.0c00008.

[149] Masaeli, E., Forster, V., Picaud, S., Karamali, F., Nasr-Esfahani, M. H., Marquette, C. Tissue Engineering of Retina through High Resolution 3-Dimensional Inkjet Bioprinting. *Biofabrication* **2020**. https://doi.org/10.1088/1758-5090/ab4a20.

[150] Bourdon, L., Maurin, J. C., Gritsch, K., Brioude, A., Salles, V. Improvements in Resolution of Additive Manufacturing: Advances in Two-Photon Polymerization and Direct-Writing Electrospinning Techniques. *ACS Biomaterials Science and Engineering* **2018**. https://doi.org/10.1021/acsbiomaterials.8b00810.

[151] Gill, E. L., Li, X., Birch, M. A., Huang, Y. Y. S. Multi-Length Scale Bioprinting towards Simulating Microenvironmental Cues. *Bio-Design and Manufacturing* **2018**. https://doi.org/10.1007/s42242-018-0014-1.

[152] Ma, J., Li, C., Huang, N., Wang, X., Tong, M., Ngan, A. H. W., Chan, B. P. Multiphoton Fabrication of Fibronectin-Functionalized Protein Micropatterns: Stiffness-Induced Maturation of Cell-Matrix Adhesions in Human Mesenchymal Stem Cells. *ACS Applied Materials and Interfaces* **2017**. https://doi.org/10.1021/acsami.7b07064.

[153] Kiefer, P., Hahn, V., Nardi, M., Yang, L., Blasco, E., Barner-Kowollik, C., Wegener, M. Sensitive Photoresists for Rapid Multiphoton 3D Laser Micro- and Nanoprinting. *Advanced Optical Materials* **2020**. https://doi.org/10.1002/adom.202000895.

[154] Richter, B., Hahn, V., Bertels, S., Claus, T. K., Wegener, M., Delaittre, G., Barner-Kowollik, C., Bastmeyer, M., Richter, B., Hahn, V., Bertels, S., Bastmeyer, M., Wegener, M., Claus, T. K., Delaittre, G., Barner-Kowollik Preparative Macromolecular Chemistry, C., Barner-Kowollik, C. Guiding Cell Attachment in 3D Microscaffolds Selectively Functionalized with Two Distinct Adhesion Proteins. **2017**. https://doi.org/10.1002/adma.201604342.

[155] Silbernagel, N., Körner, A., Balitzki, J., Jaggy, M., Bertels, S., Richter, B., Hippler, M., Hellwig, A., Hecker, M., Bastmeyer, M., Ullrich, N. D. Shaping the Heart: Structural and Functional Maturation of IPSC-Cardiomyocytes in 3D-Micro-Scaffolds. *Biomaterials* **2020**. https://doi.org/10.1016/j.biomaterials.2019.119551.

[156] Fendler, C., Denker, C., Harberts, J., Bayat, P., Zierold, R., Loers, G., Münzenberg, M., Blick, R. H. Microscaffolds by Direct Laser Writing for Neurite Guidance Leading to Tailor-Made Neuronal Networks. *Advanced Biosystems* **2019**. https://doi.org/10.1002/adbi.201800329.

[157] Harberts, J., Fendler, C., Teuber, J., Siegmund, M., Silva, A., Rieck, N., Wolpert, M., Zierold, R., Blick, R. H. Toward Brain-on-a-Chip: Human Induced Pluripotent Stem Cell-Derived Guided Neuronal Networks in Tailor-Made 3D Nanoprinted Microscaffolds. *ACS Nano* **2020**. https://doi.org/10.1021/acsnano.0c04640.

[158] Ovsianikov, A., Deiwick, A., Van Vlierberghe, S., Pflaum, M., Wilhelmi, M., Dubruel, P., Chichkov, B. Laser Fabrication of 3D Gelatin Scaffolds for the Generation of Bioartificial Tissues. *Materials* **2010**.

https://doi.org/10.3390/ma4010288.

[159] Van Hoorick, J., Tytgat, L., Dobos, A., Ottevaere, H., Van Erps, J., Thienpont, H., Ovsianikov, A., Dubruel, P., Van Vlierberghe, S. (Photo-)Crosslinkable Gelatin Derivatives for Biofabrication Applications. *Acta Biomaterialia* **2019**. https://doi.org/10.1016/j.actbio.2019.07.035.

[160] Engelhardt, S., Hoch, E., Borchers, K., Meyer, W., Krüger, H., Tovar, G. E. M., Gillner, A. Fabrication of 2D Protein Microstructures and 3D Polymer-Protein Hybrid Microstructures by Two-Photon Polymerization. *Biofabrication* **2011**. https://doi.org/10.1088/1758-5082/3/2/025003.

[161] Dickerson, M. B., Dennis, P. B., Tondiglia, V. P., Nadeau, Ll. J., Singh, K. M., Drummy, L. F., Partlow, B. P., Brown, D. P., Omenetto, F. G., Kaplan, D. L., Naik, R. R. 3D Printing of Regenerated Silk Fibroin and Antibody-Containing Microstructures via Multi-Photon Lithography. *ACS Biomaterials Science & Engineering* **2017**. https://doi.org/10.1021/acsbiomaterials.7b00338.

[162] Sun, Y.-L., Li, Q., Sun, S.-M., Huang, J.-C., Zheng, B.-Y., Chen, Q.-D., Shao, Z.-Z., Sun, H.-B. Aqueous Multiphoton Lithography with Multifunctional Silk-Centred Bio-Resists. *Nature Communications* **2015**. https://doi.org/10.1038/ncomms9612.

[163] Lay, C. L., Lee, Y. H., Lee, M. R., Phang, Y., Ling, X. Y. Formulating an Ideal Protein Photoresist for Fabricating Dynamic Microstructures with High Aspect Ratios and Uniform Responsiveness. *ACS Applied Materials & Interfaces* **2016**. https://doi.org/10.1021/acsami.6b02306.

[164] Su, P. J., Tran, Q. A., Fong, J. J., Eliceiri, K. W., Ogle, B. M., Campagnola, P. J. Mesenchymal Stem Cell Interactions with 3D ECM Modules Fabricated via Multiphoton Excited Photochemistry. *Biomacromolecules* **2012**. https://doi.org/10.1021/bm300949k.

[165] Nishiguchi, A., Kapiti, G., Höhner, J. R., Singh, S., Moeller, M. In Situ 3D-Printing Using a Bio-Ink of Protein–Photosensitizer Conjugates for Single-Cell Manipulation. *ACS Applied Bio Materials* **2020**. https://doi.org/10.1021/acsabm.0c00116.

[166] Tong, M. H., Huang, N., Zhang, W., Zhou, Z. L., Ngan, A. H. W., Du, Y., Chan, B. P. Multiphoton Photochemical Crosslinking-Based Fabrication of Protein Micropatterns with Controllable Mechanical Properties for Single Cell Traction Force Measurements. *Scientific Reports* **2016**. https://doi.org/10.1038/srep20063.

[167] Chan, B. P., Ma, J. N., Xu, J. Y., Li, C. W., Cheng, J. P., Cheng, S. H. Femto-Second Laser-Based Free Writing of 3D Protein Microstructures and Micropatterns with Sub-Micrometer Features: A Study on Voxels, Porosity, and Cytocompatibility. *Advanced Functional Materials* **2014**. https://doi.org/10.1002/adfm.201300709.

[168] Khripin, C. Y., Brinker, C. J., Kaehr, B. Mechanically Tunable Multiphoton Fabricated Protein Hydrogels Investigated Using Atomic Force Microscopy. *Soft Matter* **2010**. https://doi.org/10.1039/c001193b.

[169] Torgersen, J., Qin, X. H., Li, Z., Ovsianikov, A., Liska, R., Stampfl, J. Hydrogels for Two-Photon Polymerization: A Toolbox for Mimicking the Extracellular Matrix. *Advanced Functional Materials* **2013**. https://doi.org/10.1002/adfm.201203880.

[170] Pennacchio, F. A., Fedele, C., De Martino, S., Cavalli, S., Vecchione, R., Netti, P. A. Three-Dimensional Microstructured Azobenzene-Containing Gelatin as a Photoactuable Cell Confining System. *ACS Applied Materials and Interfaces* **2018**. https://doi.org/10.1021/acsami.7b13176.

[171] Worthington, K. S., Wiley, L. A., Kaalberg, E. E., Collins, M. M., Mullins, R. F., Stone, E. M., Tucker, B. A. Two-Photon Polymerization for Production of Human IPSC-Derived Retinal Cell Grafts. *Acta Biomaterialia* **2017**. https://doi.org/10.1016/j.actbio.2017.03.039.

[172] Buch-Månson, N., Spangenberg, A., Gomez, L. P. C., Malval, J. P., Soppera, O., Martinez, K. L. Rapid Prototyping of Polymeric Nanopillars by 3D Direct Laser Writing for Controlling Cell Behavior. *Scientific Reports* **2017**. https://doi.org/10.1038/s41598-017-09208-y.

[173] Serien, D., Takeuchi, S. Multi-Component Microscaffold with 3D Spatially Defined Proteinaceous Environment. *ACS Biomaterials Science and Engineering* **2017**. https://doi.org/10.1021/acsbiomaterials.6b00695.

[174] Parkatzidis, K., Chatzinikolaidou, M., Kaliva, M., Bakopoulou, A., Farsari, M., Vamvakaki, M. Multiphoton 3D Printing of Biopolymer-Based Hydrogels. *ACS Biomaterials Science and Engineering* **2019**. https://doi.org/10.1021/acsbiomaterials.9b01300.

[175] Yin, H., Caceres, M. D., Yan, Z., Schieker, M., Nerlich, M., Docheva, D. Tenomodulin Regulates Matrix Remodeling of Mouse Tendon Stem/Progenitor Cells in an Ex Vivo Collagen I Gel Model. *Biochemical and Biophysical Research Communications* **2019**. https://doi.org/10.1016/j.bbrc.2019.03.063.

[176] Pryce, B. A., Brent, A. E., Murchison, N. D., Tabin, C. J., Schweitzer, R. Generation of Transgenic Tendon Reporters, ScxGFP and ScxAP, Using Regulatory Elements of the Scleraxis Gene. *Developmental Dynamics* **2007**. https://doi.org/10.1002/dvdy.21179.

[177] Hörning, M., Nakahata, M., Linke, P., Yamamoto, A., Veschgini, M., Kaufmann, S., Takashima, Y., Harada, A., Tanaka, M. Dynamic Mechano-Regulation of Myoblast Cells on Supramolecular Hydrogels Cross-Linked by Reversible Host-Guest Interactions. *Scientific Reports* **2017**. https://doi.org/10.1038/s41598-017-07934-x.

[178] Garcia, A. J., Vega, M. D., Boettiger, D. Modulation of Cell Proliferation and Differentiation through Substrate-Dependent Changes in Fibronectin Conformation Andre´s. *Molecular Biology of the Cell* **1999**. https://doi.org/10.1016/j.cpc.2005.06.001.

[179] Peng, T., Thorn, K., Schroeder, T., Wang, L., Theis, F. J., Marr, C., Navab, N. A BaSiC Tool for Background and Shading Correction of Optical Microscopy Images. *Nature Communications* **2017**. https://doi.org/10.1038/ncomms14836.

[180] Sneddon, I. N. The Relation between Load and Penetration in the Axisymmetric Boussinesq Problem for a Punch of Arbitrary Profile. *International Journal of Engineering Science* **1965**. https://doi.org/10.1016/0020-7225(65)90019-4.

[181] Álvarez-Asencio, R., Thormann, E., Rutland, M. W. Note: Determination of Torsional Spring Constant of Atomic Force Microscopy Cantilevers: Combining

Normal Spring Constant and Classical Beam Theory. *Review of Scientific Instruments* **2013**. https://doi.org/10.1063/1.4820345.

[182] Prein, C., Warmbold, N., Farkas, Z., Schieker, M., Aszodi, A., Clausen-Schaumann, H. Structural and Mechanical Properties of the Proliferative Zone of the Developing Murine Growth Plate Cartilage Assessed by Atomic Force Microscopy. *Matrix Biology* **2016**. https://doi.org/10.1016/j.matbio.2015.10.001.

[183] Docheva, D., Padula, D., Popov, C., Mutschler, W., Clausen-Schaumann, H., Schieker, M. Researching into the Cellular Shape, Volume and Elasticity of Mesenchymal Stem Cells, Osteoblasts and Osteosarcoma Cells by Atomic Force Microscopy: Stem Cells. *Journal of Cellular and Molecular Medicine* **2008**. https://doi.org/10.1111/j.1582-4934.2007.00138.x.

[184] Hartmann, B., Fleischhauer, L. CANTER Processing Tool https://github.com/CANTERhm/Canter_Matlab_Library.

[185] Zemel, A., Rehfeldt, F., Brown, A. E. X., Discher, D. E., Safran, S. A. Optimal Matrix Rigidity for Stress-Fibre Polarization in Stem Cells. *Nature Physics* **2010**. https://doi.org/10.1038/nphys1613.

[186] Inoue, S., Frank, V., Hörning, M., Kaufmann, S., Yoshikawa, H. Y., Madsen, J. P., Lewis, A. L., Armes, S. P., Tanaka, M. Live Cell Tracking of Symmetry Break in Actin Cytoskeleton Triggered by Abrupt Changes in Micromechanical Environments. *Biomaterials Science* **2015**. https://doi.org/10.1039/c5bm00205b.

[187] Otsu, N. A Threshold Selection Method from Gray-Level Histograms. *IEEE Transactions on Systems, Man, and Cybernetics* **1979**. https://doi.org/10.1109/TSMC.1979.4310076.

[188] Cignoni, P., Callieri, M., Corsini, M., Dellepiane, M., Ganovelli, F., Ranzuglia, G. MeshLab: An Open-Source Mesh Processing Tool. In *Sixth Eurographics Italian Chapter Conference*; 2008; p 129.136.

[189] Bückmann, T., Stenger, N., Kadic, M., Kaschke, J., Frölich, A., Kennerknecht, T., Eberl, C., Thiel, M., Wegener, M. Tailored 3D Mechanical Metamaterials Made by Dip-in Direct-Laser-Writing Optical Lithography. *Advanced Materials* **2012**. https://doi.org/10.1002/adma.201200584.

[190] Sodian, R., Loebe, M., Hein, A., Martin, D. P., Hoerstrup, S. P., Potapov, E. V., Hausmann, H., Lueth, T., Hetzer, R. Application of Stereolithography for Scaffold Fabrication for Tissue Engineered Heart Valves. *ASAIO Journal* **2002**. https://doi.org/10.1097/00002480-200201000-00004.

[191] Leiss, M., Beckmann, K., Girós, A., Costell, M., Fässler, R. The Role of Integrin Binding Sites in Fibronectin Matrix Assembly in Vivo. *Current Opinion in Cell Biology* **2008**. https://doi.org/10.1016/j.ceb.2008.06.001.

[192] Brigo, L., Urciuolo, A., Giulitti, S., Della Giustina, G., Tromayer, M., Liska, R., Elvassore, N., Brusatin, G. 3D High-Resolution Two-Photon Crosslinked Hydrogel Structures for Biological Studies. *Acta Biomaterialia* **2017**. https://doi.org/10.1016/J.ACTBIO.2017.03.036.

[193] Yue, K., Trujillo-de Santiago, G., Alvarez, M. M., Tamayol, A., Annabi, N., Khademhosseini, A. Synthesis, Properties, and Biomedical Applications of Gelatin

Methacryloyl (GelMA) Hydrogels. *Biomaterials* **2015**. https://doi.org/10.1016/j.biomaterials.2015.08.045.

[194] Zhu, M., Wang, Y., Ferracci, G., Zheng, J., Cho, N. J., Lee, B. H. Gelatin Methacryloyl and Its Hydrogels with an Exceptional Degree of Controllability and Batch-to-Batch Consistency. *Scientific Reports* **2019**. https://doi.org/10.1038/s41598-019-42186-x.

[195] Claaßen, C., Claaßen, M. H., Truffault, V., Sewald, L., Tovar, G. E. M., Borchers, K., Southan, A. Quantification of Substitution of Gelatin Methacryloyl: Best Practice and Current Pitfalls. *Biomacromolecules* **2018**. https://doi.org/10.1021/acs.biomac.7b01221.

[196] Sewald, L., Claaßen, C., Götz, T., Claaßen, M. H., Truffault, V., Tovar, G. E. M., Southan, A., Borchers, K. Beyond the Modification Degree: Impact of Raw Material on Physicochemical Properties of Gelatin Type A and Type B Methacryloyls. *Macromolecular Bioscience* **2018**. https://doi.org/10.1002/mabi.201800168.

[197] Hoch, E., Hirth, T., Tovar, G. E. M., Borchers, K. Chemical Tailoring of Gelatin to Adjust Its Chemical and Physical Properties for Functional Bioprinting. *Journal of Materials Chemistry B* **2013**. https://doi.org/10.1039/c3tb20745e.

[198] Alberton, P., Dugonitsch, H. C., Hartmann, B., Li, P., Farkas, Z., Saller, M. M., Clausen-Schaumann, H., Aszodi, A. Aggrecan Hypomorphism Compromises Articular Cartilage Biomechanical Properties and Is Associated with Increased Incidence of Spontaneous Osteoarthritis. *International Journal of Molecular Sciences* **2019**. https://doi.org/10.3390/ijms20051008.

[199] Li, P., Fleischhauer, L., Nicolae, C., Prein, C., Farkas, Z., Saller, M. M., Prall, W. C., Wagener, R., Heilig, J., Niehoff, A., Clausen-Schaumann, H., Alberton, P., Aszodi, A. Mice Lacking the Matrilin Family of Extracellular Matrix Proteins Develop Mild Skeletal Abnormalities and Are Susceptible to Age-Associated Osteoarthritis. *International Journal of Molecular Sciences* **2020**. https://doi.org/10.3390/ijms21020666.

[200] O'Connell, C. D., Zhang, B., Onofrillo, C., Duchi, S., Blanchard, R., Quigley, A., Bourke, J., Gambhir, S., Kapsa, R., Di Bella, C., Choong, P., Wallace, G. G. Tailoring the Mechanical Properties of Gelatin Methacryloyl Hydrogels through Manipulation of the Photocrosslinking Conditions. *Soft Matter* **2018**. https://doi.org/10.1039/c7sm02187a.

[201] Xin, S., Chimene, D., Garza, J. E., Gaharwar, A. K., Alge, D. L. Clickable PEG Hydrogel Microspheres as Building Blocks for 3D Bioprinting. *Biomaterials Science* **2019**. https://doi.org/10.1039/c8bm01286e.

[202] Pennacchio, F. A., Casale, C., Urciuolo, F., Imparato, G., Vecchione, R., Netti, P. A. Controlling the Orientation of a Cell-Synthesized Extracellular Matrix by Using Engineered Gelatin-Based Building Blocks. *Biomaterials Science* **2018**. https://doi.org/10.1039/c7bm01093a.

[203] Roether, J., Bertels, S., Oelschlaeger, C., Bastmeyer, M., Willenbacher, N. Microstructure, Local Viscoelasticity and Cell Culture Suitability of 3D Hybrid HA/Collagen Scaffolds. *PLoS ONE* **2018**. https://doi.org/10.1371/journal.pone.0207397.

[204] Lee, K.-S., Yang, D.-Y., Park, S. H., Lim, T. W., Kim, R. H. Improvement of Spatial Resolution in Two-Photon Stereolithography Kwang-Sup. *2006 International Symposium on Biophotonics, Nanophotonics and Metamaterials, Hangzhou* **2006**. https://doi.org/10.1109/METAMAT.2006.334983.

[205] Stampfl, J., Liska, R., Ovsianikov, A. *Multiphoton Lithography: Techniques, Materials, and Applications*; Wiley-VCH Verlag, 2017.

[206] Chen, H., Zhong, J., Wang, J., Huang, R., Qiao, X., Wang, H., Tan, Z. Enhanced Growth and Differentiation of Myoblast Cells Grown on E-Jet 3D Printed Platforms. *International Journal of Nanomedicine* **2019**. https://doi.org/10.2147/IJN.S193624.

[207] Linke, P., Suzuki, R., Yamamoto, A., Nakahata, M., Kengaku, M., Fujiwara, T., Ohzono, T., Tanaka, M. Dynamic Contact Guidance of Myoblasts by Feature Size and Reversible Switching of Substrate Topography: Orchestration of Cell Shape, Orientation, and Nematic Ordering of Actin Cytoskeletons. *Langmuir* **2019**. https://doi.org/10.1021/acs.langmuir.8b02972.

[208] Hörning, M., Kidoaki, S., Kawano, T., Yoshikawa, K. Rigidity Matching between Cells and the Extracellular Matrix Leads to the Stabilization of Cardiac Conduction. *Biophysical Journal* **2012**. https://doi.org/10.1016/j.bpj.2011.12.018.

[209] Romanazzo, S., Forte, G., Ebara, M., Uto, K., Pagliari, S., Aoyagi, T., Traversa, E., Taniguchi, A. Substrate Stiffness Affects Skeletal Myoblast Differentiation in Vitro. *Science and Technology of Advanced Materials* **2012**. https://doi.org/10.1088/1468-6996/13/6/064211.

[210] Li, J., Zhang, L., Yu, L., Minami, I., Miyagawa, S., Hörning, M., Dong, J., Qiao, J., Qu, X., Hua, Y., Fujimoto, N., Shiba, Y., Zhao, Y., Tang, F., Chen, Y., Sawa, Y., Tang, C., Liu, L. Circulating Re-Entrant Waves Promote Maturation of HiPSC-Derived Cardiomyocytes in Self-Organized Tissue Ring. *Communications Biology* **2020**. https://doi.org/10.1038/s42003-020-0853-0.

[211] Yaffe, D., Ora, S. Serial Passaging of Myogenic Cells Isolated from Dystrophic Mouse Muscle. *Nature* **1977**.

[212] Murphy, S. M., Kiely, M., Jakeman, P. M., Kiely, P. A., Carson, B. P. Optimization of an in Vitro Bioassay to Monitor Growth and Formation of Myotubes in Real Time. *Bioscience Reports* **2016**. https://doi.org/10.1042/BSR20160036.

[213] Knoška, J., Adriano, L., Awel, S., Beyerlein, K. R., Yefanov, O., Oberthuer, D., Peña Murillo, G. E., Roth, N., Sarrou, I., Villanueva-Perez, P., Wiedorn, M. O., Wilde, F., Bajt, S., Chapman, H. N., Heymann, M. Ultracompact 3D Microfluidics for Time-Resolved Structural Biology. *Nature Communications* **2020**. https://doi.org/10.1038/s41467-020-14434-6.

[214] Bohne, S., Heymann, M., Chapman, H. N., Trieu, H. K., Bajt, S. 3D Printed Nozzles on a Silicon Fluidic Chip. *Review of Scientific Instruments* **2019**. https://doi.org/10.1063/1.5080428.

[215] Cassot, F., Lauwers, F., Fouard, C., Prohaska, S., Lauwers-Cances, V. A Novel Three-Dimensional Computer-Assisted Method for a Quantitative Study of Microvascular Networks of the Human Cerebral Cortex. *Microcirculation* **2006**. https://doi.org/10.1080/10739680500383407.

[216] Armstrong, J. K., Wenby, R. B., Meiselman, H. J., Fisher, T. C. The Hydrodynamic Radii of Macromolecules and Their Effect on Red Blood Cell Aggregation. *Biophysical Journal* **2004**. https://doi.org/10.1529/biophysj.104.047746.

[217] Böcker, W., Yin, Z., Drosse, I., Haasters, F., Rossmann, O., Wierer, M., Popov, C., Locher, M., Mutschler, W., Docheva, D., Schieker, M. Introducing a Single-Cell-Derived Human Mesenchymal Stem Cell Line Expressing HTERT after Lentiviral Gene Transfer. *Journal of Cellular and Molecular Medicine* **2008**. https://doi.org/10.1111/j.1582-4934.2008.00299.x.

[218] Flamourakis, G., Kordas, A., Barmparis, G. D., Ranella, A., Farsari, M. Low-Autofluorescence, Transparent Composite for Multiphoton 3D Printing. *Optical Materials Express* **2020**. https://doi.org/10.1364/ome.418269.

[219] Van Hoorick, J., Gruber, P., Markovic, M., Tromayer, M., Van Erps, J., Thienpont, H., Liska, R., Ovsianikov, A., Dubruel, P., Van Vlierberghe, S. Cross-Linkable Gelatins with Superior Mechanical Properties Through Carboxylic Acid Modification: Increasing the Two-Photon Polymerization Potential. *Biomacromolecules* **2017**. https://doi.org/10.1021/acs.biomac.7b00905.

[220] Knudsen, L., Ochs, M. The Micromechanics of Lung Alveoli: Structure and Function of Surfactant and Tissue Components. *Histochemistry and Cell Biology* **2018**. https://doi.org/10.1007/s00418-018-1747-9.

[221] Baldassi, D., Gabold, B., Merkel, O. M. Air À Liquid Interface Cultures of the Healthy and Diseased Human Respiratory Tract : Promises, Challenges, and Future Directions. **2021**. https://doi.org/10.1002/anbr.202000111.

[222] Chang, S., Kwon, N., Kim, J., Kohmura, Y., Ishikawa, T., Rhee, C. K., Je, J. H., Tsuda, A. Synchrotron X-Ray Imaging of Pulmonary Alveoli in Respiration in Live Intact Mice. *Scientific Reports* **2015**. https://doi.org/10.1038/srep08760.

[223] Blakey-Milner, B., Gradl, P., Snedden, G., Brooks, M., Pitot, J., Lopez, E., Leary, M., Berto, F., du Plessis, A. Metal Additive Manufacturing in Aerospace: A Review. *Materials and Design*. 2021. https://doi.org/10.1016/j.matdes.2021.110008.

[224] Wu, D., Niu, L.-G. G., Wu, S.-Z. Z., Xu, J., Midorikawa, K., Sugioka, K. Ship-in-a-Bottle Femtosecond Laser Integration of Optofluidic Microlens Arrays with Center-Pass Units Enabling Coupling-Free Parallel Cell Counting with a 100% Success Rate. *Lab on a Chip* **2015**. https://doi.org/10.1039/C4LC01439A.

[225] Liu, W., Zhang, Y. S., Heinrich, M. A., De Ferrari, F., Jang, H. L., Bakht, S. M., Alvarez, M. M., Yang, J., Li, Y. C., Trujillo-de Santiago, G., Miri, A. K., Zhu, K., Khoshakhlagh, P., Prakash, G., Cheng, H., Guan, X., Zhong, Z., Ju, J., Zhu, G. H., Jin, X., Shin, S. R., Dokmeci, M. R., Khademhosseini, A. Rapid Continuous Multimaterial Extrusion Bioprinting. *Advanced Materials* **2017**. https://doi.org/10.1002/adma.201604630.

[226] Mandal, K., Wang, I., Vitiello, E., Orellana, L. A. C., Balland, M. Cell Dipole Behaviour Revealed by ECM Sub-Cellular Geometry. *Nature Communications* **2014**. https://doi.org/10.1038/ncomms6749.

[227] Guilak, F., Cohen, D. M., Estes, B. T., Gimble, J. M., Liedtke, W., Chen, C. S. Control of Stem Cell Fate by Physical Interactions with the Extracellular Matrix. *Cell Stem Cell* **2009**. https://doi.org/10.1016/j.stem.2009.06.016.

[228] D'Arcangelo, E., McGuigan, A. P. Micropatterning Strategies to Engineer Controlled Cell and Tissue Architecture in Vitro. *BioTechniques* **2015**. https://doi.org/10.2144/000114245.

[229] Kilian, K. A., Bugarija, B., Lahn, B. T., Mrksich, M. Geometric Cues for Directing the Differentiation of Mesenchymal Stem Cells. *Proceedings of the National Academy of Sciences of the United States of America* **2010**. https://doi.org/10.1073/pnas.0903269107.

[230] Dalby, M. J., Gadegaard, N., Tare, R., Andar, A., Riehle, M. O., Herzyk, P., Wilkinson, C. D. W., Oreffo, R. O. C. The Control of Human Mesenchymal Cell Differentiation Using Nanoscale Symmetry and Disorder. *Nature Materials* **2007**. https://doi.org/10.1038/nmat2013.

[231] Regehly, M., Garmshausen, Y., Reuter, M., König, N. F., Israel, E., Kelly, D. P., Chou, C. Y., Koch, K., Asfari, B., Hecht, S. Xolography for Linear Volumetric 3D Printing. *Nature* **2020**. https://doi.org/10.1038/s41586-020-3029-7.

[232] Hahn, V., Kiefer, P., Frenzel, T., Qu, J., Blasco, E., Barner-Kowollik, C., Wegener, M. Rapid Assembly of Small Materials Building Blocks (Voxels) into Large Functional 3D Metamaterials. *Advanced Functional Materials* **2020**. https://doi.org/10.1002/adfm.201907795.

[233] Tromayer, M., Dobos, A., Gruber, P., Ajami, A., Dedic, R., Ovsianikov, A., Liska, R. A Biocompatible Diazosulfonate Initiator for Direct Encapsulation of Human Stem Cells: Via Two-Photon Polymerization. *Polymer Chemistry* **2018**. https://doi.org/10.1039/c8py00278a.

[234] Geng, Q., Wang, D., Chen, P., Chen, S. C. Ultrafast Multi-Focus 3-D Nano-Fabrication Based on Two-Photon Polymerization. *Nature Communications* **2019**. https://doi.org/10.1038/s41467-019-10249-2.

[235] Käpylä, E. *Direct Laser Writing of Polymer-Ceramic and Hydrogel Microstructures by Two-Photon Polymerization*; 2014.

[236] Ihnatouski, M., Pauk, J., Karev, D., Karev, B. AFM-Based Method for Measurement of Normal and Osteoarthritic Human Articular Cartilage Surface Roughness. *Materials* **2020**. https://doi.org/10.3390/ma13102302.

[237] Cicha, K., Koch, T., Torgersen, J., Li, Z., Liska, R., Stampfl, J. Young ' s Modulus Measurement of Two- Photon Polymerized Micro-Cantilevers by Using Nanoindentation Equipment. *Journal of Applied Physics* **2012**.

[238] Lemma, E. D., Rizzi, F., Sileo, L., Spagnolo, B., Dattoma, T., Qualtieri, A., Vittorio, M. De, Pisanello, F. Static and Dynamic Mechanical Characterization of Two-Photon Lithography Photoresists. **2015**.

[239] Lemma, E. D., Rizzi, F., Dattoma, T., Spagnolo, B., Sileo, L., Qualtieri, A., De Vittorio, M., Pisanello, F. Mechanical Properties Tunability of Three-Dimensional Polymeric Structures in Two-Photon Lithography. *IEEE Transactions on Nanotechnology* **2017**. https://doi.org/10.1109/TNANO.2016.2625820.

[240] Dex, S., Alberton, P., Willkomm, L., Söllradl, T., Bago, S., Milz, S., Shakibaei, M., Ignatius, A., Bloch, W., Clausen-Schaumann, H., Shukunami, C., Schieker, M., Docheva, D. Tenomodulin Is Required for Tendon Endurance Running and Collagen

I Fibril Adaptation to Mechanical Load. *EBioMedicine* **2017**. https://doi.org/10.1016/j.ebiom.2017.05.003.

[241] Muschter, D., Fleischhauer, L., Taheri, S., Schilling, A. F., Clausen-Schaumann, H., Grässel, S. Sensory Neuropeptides Are Required for Bone and Cartilage Homeostasis in a Murine Destabilization-Induced Osteoarthritis Model. *Bone* **2020**. https://doi.org/10.1016/j.bone.2019.115181.

[242] Reuten, R., Patel, T. R., McDougall, M., Rama, N., Nikodemus, D., Gibert, B., Delcros, J. G., Prein, C., Meier, M., Metzger, S., Zhou, Z., Kaltenberg, J., McKee, K. K., Bald, T., Tüting, T., Zigrino, P., Djonov, V., Bloch, W., Clausen-Schaumann, H., Poschl, E., Yurchenco, P. D., Ehrbar, M., Mehlen, P., Stetefeld, J., Koch, M. Structural Decoding of Netrin-4 Reveals a Regulatory Function towards Mature Basement Membranes. *Nature Communications* **2016**. https://doi.org/10.1038/ncomms13515.

[243] Lunzer, M., Shi, L., Andriotis, O. G., Gruber, P., Markovic, M., Thurner, P. J., Ossipov, D., Liska, R., Ovsianikov, A. A Modular Approach to Sensitized Two-Photon Patterning of Photodegradable Hydrogels. *Angewandte Chemie* **2018**. https://doi.org/10.1002/ange.201808908.

[244] Mahmodi, H., Piloni, A., Utama, R. H., Kabakova, I. Mechanical Mapping of Bioprinted Hydrogel Models by Brillouin Microscopy. *Bioprinting* **2021**. https://doi.org/10.1016/j.bprint.2021.e00151.

[245] Stampfl, J., Liska, R., Ovsianikov, A. *Multiphoton Lithography*; WILEY-VCH Verlag, 2017.

[246] Yu, F., Choudhury, D. Microfluidic Bioprinting for Organ-on-a-Chip Models. *Drug Discovery Today* **2019**. https://doi.org/10.1016/j.drudis.2019.03.025.

[247] Au, A. K., Huynh, W., Horowitz, L. F., Folch, A. 3D-Printed Microfluidics. *Angewandte Chemie - International Edition* **2016**. https://doi.org/10.1002/anie.201504382.

[248] Gissibl, T., Thiele, S., Herkommer, A., Giessen, H. Sub-Micrometre Accurate Free-Form Optics by Three-Dimensional Printing on Single-Mode Fibres. *Nature Communications*. 2016. https://doi.org/10.1038/ncomms11763.

[249] Olsen, M. H., Hjortø, G. M., Hansen, M., Met, Ö., Svane, I. M., Larsen, N. B. In-Chip Fabrication of Free-Form 3D Constructs for Directed Cell Migration Analysis. *Lab on a Chip* **2013**. https://doi.org/10.1039/c3lc50930c.

[250] Iosin, M., Scheul, T., Nizak, C., Stephan, O., Astilean, S., Baldeck, P. Laser Microstructuration of Three-Dimensional Enzyme Reactors in Microfluidic Channels. *Microfluidics and Nanofluidics* **2011**. https://doi.org/10.1007/s10404-010-0698-9.

[251] Amato, L., Gu, Y., Bellini, N., Eaton, S. M., Cerullo, G., Osellame, R. Integrated Three-Dimensional Filter Separates Nanoscale from Microscale Elements in a Microfluidic Chip. *Lab on a Chip* **2012**. https://doi.org/10.1039/c2lc21116e.

[252] Wang, J., He, Y., Xia, H., Niu, L. G., Zhang, R., Chen, Q. D., Zhang, Y. L., Li, Y. F., Zeng, S. J., Qin, J. H., Lin, B. C., Sun, H. B. Embellishment of Microfluidic Devices via Femtosecond Laser Micronanofabrication for Chip Functionalization.

Lab on a Chip **2010**. https://doi.org/10.1039/c003264f.

[253] Fay, C. D. Computer-Aided Design and Manufacturing (CAD/CAM) for Bioprinting. In: Crook J. (Eds). In *3D Bioprinting. Methods in Molecular Biology*; Humana: New York, NY, 2020; Vol. 2140, pp 27–41. https://doi.org/10.1007/978-1-0716-0520-2_3.

[254] Xu, C., Christensen, K., Zhang, Z., Huang, Y., Fu, J., Markwald, R. R. Predictive Compensation-Enabled Horizontal Inkjet Printing of Alginate Tubular Constructs. *Manufacturing Letters* **2013**. https://doi.org/10.1016/j.mfglet.2013.09.003.

List of Contributed Articles

Publications in the context of my doctoral studies:

All results of my doctoral thesis have been published in the following journals. These publications are listed below in chronological order.

(1) ***Amelie Erben***, *Marcel Hörning, Bastian Hartmann, Tanja Becke, Stephan A. Eisler, Alexander Southan, Séverine Cranz, Oliver Hayden, Nikolaus Kneidinger, Melanie Königshoff, Michael Lindner, Günter E. M. Tovar, Gerald Burgstaller, Hauke Clausen-Schaumann, Stefanie Sudhop, and Michael Heymann (2020),* ***Precision 3D-Printed Cell Scaffolds Mimicking Native Tissue Composition and Mechanics****, Adv. Healthcare Mater., DOI: 10.1002/adhm.202000918*

(2) Jun Zhang, Patrick Byers, ***Amelie Erben****, Christine Frank, Levin Schulte-Spechtel, Michael Heymann, Denitsa Docheva, Heinz P. Huber, Stefanie Sudhop, Hauke Clausen-Schaumann (2021),* ***Single Cell Bioprinting with Ultrashort Laser Pulses,*** *Adv. Funct. Mater., DOI: 10.1002/adfm.202100066*

(3) ***Amelie Erben****, Thomas Kellerer, Josefine Lissner, Constanze Eulenkamp, Thomas Hellerer, Hauke-Clausen-Schaumann, Stefanie Sudhop and Michael Heymann (2022),* ***Engineering Principles and Algorithmic Design Synthesis for Ultracompact Bio- Hybrid Perfusion Chip,*** *bioRxiv preprint, DOI: 10.1101/2022.03.16.484492*

Further publications

I was also involved in further projects and collaborations during the course of my time as PhD student, resulting in following publication, which is in the publication process.

Francisco Zurita, Leroy Grob*, **Amelie Erben***, Fulvia Del Duca, Hauke Clausen-Schaumann, Stefanie Sudhop, Oliver Hayden, Bernhard Wolfrum, Fully 3D-printed cuff electrode for small nerve interfacing, **Fully 3D-printed cuff electrodes for small nerve interfacing**, submitted to Advanced Materials Technologies in 2022*

** these authors contributed equally to this paper*

Journal Covers

Our design was selected as front inside cover of Advanced Healthcare Materials and was used as an inside cover for this document.

***Amelie Erben**, Marcel Hörning, Bastian Hartmann, Tanja Becke, Stephan A. Eisler, Alexander Southan, Séverine Cranz, Oliver Hayden, Nikolaus Kneidinger, Melanie Königshoff, Michael Lindner, Günter E. M. Tovar, Gerald Burgstaller, Hauke Clausen-Schaumann, Stefanie Sudhop, and Michael Heymann (2020), **High Precision 3D Bio-printing: Precision 3D-Printed Cell Scaffolds Mimicking Native Tissue Composition and Mechanics**. Adv. Healthcare Mater., DOI: 10.1002/adhm.202070087*